A Study of Overall Characteristics of the Liquid Scintillator in the 1.5m^3 Test Bench Facility for the KamLAND Experiment

by Hideki Watanabe

A dissertation submitted for the degree of

Master of Science

Reserch Center for Neutrino Science,
Department of Physics,
Tohoku University

February, 2000

Abstract

Neutrino has played an important role in the understanding of particle physics since it was postulated in 1933, and seems to complete the Standard Model as a massless particle with zero electric charge. However, some discrepancies between the observations and the theory are reported these days. They are well explained if the existence of a non-zero neutrino mass is introduced so that some projects are launched to solve this problem today.

The KamLAND experiment is one of the largest projects challenging to find the possibility of neutrino oscillations with the largest liquid scintillator detector in the world, which provides the ultra-low energy neutrino detection. The chief goal is to study the neutrino oscillations produced by the commercial nuclear reactors in Japan. The experiment's sensitivity covers one of the possible solutions of the solar neutrino problem.

Each detector for KamLAND has been studied separately. However, it is also essential to establish the experimental techniques required for the KamLAND experiment as well as to evaluate the performance of the integrated detector system in advance. These demands lead us to construct the Test Bench Facility which is modeled upon the KamLAND detector system, which may also help us to find unexpected defects of detectors.

This thesis mainly reports the characteristics of the liquid scintillator employed in the Test Bench Facility. The study of the response to gamma rays from ^{137}Cs, ^{60}Co and ^{207}Bi gives the linearity of the light output with respect to the energy deposit. This also indicates the energy resolution and the attenuation length of the liquid scintillator, to be $\sigma(\mathrm{E})/\mathrm{E} = 3.3 + 18.1\%/\sqrt{\mathrm{E(MeV)}}$ and 28.8cm, respectively. The 53-hour operation of the Test Purified System gives a good result of the 5% light output improvement in terms of the anthracene correspondence. The delayed coincidence technique and the n/γ discrimination are very crucial for the $\bar{\nu}_e$ detection in KamLAND. Both are verified under the Am/Be source employment, and the neutron capture time is thus obtained to be $173 \pm 2\mu$s, as well as the differentiation between neutrons and gammas. These results seem to satisfy the requirements for the KamLAND experiments.

Contents

List of Figures

List of Tables

Chapter 3

The Test Bench Facility

This chapter gives the general view of the Test Bench Facility with its significance and detector components.

3.1 Significance

The significance of the study in the Test Bench Facility is to have experiences of techniques required for the KamLAND experiment. In this respect, this facility is constructed with modeling on the KamLAND detector which is totally integrated system. It is also very important to find unexpected defects of the system beforehand, prior to the KamLAND experiment. This integrated system is explained in detail in the following section. The study itself can be classified into the following two items generally:

- Study of the characteristics of the liquid scintillator, mainly in terms of the light output and the pulse shape discrimination. Refer to Chapter 4, 5, and 7 for further discussion.
- Establishment of the delayed coincidence technique, which is necessary for the $\bar{\nu}_e$ detection in KamLAND. See Chapter 6 for detailed results obtained in this system.

3.2 Detector

The Test Bench Facility consists of the liquid scintillator surrounded by the prototype balloon and the purified water substituted for the buffer oil due to the restriction of the

this way, α from ^{224}Ra, ^{220}Rn, ^{216}Po and ^{212}Bi, and β+γ from ^{212}Pb and ^{208}Tl can be reduced. The ^{208}Tl decays are, particularly, the important background relevant to the recoil electron detection scattered by the solar ^{8}B neutrinos for T $\geq$ 3MeV. β and γ from ^{208}Tl stretched up to 5MeV. Its longer lifetime (4.5min) followed by the ^{212}Bi α decay would not restrict the correlated α-β rejection. In fact, correlated events can be removed in case the corresponding vertices are less than 2m apart after $\simeq$ 10 minutes.

Therefore, it is possible to subtract the number of background events due to the preceding decay in the U/Th chains accurately from the number of observed events. Here, it is assumed that α particles suffered the quenching with its factor of 0.1 found by the laboratory test, can be differentiated from electrons and photons by the pulse shape discrimination with 90% efficiency.

- Conclusion

For the reactor neutrino experiment, random coincidence of natural radioactivity and correlated signals from neutrons produced by muon spallation in the rock are prospective backgrounds. The first one will be reduced by realizing the liquid scintillator purity of 10^{-16} g/g in U, Th and K. The reduction of the second one needs the spallation cut explained before. The solar neutrino experiment, especially the measurement of the ^{7}Be line of solar neutrino, is challenging in terms of the reduction of the radioactivity of the cosmogenic ^{11}C and ^{7}Be, and the internal U/Th activity of the scintillator with its 10^{-16} g/g concentration. The detail knowledge for the detector resolution with KamLAND's high statistics will enable us to open the frontier of the ultra-low energy neutrino detection.

decay chains of the long lived ^{238}U, ^{232}Th and ^{40}K which are contained in small amounts in rocks out of the KamLAND detector and material used in the detector construction. The other is the decay of ^{222}Rn continuously produced in the decay of ^{238}U in rocks and detector materials. The radon diffuses quickly into many materials with its longer lifetime (a few days) so that it may disperse the radioactivity through the whole detector. Another is the decay of ^{60}Co artificially added to steel. In the following, the first two backgrounds are mainly discussed since ^{60}Co itself is not expected to be so much in the detector and has a trivial spectrum, which yields easy removal of it.

^{222}Rn will, actually, have a distribution, which will be largely independent from U. Even the large volume of the detector giving a big shielding factor for external radioactivity, radon may disperse inside KamLAND. The radon specific activity in the buffer volume is estimated to be 10 mBq/m^3. Assuming the balloon works as a barrier with a permeability coefficient for radon of 10 cm^3 mm m^{-2} day^{-1} atm, the specific radon activity in the active volume can be reduced to 1 μBq/m^3 by using the nylon films.

For the reactor experiment using 1kt detector volume, a 10^{-14} g/g U and Th concentration in the liquid scintillator would increase the random coincidence to 0.15 day^{-1} from 0.05 day^{-1} expected in a 10^{-16} g/g concentration. This concentration also limits the backgrounds from both neutrons produced by cosmic rays and correlated natural radioactivity, to 0.05 day^{-1} and 0.00 day^{-1}, respectively. Moreover, these internal contaminations of the liquid scintillator is required even for the solar neutrino experiment, as well as the fiducial volume reduction for extra shielding from the external radioactivity, and the cut for the further internal activity inside the fiducial volume.

Actually, both ^{214}Bi-^{214}Po in the U series and ^{212}Bi-^{212}Po in the Th series are removed event by event through the α-β coincidence with 95% tagging efficiency ($t_{1/2}$ = 164μs and 0.30μs, respectively). Well understanding of the correlated Bi-Po rates will thus help to reduce other decay which are in equilibrium with them. In the U/Rn chain, α from ^{222}Rn and ^{218}Po, and β +γ from ^{214}Pb may be subtracted. In

neutron. 10.5% of them are accompanied by a 0.478MeV photon[20]. This is also a problem for the solar neutrino detection. Again, we need to know the resolution of the detector in detail. The estimation of the production rate for both elements will be helpful for the reduction of such long-lived isotopes.

Actually, neutron spallation may also leave radioactive sources as in N + n $\rightarrow$ N′ + (n, p, α, π or γ) where N′ is a produced radioactive isotope. ^{11}C, ^{7}Be and ^{12}B are such isotopes produced mainly. ^{11}C can be vetoed as explained in the muon spallation. ^{12}B will be reduced due to its shorter half-life, and ^{7}Be is negligible compared to the total ^{7}Be amount of the detector.

Capturing by neutron and muon should not be so dangerous. Most neutrons are captured chiefly on protons and ^{12}C. These capture leave stable isotopes of ^{2}H and ^{13}C, respectively. ^{13}C is also captured and gives the radioactive isotope of ^{14}C. The number of produced ^{14}C is almost negligible compared to that of already existing in the detector. The muon capture reaction is μ + (A,Z) $\rightarrow$ (A,Z - 1)* + ν_μ. The excited nuclei (A,Z - 1)* de-excites into radioactive isotopes. ^{12}B is the only isotope produced in KamLAND. They can be vetoed due to their short half-life ($\simeq$ 20ms). Even without the veto, the rate would be 1 day^{-1} in 0.6kt fiducial volume. Possible muon capture reactions (including ^{12}B production) are listed in Table 2.6[20].

target	reaction(s)	isotope(s)	half-life	decay mode	energy(MeV)
^{12}C	(μ^-,2αn)	^{3}H	12.3year	β^-	0.0186
^{12}C	(μ^-,α)	^{8}Li	838msec	β^-	16.0
^{12}C	(μ^-,np)	^{10}Be	1.6$\times$10^{6}year	β^-	0.556
^{12}C	(μ^-,p)	^{11}Be	13.8sec	β^-	11.5
^{12}C	(μ^-)	^{12}B	20.2msec	β^-	13.4

Table 2.6: Possible reactions for muon capture

We finally understand the background initiated by muon are not so dangerous if the vetoes explained above are well-performed.

- Background from Natural Radioactivity

There are three possible backgrounds from natural radioactivity. The one is the

the detector, which gives a rate of 5,000 neutrons/day in the 1kt detector and 3,000 neutrons/day in the 0.6kt fiducial volume. To estimate backgrounds by the spallation and the capture is crucial for solar neutrino experiment.

The chief reactions from muon spallation are relevant to ^{12}C as the target. In Table 2.4 and Table 2.5[20] some reactions relevant for muon spallation are listed.

target	reaction(s)	isotope(s)	half-life	decay mode	energy(MeV)
^{12}C	(γ,n),(π^+,p)	^{11}C	21min	β^+	1.98
^{12}C	(γ,2n),(π^+,np)	^{10}C	19.3sec	β^+	3.6
^{12}C	(γ,p),(π^-,n)	^{11}B	stable		
^{12}C	(γ,np),(π^-,2n)	^{10}B	stable		
^{12}C	(γ,nα)	^{7}Be	53.3day	E.C.	0.862

Table 2.4: Part of main reactions with ^{12}C followed by muon spallation Here, γ is a virtual particle emitted by muon.

target	reaction(s)	isotope(s)	half-life	decay mode	energy(MeV)
^{13}C	(γ,n),(π^+,p)	^{12}C	stable		
^{13}C	(γ,2p),(π^-,np)	^{11}Be	13.8sec	β^-	11.5
^{16}O	(γ,n),(π^+,p)	^{15}O	122sec	β^+	2.76
^{16}O	(γ,π^+),(n,p)	^{16}N	7.1sec	β^-	10.4

Table 2.5: Part of main reactions with other targets followed by muon spallation Here, γ is a virtual particle emitted by muon.

^{10}C, ^{11}C and ^{7}Be are dangerous isotopes giving problematic decays. Assuming each neutron created in the detector is associated with their production, we may obtain a production rate of ^{10}C and ^{11}C of $< 1{,}800$ day^{-1} [12]. ^{10}C with shorter half-life can be reduced via the off-line cut using an extended veto for small regions of the detector. ^{11}C emits e^+ with a minimum visible energy of 1.02MeV, which itself is above the endpoint of the energy range for solar neutrinos. However, the restricted resolution of the detector and the high production rate of ^{11}C would worsen the detection of the solar neutrino. ^{7}Be gives rise to the electron capture and emits

and then to drop exponentially. The expected muon rates in the scintillator will be thus 0.21Hz, and 0.15Hz in the 0.6kt fiducial volume of the detector [12]. Muon traversed the veto detector will be removed with events vetoed by the 50ms window veto for the region around the muon. For muon traversed the central detector 250ms window veto will be applied also with the muon proximity. The dead times are 0.3% and 0.5%, respectively, with a conservative veto volume of 10% of the detector volume. It is therefore possible to remove all backgrounds from muon decay and short half-life induced radioactivity. Although, cosmic ray muons generate backgrounds through spallations which require another way to reduce. One possible background is an energetic neutron generated in the rock outside which is undetected at the veto detector and reaches the central detector subsequently generates background events. This results in radioactive nuclei with lifetimes of order of 100ms or greater, which turns into another possible background.

The energetic neutrons have been measured by several underground experiments and the neutron yield for each muon at 2,700 m.w.e. is calculated 4×10^{-4} $g^{-1}cm^2$. The minimum energy deposit for solar neutrinos is 280keV, which retains only 2 events/day in the 0.6kt fiducial region. These backgrounds for single events are negligible compared to the natural radioactivity background explained later. Double events are obtained whose energy threshold is 1MeV using the 1kt detector by introducing the cut of the signal correlation as well as the neutron capture within 1m of the vertex of the position. They are retained only < 0.05 events/day (2 events/day of signals from the reactor experiments). Hence the signals from muon induced neutrons will not restrict the experiment.

Nuclei in the liquid scintillator will be excited via muon capture, neutron capture, muon spallation or neutron spallation. Once the excitation undergoes, the nuclei will de-excite within the order of ns with the emission of proton, α, neutron, and γ accompanying with another possible radioactive nuclei whose lifetime extends from ms to years. Unless the short lifetime, it will be hard to remove them by the cosmic ray veto. The estimation of the number of productions of such radioactive nuclei processes will be based on the calculations of the neutron production inside

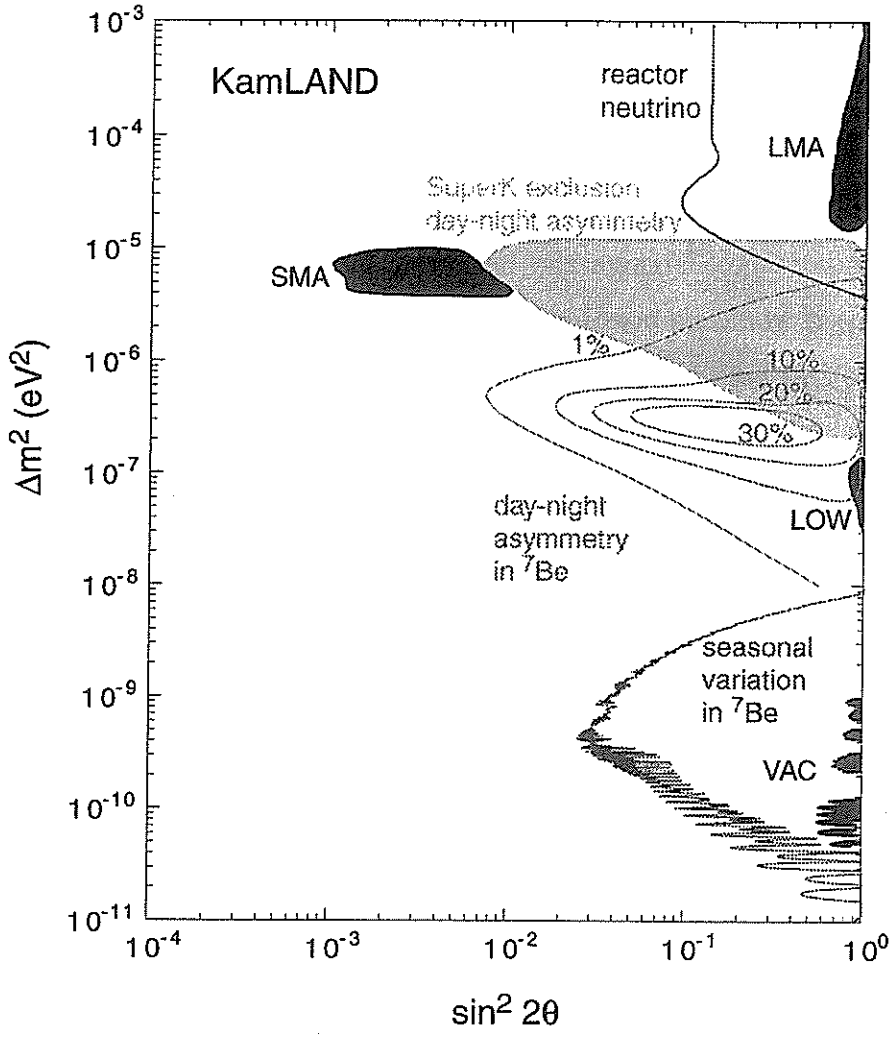

Fig. 2.9: Exclusion of the LOW solution with 95% CL limit on several up-down asymmetry

control them with careful calibration. The seasonal variation itself can be also useful way for finding neutrino oscillations.
If the correct explanation of the solar neutrino problem is the VAC solution, then there are a few tens of oscillations that occur between the Sun and the Earth.

Another possible study in ^{7}Be is the day-night asymmetry. The neutrinos observed at night may experience the MSW effect while the ones observed in the daytime may not because the former ones traverse the Earth. Figure 2.9 shows the exclusion of the LOW solution with 95% CL limit on several up-down asymmetry[19].

KamLAND can also observe the ^{8}B neutrinos with the extension towards the lower energy range. Though the background is expected to be dominated by the ^{208}Tl decay, it would be possible to measure the ^{8}B electron recoil spectrum down to about 3MeV in case the background is removed. In KamLAND's 600 tons fiducial volume one would expect about 4 events per day (assuming 100% efficiency) from the SSM, or 2 events/day as determined by Super-Kamiokande. Moreover, this is a new window in the ^{8}B neutrino spectrum extending the capabilities of Super-Kamiokande and SNO.

Combining with the result obtained in the reactor experiment, actually, we will be capable of discriminating among the four solutions to the solar neutrino problem.

2.4 Expected Backgrounds in KamLAND

Backgrounds for our interest in KamLAND are produced by cosmic muon induced processes and natural radioactivity. We are interested in mainly double events for anti-neutrino detection and single events, for example, from low energy neutrino scattering on electrons. More analysis about backgrounds are discussed below.

- Background from Cosmic Ray

  2,700 m.w.e. of rock surrounding the KamLAND detector helps to reduce cosmic radiation with total muon rate of 0.37Hz[2], measured by the full Kamiokande detector where KamLAND will be sited. The angular variation of muons is approximated by a $\cos^2\theta$ distribution. The energy distribution is expected to be flat from 0 to 100GeV

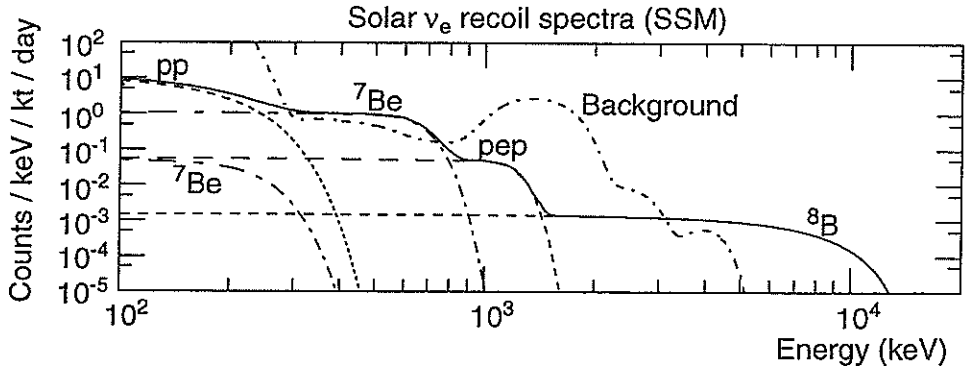

Fig. 2.8: Solar neutrino spectrum in SSM

neutrino source	SSM flux (10^8 cm^{-2}s^{-1})	T_{max} (MeV)	events (1/kt·day)
pp	591	0.25	2033
^{7}Be	51.5	0.66	841
pep	1.4	1.22	46
^{8}B	0.066	13.7	12

Table 2.3: Expected rates for the most important components of neutrino fluxes The event rate is for all recoil electrons, with T from 0 to T_{max}.

2.3 for more detail), our choice of the analysis interval 280-800keV for the ^{7}Be solar neutrinos is obvious. The energy threshold of 280keV is dictated by the ^{14}C background (end point of 157keV) while 800keV is taken above the kinematic limit of the electron recoil energy by ^{7}Be solar neutrino (665keV). Also, one can see the relevance of the ^{208}Tl (associated with the ^{232}Tl decay chain) for the detection of the ^{8}B neutrinos.

It is difficult to determine the full extent of the background in KamLAND, however, the solar ^{7}Be neutrino signal can be isolated from the background because it has a seasonal variation as a consequence of the eccentricity of the Earth's orbit. This uniquely identifies the source of the effect as solar. Even if we have backgrounds, which especially have a yearly modulation such as environmental radon, we could

R = 0.27 ± 0.04 taking the median of the theoretical value for the Homestake experiment. On the other hand, the Kamiokande experiment, using the elastic scattering of electrons with neutrinos shows R = 0.46 ± 0.05 ± 0.06 (statistical and systematic errors mentioned in order) for more than 7.5MeV of electron energy, still the solar neutrino problem exists. Because of the high energy threshold in Kamiokande, only ^{8}B are relevant to the reaction. In Homeskate, both ^{7}Be and ^{8}B are captured due to its lower energy threshold, however. Even taking its ^{8}B dependence to the neutrino spectrum into account, two calculated Rs are different. This suggests some existence of disturbing the neutrino energy spectrum.

KamLAND has an advantage to observe both ^{7}Be and ^{8}B separately described in detail as follows, so that some solutions may be found for the solar neutrino problem.

- Solar ν_e in KamLAND

KamLAND can study the solar neutrino problem directly via the detection of solar neutrinos, with the assumption of the required background level. It is essential to minimize radioactive contaminants in the construction of the detector itself, by keeping radon away from the active scintillator which is produced mainly in the photomultiplier glass and carried to the center of the detector by convection, and by designing electronics capable of providing extra discriminations.

Solar neutrinos interacting with the electrons in the scintillator will scatter and the resulting recoil electron can be detected via the scintillation light (more than 300 per day for the full Standard Solar Model[12]). The discrete ^{7}Be spectrum is thus obtained from a recoil electron spectrum characterized by a sharp edge at T_{max} = 665keV, where T is an electron recoil kinetic energy. Figure 2.8 shows the solar neutrinos' recoil spectra[12] expected in the SSM with prospective backgrounds.

The total expected rate is obtained by integrating over T and multiplying by the number of target electrons (3.4×10^{32} electrons per kt of scintillator). The result is shown in Table 2.3[12].

With the subtraction of both internal and cosmogenic background (see section

ν_es in this chain are

$$p + e^- + p \rightarrow {}^2H + \nu_e \quad (0.4\%), \tag{2.14}$$

$$^7Be + e^- \rightarrow {}^7Li + \nu_e \quad (15\%), \tag{2.15}$$

$$^8B \rightarrow {}^8Be + e^+ + \nu_e \quad (0.02\%), \tag{2.16}$$

and

$$^3He + p \rightarrow {}^4He + e^+ + \nu_e \quad (0.00002\%). \tag{2.17}$$

ν_e generated in (2.11) is called pp neutrino. With the same manner, pep neutrino in (2.14), ^{7}Be neutrino in (2.15), ^{7}Be neutrino in (2.16) and hep neutrino in (2.17).

In CNO cycle, three reactions given below generate ν_e.

$$^{13}N \rightarrow {}^{13}C + e^+ + \nu_e \tag{2.18}$$

$$^{15}O \rightarrow {}^{15}N + e^+ + \nu_e \tag{2.19}$$

$$^{17}F \rightarrow {}^{17}O + e^+ + \nu_e \tag{2.20}$$

- Solar neutrino problem[18]

The Homestake experiment was performed using ^{37}Cl as the target for neutrino capture. By counting ^{37}Ar generated with the following reaction,

$$\nu_e + {}^{37}Cl \rightarrow e^- + {}^{37}Ar, \tag{2.21}$$

thus observed rate is derived as 2.1 ± 0.3 SNU for the energy threshold of 0.81MeV. However, the expected rate in SSM is 7.9 ± 2.9 SNU (3σ uncertainty for both rates). Here, SNU stands for Solar Neutrino Unit, which is the product of a characteristic calculated solar neutrino flux ($cm^{-2}s^{-1}$) times a theoretical cross section for neutrino absorption (cm^2). This is thus the units of events per target atom per second and is chosen for convenience equal to 10^{-36} s^{-1}. This inconsistency between two rates is well-known the solar neutrino problem.

Let R be the ratio of the observation rate to the expected rate, which results in

Temperature(MeV)	ν_e ^{12}C$\rightarrow$^{12}N e$^-$	$\bar{\nu}_e$ ^{12}C$\rightarrow$^{12}B e$^+$	ν_x ^{12}C$\rightarrow$^{12}C*(15.11MeV) ν_x
3.5MeV(ν_e)	1.9	-	1.5
5.0MeV($\bar{\nu}_e$)	-	7.4	4.2
8.0MeV(ν_x)	-	-	51.9^i
	ν_e ^{12}C$\rightarrow$^{12}N e$^-$	$\bar{\nu}_e$ ^{12}C$\rightarrow$^{12}B e$^+$	ν_x ^{12}C$\rightarrow$^{12}C* (15.11MeV)ν_x
vacuum osc.	14.5	13.8	57.6^{ii}
MSW osc.	27	7.4	57.6^{ii}

Table 2.2: Expected rates detected for supernova neutrinos scattering on carbon Different cases are shown. Especially, in case *i*, all neutrino and anti-neutrino flavours are contributed, and in case *ii*, the number of the detected 15.11MeV photons are provided. All expected rates are represented about 5σ, enough to claim a discovery of the solution of the solar neutrino problem.

2.3.5 Solar neutrino

- ν_e production in the Sun[17]

  In main sequence stars like the Sun, the nuclear fusion takes place because of high physical density (150 g/cm^3) at the center and ν_es are generated with the following reaction.

$$\mathrm{p} + \mathrm{p} \rightarrow {}^2\mathrm{H} + \mathrm{e}^+ + \nu_e \quad (100\%) \tag{2.11}$$

  Generated ^{2}H, moreover, reacts with a proton subsequently generates ^{3}He.

$${}^2\mathrm{H} + \mathrm{p} \rightarrow {}^3\mathrm{He} + \gamma \quad (100\%) \tag{2.12}$$

  ^{3}He collides with another ^{3}He as follows.

$${}^3\mathrm{He} + {}^3\mathrm{He} \rightarrow {}^4\mathrm{He} + \mathrm{p} + \mathrm{p} \quad (85\%) \tag{2.13}$$

  After all, four protons fuse to give off two ν_es with energy of 26.73MeV per reaction in the Sun. Here, each percentage in parentheses shows the termination percentage which is the fraction of terminations of the proton-proton chain, $4\mathrm{p} \rightarrow \alpha + 2\mathrm{e}^+ + 2\nu_e$.

  The proton-proton chain (pp chain) is the principal nuclear reaction as well as the CNO cycle. Reactions above belong to this chain. Other possible reactions generate

and the vertex of $e^{\pm}$, ^{12}N and ^{12}B for the charged current reactions, and the sharp peak at 15.11MeV for the neutral current reaction. Actually, it is easy to discriminate among the inverse β-decay and two charged current reactions since each emits its own delayed signal with its characteristic energy and lifetime. All of such reactions are referred to the following. The first two of them are of the charged current reaction and the last one is of the neutral current reaction. And the expected energy spectrum is shown in Figure 2.7.

$$\nu_e + {}^{12}\mathrm{C} \rightarrow {}^{12}\mathrm{N} + \mathrm{e}^- \tag{2.8}$$

$$\bar{\nu}_e + {}^{12}\mathrm{C} \rightarrow {}^{12}\mathrm{B} + \mathrm{e}^+ \tag{2.9}$$

$$\nu_x + {}^{12}\mathrm{C} \rightarrow {}^{12}\mathrm{C}^*(15.11\mathrm{MeV}) + \nu_x \tag{2.10}$$

After all, neutrino flux of all six flavours, $\bar{\nu}_e$ and ν_e can be cleanly obtained separately. This

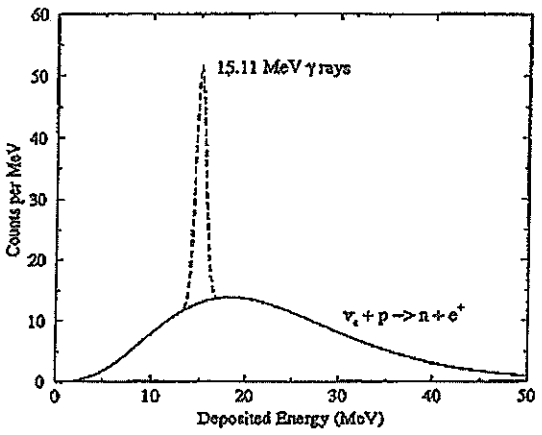

Fig. 2.7: Expected energy spectrum for supernova relevant reaction

allows us to study the time distribution and the temperature for each flavour of neutrino and thus the mechanism of the supernova explosion.

The expected number of events is shown in Table 2.2[12] with the assumptions about the temperatures of different neutrino flavours. The number of events expected without the effects of neutrino oscillations, with the vacuum oscillations (and maximum mixing) and with the matter-enhanced MSW oscillations are considered. The case of the vacuum oscillations is prepared for the just so oscillation scenario of the solar neutrino puzzle.

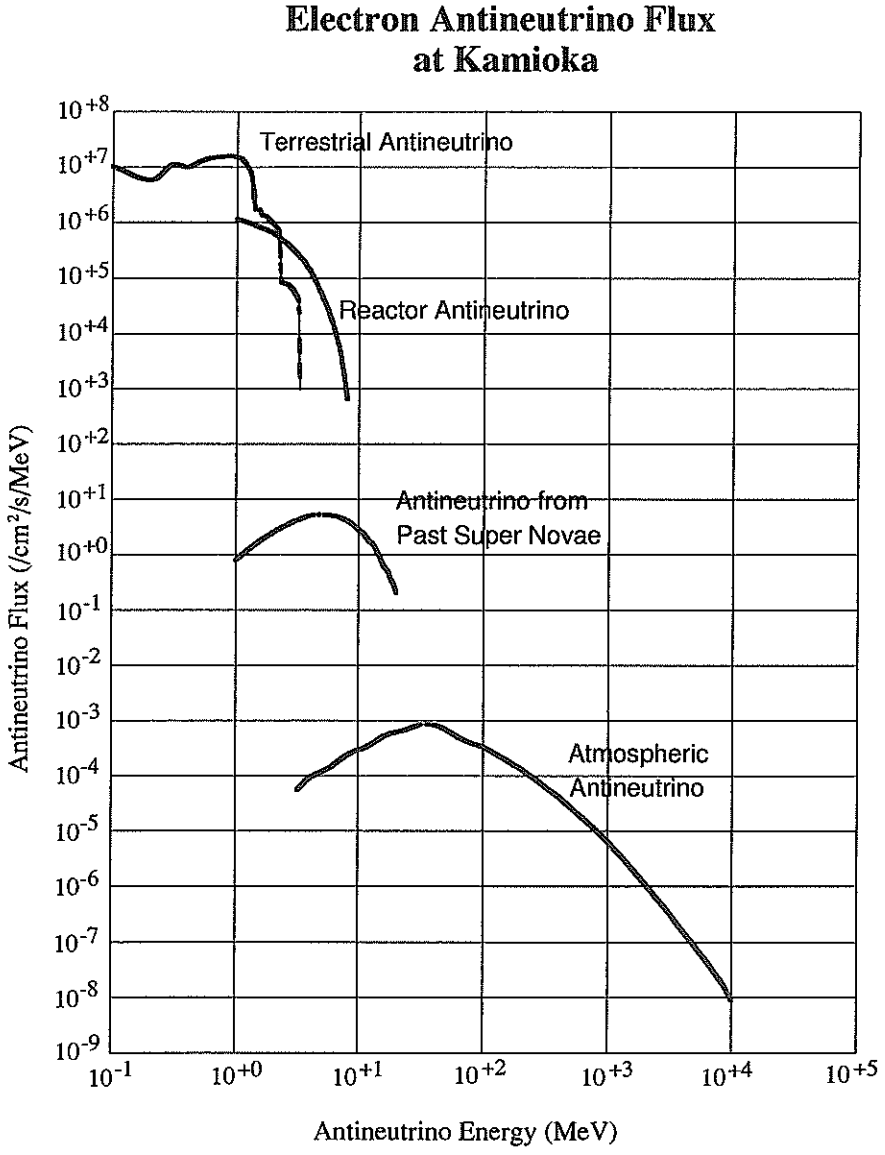

Fig. 2.6: $\bar{\nu}_e$ flux for relic neutrinos compared with other possible $\bar{\nu}_e$ in KamLAND

of gravitational collapses and a mean density of matter in the universe of 10^{-31} g/cm^3, thus we would expect to detect about $40\bar{\nu}_e$ /yr above 8MeV of energy in our detector[15]. The following is the theoretical flux for relic neutrinos, and the Figure 2.6 shows the $\bar{\nu}_e$ flux distribution of these neutrinos compared with other possible neutrinos in KamLAND.

$$\Phi_\nu(\mathrm{E}) = \int_{t_{min}}^{t_0} n_G(t_0) R_{SN}(t) \phi_\nu((1+z)E)(1+z)dt, \tag{2.6}$$

where $n_G(t) = n_G(t_0)(1+z)^3$ is the number density of galaxies, $R_{SN}(t)$ is the supernova rate per galaxy and z is the red shift.

As can be seen in the flux, between 10$\sim$50MeV relic neutrinos are dominated. In this region, the flux of atmospheric neutrinos as backgrounds for relic neutrinos are 10^{-3} lower so that relic neutrinos can be detected with few backgrounds. Understanding well this flux is required to find the mechanism of the large scale structure of the universe, because the flux depends on the rate of the supernova explosion per galaxy per year and that in each stage of the evolution of the universe as well as the mass distribution of the exploded stars.

2.3.4 Supernova neutrino

The KamLAND detector, containing a large number of carbon, leads to the detection of the scattering of ν and $\bar{\nu}$ from supernovae explosions on carbon nuclei. Assuming a supernova at the distance of 10kpc from the Earth with 3×10^{53}erg energy release equally divided among the six neutrino flavours[16] with 100% detection efficiency, we obtain the count rate of

$$\mathrm{N}_\nu = \frac{35.3 < \sigma >}{\mathrm{T(MeV)}} \text{counts} \tag{2.7}$$

in KamLAND where the thermally averaged cross section $< \sigma >$ is in terms of 10^{-42} cm^2 and the temperature T is in MeV.

The charged current reactions and the neutral current reactions are of our interest for the supernova detection in KamLAND. The electron scattering reaction ($\nu_x + \mathrm{e}^- \rightarrow \nu_x{}' + \mathrm{e}^{-\prime}$) and the inverse β-decay with delayed coincidence ($\bar{\nu}_e + \mathrm{p} \rightarrow \mathrm{e}^+ + \mathrm{n}$) are also used for supernova neutrino detection.

The signal for the charged current and neutral current reactions will be essentially background free due to the possibility of observing the correlation of the delayed coincidence

constitute background to the reactor neutrinos. However, they will be separated with their characteristic double peak structure. Figure 2.5 introduces the three different models, based on the different possible geophysical models of the heavy element concentration in the oceanic and continental crusts[14], compared with the spectrum for the reactor experiment with five year data taking at 3σ level.

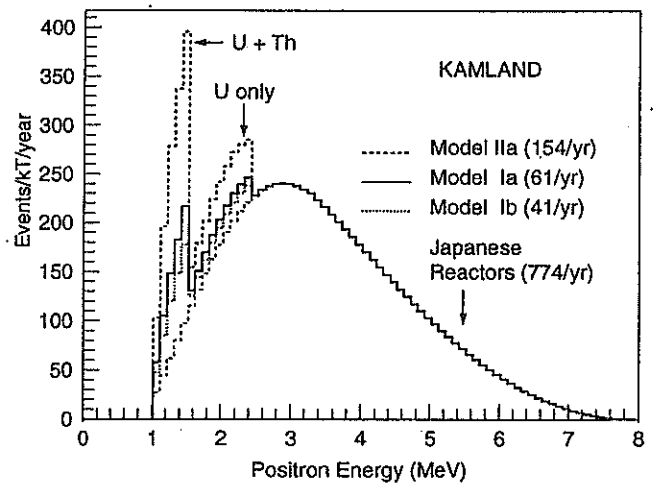

Fig. 2.5: Energy spectrum for geological anti-neutrinos with reactor signals Three different geophysical models are shown for the geological anti-neutrinos and no oscillations are assumed for all the spectra shown (Five year data taking at 3σ level).

2.3.3 Relic anti-neutrino

Neutrinos created in the first 10 seconds after the Big Bang could give us hints for the structure formation and evolution of the universe. These neutrinos fill the universe, which decoupled from the rest of the matter after the Big Bang, and thus are called relic neutrinos.

The number of such neutrinos is also directly relevant to the amount of the baryonic matter bound in black holes and neutron stars, and their average energy is expected to be around 15MeV. Due to the red shift, the energy spectrum carries information on the time distribution of large collapses during the history of our universe. Assuming a constant rate

Most of them are shut down for the preventive maintenance in the fall and spring when the demand for electricity is lower. During the past six years, the electrical power flux at Kamioka varies 30%. This variation can be used for the estimation of the background. Another possible backgrounds for reactor experiments are due to the geological anti-neutrinos (explained in detail in the next subsection). The event rates of them are expected small about 50 events/year (with a large uncertainty depending on models). The energy spectra of anti-neutrinos from ^{238}U and ^{232}Th chains are well known and do not deposit more than 2.49MeV including photons from annihilations as well so that the sensitivity of the reactor experiment will not be degraded by the geological anti-neutrinos.

Chief backgrounds are energetic neutrons from muon spallation in the surrounding rocks as the correlated background and internal natural radioactivity (^{238}U, ^{232}Th and ^{40}K etc.) in the detector as the random background. Imposing the condition mentioned above for the $\bar{\nu}_e$ from reactors, both backgrounds are reduced 0.05 events/day for each, compared to 2 signal events/day from reactor neutrinos[12]. Those backgrounds are described in detail in another section of this chapter.

2.3.2 Geological (Terrestrial) anti-neutrino

KamLAND will, for the first time, be able to detect anti-neutrinos from ^{238}U and ^{232}Th β-decay from the Earth. While the current experimental data are derived from sparse and shallow samplings, KamLAND will provide a global measurement. It is believed that 40% of the heat (16TW) emitted from the Earth's surface (40TW) comes from these β-decay, which produce anti-neutrinos. Therefore, their measurements will be of considerable dynamics of our planet. In addition, comparisons with similar measurements from Borexino[13] should make it possible to calculate the ratio of uranium to thorium in the crust and mantle of the Earth. This is because Borexino is surrounded by the thick continental crust, while KamLAND is located at the edge of the Asian plate. Hence, it receives anti-neutrinos from beneath the Pacific Ocean with more than half of its angular coverage.

The maximum energy in the prompt signal of the detected correlated event should be 2.49MeV with the photon annihilation since the maximum energy of geological anti-neutrinos is 3.27MeV. The expected energy spectrum is shown in Figure 2.5. They might

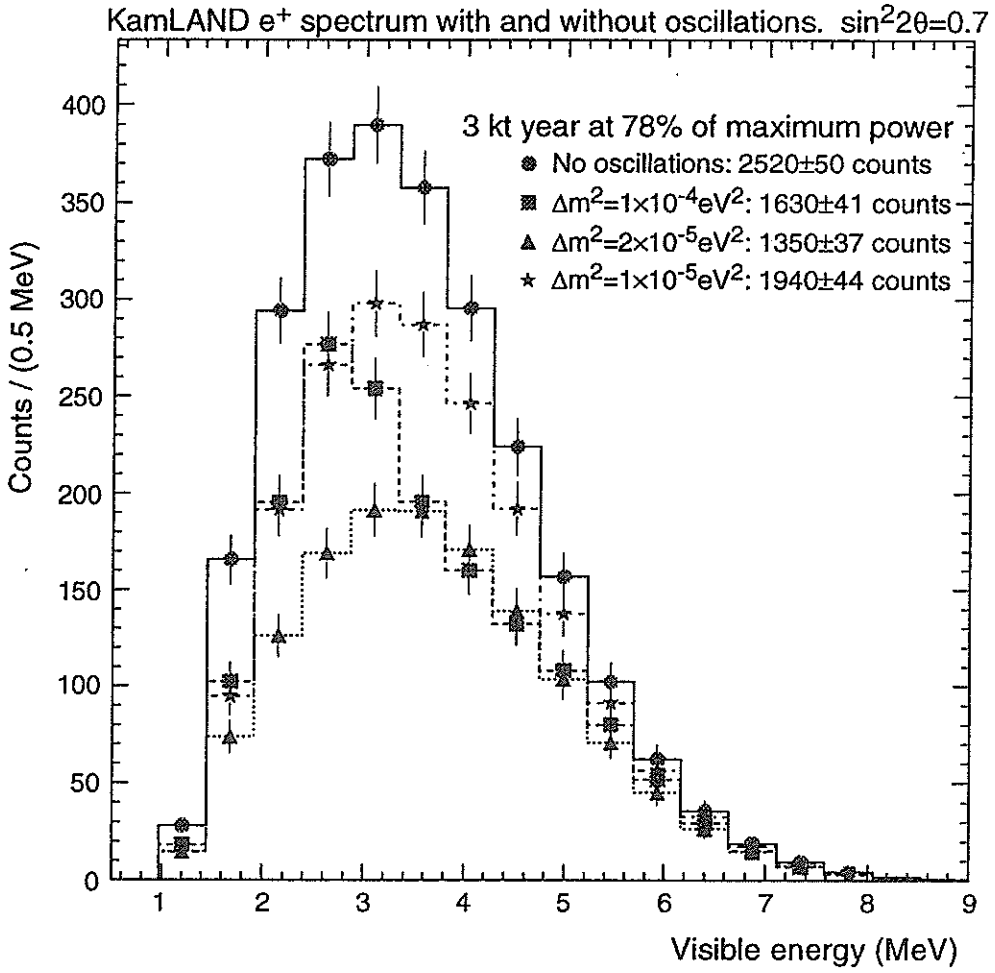

Fig. 2.4: The positron energy spectrum including photons from annihilations Three different oscillation cases and no oscillation case are considered. 100% detection efficiency and 3kt year at 78% of maximum power are assumed.

for prompt and the 1.8 $\sim$ 2.7MeV deposit for delayed signal (3σ cut for 2.2MeV neutron capture signal), as well as the delayed interval of 10 $\sim$ 500μs and the neutron captured within 1m of the vertex of the position. Further explanation of the delayed coincidence technique is given in Chapter 6.

We shall now see the determination of the emitted positron spectrum. To calculate the predicted counting rate in KamLAND for 100% efficiency from each reactor, the cross section of the reaction[11] should be calculated first which is given by (with all small corrections included)

$$\begin{aligned} \sigma(\mathrm{E}_{\bar{\nu}_e}) &= \frac{2\pi^2}{\mathrm{m}_{e^+}{}^5 f \tau_\mathrm{n}} \mathrm{p}_{e^+}\mathrm{E}_{e^+} \\ &= 9.5\times10^{-44}\mathrm{p}_{e^+}\mathrm{E}_{e^+}(\mathrm{MeV}^2\cdot\mathrm{cm}^2), \end{aligned} \tag{2.3}$$

where $\mathrm{E}_{e^+} = \mathrm{E}_{\bar{\nu}_e}$ - $\triangle$M with $\triangle\mathrm{M} = \mathrm{m_n} - \mathrm{m_p} = 1.293\mathrm{MeV}$, τ_n as the neutron lifetime, $f = 1.69$ as the integrated Fermi function for neutrino β-decay and p_{e^+} and E_{e^+} as the momentum and energy of the positron, respectively. Thus, the rate $\mathrm{N}_i(\mathrm{t},\mathrm{E}_{e^+},\triangle\mathrm{m}^2,\sin^2 2\theta)$ can be found with the number of target protons $\mathrm{N_p}$ and the initial spectrum $\mathrm{S}_i(\mathrm{t},\mathrm{d}_i,\mathrm{E}_{\bar{\nu}_e})$ to be

$$\mathrm{N}_i(\mathrm{t},\mathrm{E}_{e^+},\triangle\mathrm{m}^2,\sin^2 2\theta) = \mathrm{S}_i(\mathrm{t},\mathrm{d}_i,\mathrm{E}_{\bar{\nu}_e}) \times \mathrm{N_p} \times \frac{\sigma(\mathrm{E}_{\bar{\nu}_e})}{4\pi\mathrm{d}_i^2} \times [1-\sin^2 2\theta \sin^2(\frac{\triangle\mathrm{m}^2\mathrm{d}_i}{4\mathrm{E}_{\bar{\nu}_e}})]. \tag{2.4}$$

Here, d_i is the distance to KamLAND listed in Table 2.1, and the subscription i denotes the individual reactors. $\mathrm{S}_i(\mathrm{t},\mathrm{d}_i,\mathrm{E}_{\bar{\nu}_e})$ is, actually, obtained by multiplying the set of thermal powers $\mathrm{P}_{i,f}(\mathrm{t},\mathrm{d}_i)$ (f denotes the four fission isotopes) and the known $\bar{\nu}_e$ spectrum at d_i=0. After all, integrating over all positron energies with the contribution of all reactors and the background rate, we obtain the expected signal

$$\mathrm{N_{tot}}(\mathrm{t},\triangle\mathrm{m}^2,\sin^2 2\theta) = \int \mathrm{dE}_{e^+} \sum \mathrm{N}_i(\mathrm{t},\mathrm{E}_{e^+},\triangle\mathrm{m}^2,\sin^2 2\theta) + \mathrm{B.G.}. \tag{2.5}$$

The $\bar{\nu}_e$ energy spectrum is modified by oscillations. Therefore, additional information is available besides the absolute neutrino count. In Figure 2.4, the positron energy spectrum with three different sets of parameters as well as the no oscillation case are plotted.

It is usually to measure the background at zero or at least low reactor power for the best sensitivity of the absolute flux. This is possible even though there are many reactors.

Reactor Site	Number of Reactors	Distance (km)	Thermal (max.) Power(GW)	Max. Flux ($10^5\bar{\nu}_e\mathrm{cm}^{-2}\mathrm{s}^{-1}$)	Max. Event Rate (events/kt-year)
Kashiwazaki	7	160	24.6	4.25	348
Ohi	4	180	13.7	1.90	154
Takahama	4	191	10.2	1.24	102
Hamaoka	4	214	10.6	1.03	84
Tsuruga	2	139	4.5	1.03	84
Shiga	1	81	1.6	1.08	89
Mihama	3	145	4.9	1.03	84
Fukushima-1	6	344	14.2	0.53	44
Fukushima-2	4	344	13.2	0.49	40
Tokai-II	1	295	3.3	0.17	14
Shimane	2	414	3.8	0.10	8
Ikata	3	561	6.0	0.08	7
Genkai	4	755	6.7	0.05	4
Onagawa	2	430	4.1	0.10	8
Tomari	2	784	3.3	0.02	2
Sendai	2	824	5.3	0.03	3
Total	51	—	130	13.1	1,075

Table 2.1: Expected $\bar{\nu}_e$ rates detected in KamLAND produced in different reactors No neutrino oscillation is assumed. Thermal power, flux, and event rates are of the maximum operation of the reactors. Annual averages are about 80% of the maximum.

The produced positron deposits its energy via ionization and subsequently annihilates with an electron in the liquid scintillator. The neutron is, on the other hand, thermalized and captured as follows.

$$\mathrm{n} + \mathrm{p} \rightarrow \mathrm{d} + \gamma \tag{2.2}$$

The energy of the emitted photon is 2.2MeV. The mean neutron capture time of the neutron is obtained about 200μs so that we may have clear $\bar{\nu}_e$ events with the introduction of the delayed coincidence between the prompt positron signal (with photons from its annihilation) and the delayed neutron capture γ-ray. This occurs when the energy of $\bar{\nu}_e$ satisfies the threshold energy of the reaction which is given by $\mathrm{m_n} - \mathrm{m_p} + \mathrm{m_{e^+}} \simeq 1.8\mathrm{MeV}$. Here, $\mathrm{m_n}$, $\mathrm{m_p}$ and $\mathrm{m_{e^+}}$ are the mass of neutron, proton and positron, respectively. Actually, the candidate of the $\bar{\nu}_e$ event is restricted by the cut, such as the 1MeV energy deposit

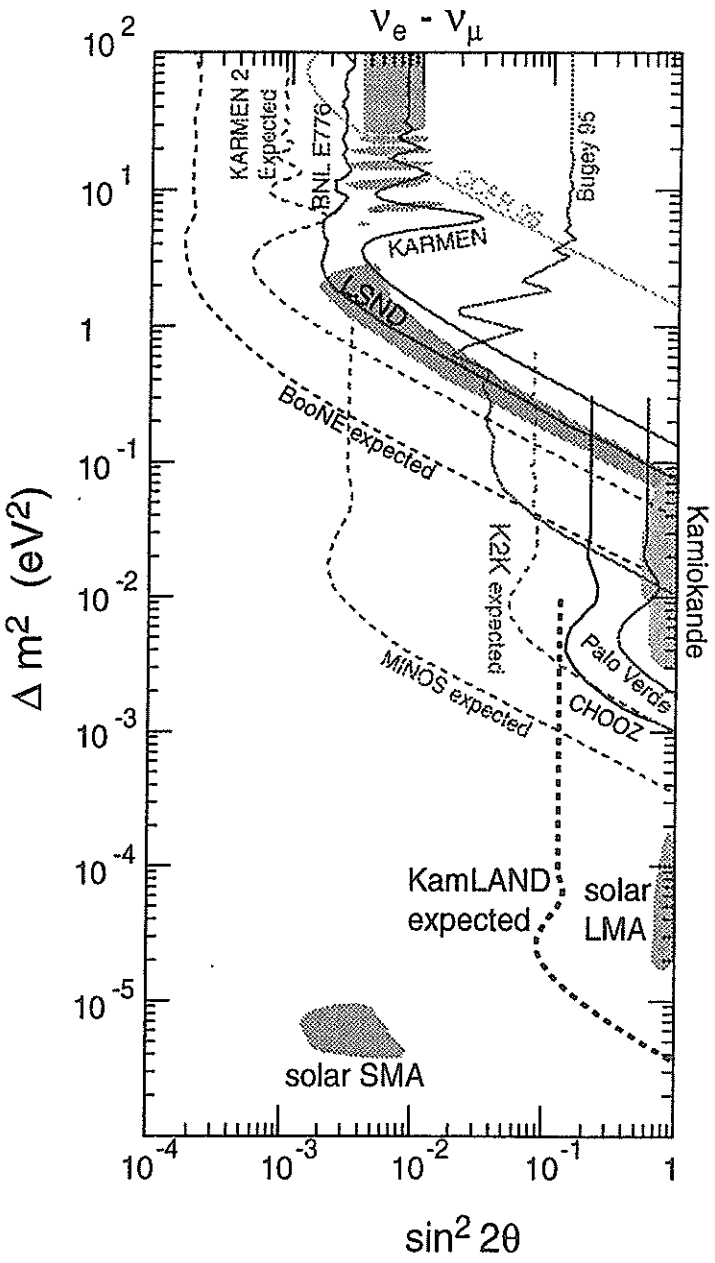

Fig. 2.3: Δm^2 - $\sin^2 2\theta$ plane for ν_e - ν_μ oscillations covered by different accelerator, reactor, and solar neutrino experiments with 90% CL limits
The region obtained by the Kamiokande atmospheric results is today rejected by the Super-Kamiokande results.

iment. It is of the long baseline and low antineutrino energy so that it will reach a very different sensitivity, $\triangle m^2 \leq 10^{-5}$ eV^2 which other neutrino oscillation experiments have never experienced.

$\triangle m^2$ - $\sin^2 2\theta$ plane for ν_e - ν_μ oscillations covered by some accelerator, reactor, and solar neutrino experiments is shown in Figure 2.3. Results obtained by many experiments are relevant to the atmospheric anomaly region, $\triangle m^2 \simeq 10^{-3}$ - 10^{-2} eV^2. Actually, Bugey[3], CHOOZ[4] and Palo Verde[5] are reactor neutrino experiments, while K2K[6], MINOS[7], BooNE[8], BNL E776 and LSND[9] use high energy neutrino from $\pi^\pm$ or $K^\pm$ decay, which are produced in the accelerators. KARMEN[10] uses the neutrinos produced by the neutron spallation source, and Super-Kamiokande is the largest water Cerenkov detector experiment[1]. In KamLAND, however, 6×10^{-6} eV^2 in $\triangle m^2$ will be achieved.

In reactors, four isotopes such as ^{235}U, ^{238}U, ^{239}U and ^{241}Pu work as fuel. They absorb thermalized neutrons, which gives rise to nuclear fissions. Then, generated long chains daughter nucleus emit $\bar{\nu}_e$ via hundreds of different β-decay. It is thus possible to obtain only one flavor of neutrino such as $\bar{\nu}_e$. This flux and spectrum depend only on the composition of the core with respect to the four isotopes, which varies with time passage. But this composition will be calculated each day so that we can obtain the neutrino flux with small uncertainties.

In Table 2.1, 16 Japanese commercial nuclear power plants are considered. Distance from Kamioka, maximum thermal power, flux etc. are introduced as well. $\bar{\nu}_e$ flux of 1.3 $\times 10^6$ cm^{-2}s^{-1} are expected in Kamioka site for $E_{\bar{\nu}_e} > 1.8$MeV at maximum power from the reactors in Table 2.1. 80% of the reactors are positioned between 140km and 210km away. This gives the limited range of baselines. The total number of events expected from reactors is 1,075 kt^{-1}yr^{-1} at maximum power with 100% live time of the detector.

Nuclear reactors produce $\bar{\nu}_e$s isotropically in the β-decay of the neutron rich fission fragments. These events are detected using the delayed coincidence between positron emission (with photons from its annihilation) and the gamma from neutron capture. $\bar{\nu}_e$ reacts with a proton in the liquid scintillator in the detector through the following reaction.

$$\bar{\nu}_e + p \rightarrow e^+ + n \tag{2.1}$$

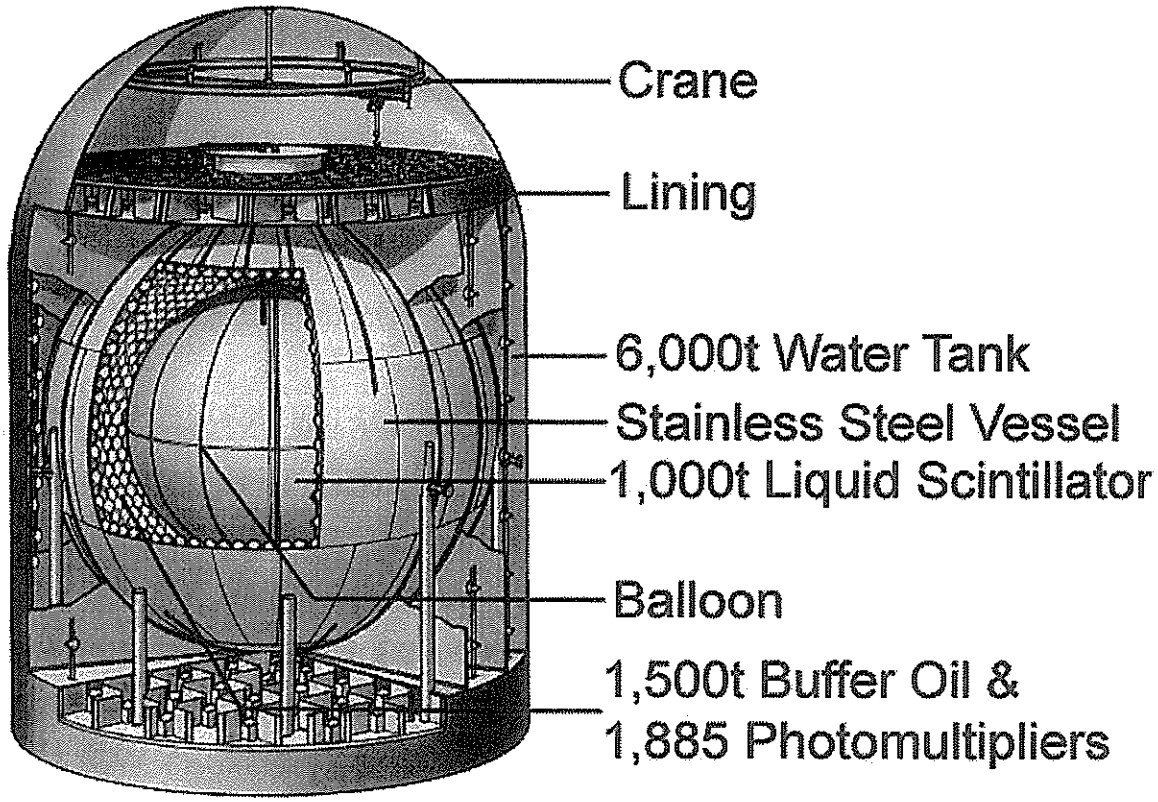

Fig. 2.2: Overall drawing of the KamLAND detector

pseudocumene in the oil mixed with the 1.5 g/l PPO. This retains most of the scintillator properties while substantially reducing flammability, toxicity and cost.

This developed liquid scintillator is, in fact, able to reject the backgrounds such as recoiled protons by fast neutrons and other internal radioactivity. The former ones can be reduced with the pulse shape discrimination (see Chapter 7 and Appendix A for more detail), and the latter ones can be done by purifying both liquid scintillator and buffer fluid continuously. It is necessary to reduce U, Th, and ^{40}K to at least 10^{-14}g/g for the reactor experiment and 10^{-16} for the solar neutrinos. The introduction of the purification system will help us to remove these contaminations as well as the radioactive nuclei produced initially and during the experiment by cosmogenic activation (mainly by ^{7}Be) and radon decay (^{210}Pb). And it will also remove the dissolved oxygen in the liquid scintillator with the nitrogen purging, which will improve the light output of the scintillator.

A large water purification system will be built to treat the water of the veto counter and to provide ultra-clean water for the scintillator plant.

The 17-inch PMTs are another developed detectors for KamLAND experiment in order to optimize the photon collection efficiency and physics reconstruction accuracy. The photocathode of 20-inch PMTs now used in Super-Kamiokande experiment is reduced so that we may improve the transit time spread(TTS) in the timing signals from the large area tube. On top of that, the slower venetian blind type in the multiplier section is replaced to the fast linear focusing type for better TTS. Actually, the TTS of the order of 3ns reduced from at most 10ns is obtained without losing the equivalent collection efficiency in 20-inch PMTs. The detailed specifications for both 17-inch and 20-inch PMTs are given in Chapter 3.

The whole KamLAND detector is shown in Figure 2.2.

2.3 Physics Interest

2.3.1 Reactor anti-neutrino

The first direct test of the large mixing angle MSW solution to the solar neutrino problem via the detection of $\bar{\nu}_e$ from reactors is one of the main subject of the KamLAND exper-

17m diameter spherical stainless tank contains 13m diameter, 80μ thin transparent plastic spherical balloon filled with the liquid scintillator and the buffer oil outer side of it. Also, 1,295 17-inch photomultiplier tubes(PMTs) and 590 20-inch PMTs will be installed with supported on a 9m radius stainless steel spherical vessel.

The buffer oil will support the slight difference of densities of the two liquids so that it may help to keep within 1% buoyancy generated in the innermost shell. It is composed of 60% concentration of the normal paraffin12(N12) and 40% concentration of the paraol 250(P250:isoparaffin), which are both paraffin oil. The normal paraffin12 is one of the main component of the liquid scintillator in order to keep the balance. This also enables us to reduce the background radioactivity chiefly either from rocks, or from the 17-inch PMTs.

The outer 5,400m^3 water tank will be used to identify a cosmic ray muon as a background. Inside this tank, 800 20-inch PMTs will be installed, which were used in the old Kamiokande experiment. They will work as the veto counter with the detection of the Cerenkov signals of muon generated in the shielding water. This water shield actually absorbs much of the radioactivity coming from the walls and moderates the fast neutrons produced by cosmic rays in the rock as well.

The liquid scintillator is in itself the most significant component of the KamLAND experiment. The Super-Kamiokande experiment uses a water Cerenkov detector which restricts the possible lower energy threshold value to around 5MeV due to the radioactive substance contained in the water. We are, however, aiming at the detection of energy deposit as low as several hundred keV. It will be possible only if the scintillator has excellent light output and optical clarity. The energy resolution will be improved as well because of high photon yield. However, KamLAND is such a large detector that we may also need to care about the attenuation length of the liquid scintillator.

Taking them into account, we have thus selected the scintillator which is composed of the pseudocumene (1,2,4-Trimethylbenzene) as a primary solvent with the PPO (2,5-Diphenyloxazole) as a primary fluorescence. Actually, the normal paraffin12 is diluted with the pseudocumene as a co-solvent in order to keep the flash point of the fluid above the value required in Kamioka site. After all, the compounds of the liquid scintillator are determined to be 80% concentration of the normal paraffin12 and 20% concentration of the

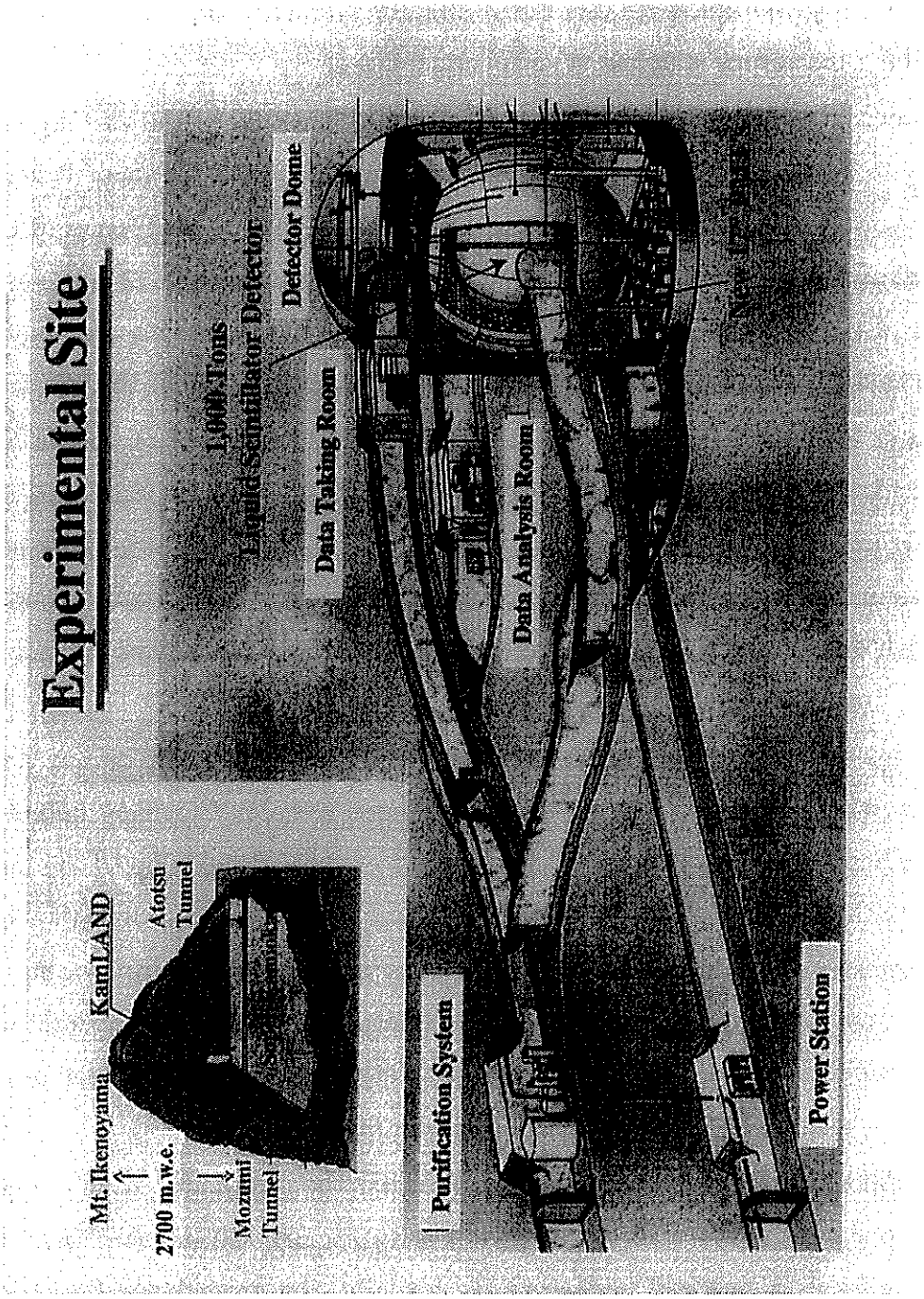

Fig. 2.1: View of the KamLAND detector site

Chapter 2

KamLAND Experiment

KamLAND provides a variety of physics topics with its pure, gigantic liquid scintillator detector. In this chapter, the possibilities of physics in KamLAND and its detector are discussed. Background estimation in KamLAND is also introduced as well.

2.1 The Detector Site

The KamLAND detector will be sited in the old Kamiokande detector cavity more than 1,000m (2,700 m.w.e.) under the top of Mt. Ikenoyama, which is about 500m away from the Super-Kamiokande detector currently operated under the same mountain. The rock surrounding the detector has the average rock density of 2.7g/cm^3 in this location. Actually, it is studied that the flux of muon at the surface is attenuated with the factor of 10^5 and then is 1.3×10^{-3} m^{-2}s^{-1} at the detector[2].

It is expected to have radioactivity during the detector construction and operation, especially radon. Thus, the radon barriers will be installed for radon reduction in the detector cavity and experimental area walls with a special impermeable polyurethane coating.

The site and location of the detector is shown in Figure 2.1.

2.2 The Detector Overview

The detector mainly consists of two concentric spherical shells and the outer purified water tank. The former ones are for 1,000 tons of ultra-pure liquid scintillator at the center and for the ultra-pure buffer oil which surrounds the liquid scintillator shell. Namely, the

$$\sin^2(2\theta_{\rm m}) = \sin^2(2\theta)[\sin^2(2\theta)+(\frac{\rm L_{vac}}{\rm L_e}-\cos 2\theta)^2]^{-1} \tag{1.13}$$

The resonance occurs in $\rm L_{vac} = L_e \cos 2\theta$, and $\sin^2(2\theta_{\rm m}) = 1$ yields the maximum oscillation. The mass eigenstates is adiabatically transferred from ν_e to ν_μ by the multi-oscillation between the resonance width, $\Gamma = 2\sin 2\theta$. This is the description of the MSW effect.

flavours cannot. Especially, it occurs in the Sun, causing the almost complete conversion of solar neutrinos of the electron type to neutrinos of a different flavour. This process is known as the Mikheyev-Smirnov-Wolfenstein(MSW) effect.

Again, only two neutrino flavours are considered for the simplicity, then the time evolution of the flavour eigenstates in matter is expressed by the Schrödinger equation

$$i\frac{\mathrm{d}}{\mathrm{dt}}\begin{pmatrix} |\nu_e\rangle \\ |\nu_\mu\rangle \end{pmatrix} = \mathrm{H}\begin{pmatrix} |\nu_e\rangle \\ |\nu_\mu\rangle \end{pmatrix}, \tag{1.7}$$

where $\mathrm{H} \cong \mathrm{E} + \frac{1}{2\mathrm{E}}(\mathrm{M}^2 + 2\mathrm{EV})$ ($\mathrm{M}^2 = \mathrm{U}\begin{pmatrix} \mathrm{m}_1^2 & 0 \\ 0 & \mathrm{m}_2^2 \end{pmatrix}\mathrm{U}^{-1}$ is the mass matrix and the potential $\mathrm{V} = \begin{pmatrix} \mathrm{V}_e + \mathrm{V}_\mu & 0 \\ 0 & \mathrm{V}_\mu \end{pmatrix} = \begin{pmatrix} \mathrm{V}_e & 0 \\ 0 & 0 \end{pmatrix}$). Subtracting E from H yields

$$2\mathrm{EH} = \frac{1}{2}(\mathrm{m}_1^2 + \mathrm{m}_2^2 + \mathrm{A})\begin{pmatrix} 1 & 0 \\ 0 & 1 \end{pmatrix} + \frac{1}{2}\begin{pmatrix} \mathrm{A} - \triangle\mathrm{m}^2\cos 2\theta & \triangle\mathrm{m}^2\sin 2\theta \\ \triangle\mathrm{m}^2\sin 2\theta & -\mathrm{A} + \triangle\mathrm{m}^2\cos 2\theta \end{pmatrix} \tag{1.8}$$

The mass eigenvalue for ν_e and ν_μ is

$$\mathrm{m}^2 = \frac{1}{2}(\mathrm{m}_1^2 + \mathrm{m}_2^2 + \mathrm{A}) \pm \frac{1}{2}[(\triangle\mathrm{m}^2\cos 2\theta - \mathrm{A})^2 + \triangle\mathrm{m}^4\sin^2 2\theta]^{\frac{1}{2}}, \tag{1.9}$$

where $\mathrm{A} = 2\mathrm{EV}_e = 2\sqrt{2}\mathrm{G_F}\mathrm{N}_e\mathrm{E}$, and $\mathrm{G_F}$ and N_e are the electron number density and the Fermi coupling constant, respectively. Therefore, solving the Schrödinger equation, we obtain

$$i\frac{\mathrm{d}}{\mathrm{dt}}\begin{pmatrix} |\nu_e\rangle \\ |\nu_\mu\rangle \end{pmatrix} = 2\pi\begin{pmatrix} \frac{1}{\mathrm{L}_e} - \frac{\cos 2\theta}{\mathrm{L_{vac}}} & \frac{\sin 2\theta}{2\mathrm{L_{vac}}} \\ \frac{\sin 2\theta}{2\mathrm{L_{vac}}} & 0 \end{pmatrix}\begin{pmatrix} |\nu_e\rangle \\ |\nu_\mu\rangle \end{pmatrix} \tag{1.10}$$

Here, $\mathrm{L}_e = \frac{\sqrt{2}\pi}{\mathrm{G_F}\mathrm{N}_e(\mathrm{t})}$ is the neutrino-electron interaction length. When neutrinos travel in matter with its constant electron density, the oscillation probability becomes

$$\mathrm{P}(\nu_e \to \nu_\mu) \;=\; \sin^2 2\theta_\mathrm{m}\sin^2\frac{\pi\mathrm{L}}{\mathrm{L_m}} \tag{1.11}$$

$\mathrm{L_m}$ and θ_m are the matter oscillation length and the mixing angle in matter, respectively, given by

$$\mathrm{L_m} = \mathrm{L_{vac}}[1 - 2\frac{\mathrm{L_{vac}}}{\mathrm{L}_e}\cos 2\theta + (\frac{\mathrm{L_{vac}}}{\mathrm{L}_e})^2]^{-\frac{1}{2}}, \tag{1.12}$$

and

Actually, $|\nu_i\rangle$ propagates as a free particle so that it may evolve as in the following wave function (1.2) at time t by solving the Schrödinger equation,

$$|\nu_i(\mathrm{t})\rangle = \mathrm{e}^{-i\mathrm{H_i t}}|\nu_i(0)\rangle, \tag{1.2}$$

where H is the Hamiltonian whose eigenvalue is given by the energy, E, and hence, $\mathrm{H}_i = \mathrm{E}_i = \sqrt{\mathrm{p}^2 + \mathrm{m}_i^2} \cong \mathrm{E} + \frac{\mathrm{m}_i^2}{2\mathrm{E}}$ (i = 1, 2) (p denotes the momentum, and $\mathrm{m}_i \ll \mathrm{p}$). Substituting (1.2) into (1.1), we obtain

$$\begin{aligned} |\nu_i(\mathrm{t})\rangle &= \sum_i \mathrm{U}_{l,i}\mathrm{e}^{-i\mathrm{H_i t}}|\nu_i(0)\rangle \\ &= \mathrm{U}_{l,i}\mathrm{e}^{-i\mathrm{H_i t}}\mathrm{U}^{\dagger}_{i,l}|\nu_l(0)\rangle \end{aligned} \tag{1.3}$$

Assuming only three neutrinos are relevant for (1.1), we treat U as a unitary 3 × 3 matrix. However, neutrino oscillation experiments are often analyzed in a simplified way by assuming only two neutrino flavours mixing, for instance, e and μ. The mixing matrix U then depends upon only one mixing angle θ, which is thus given as in (1.4).

$$\mathrm{U} = \begin{pmatrix} \cos\theta & \sin\theta \\ -\sin\theta & \cos\theta \end{pmatrix} \tag{1.4}$$

After all, the oscillation probability which retains the same flavour as in the one at t = 0 is

$$\begin{aligned} \mathrm{P}(\nu_e \rightarrow \nu_e) &= |\langle\nu_e(0)|\nu_e(\mathrm{t})\rangle|^2 \\ &= 1 - \sin^2 2\theta \sin^2 \frac{\mathrm{m}_1^2 - \mathrm{m}_2^2}{4\mathrm{E}}\mathrm{t} \\ &= 1 - \sin^2 2\theta \sin^2 1.27\frac{\triangle\mathrm{m}^2(\mathrm{eV}^2)\mathrm{L(meter)}}{\mathrm{E(MeV)}} \end{aligned} \tag{1.5}$$

Here, $\triangle\mathrm{m}^2 \equiv \mathrm{m}_1^2$ - m_2^2. And hence the oscillation length in vacuum is given by

$$\begin{aligned} \mathrm{L_{vac}} &= 2\pi\frac{2\mathrm{E}_\nu}{\triangle\mathrm{m}^2} \\ &= \frac{2.48\mathrm{E}_\nu\mathrm{(MeV)}}{\triangle\mathrm{m}^2(\mathrm{eV}^2)}\mathrm{(meter)} \end{aligned} \tag{1.6}$$

1.3 MSW Effect

Neutrino oscillations are also experienced in matter. This happens because electron neutrinos can forward scatter on electrons by charged current interactions while other neutrino

with the expectations, such as $(\bar{\nu}_\mu + \nu_\mu)/(\bar{\nu}_e + \nu_e)$ to be around 2. Since cosmic rays are nearly isotropic one would expect to see the same effect in all directions but one experiment observed a dependence of the ratio on the direction of observation. Actually, the zenith angle is simply related to the neutrino path length, thus, one expects that the lepton yield will have a dependence on the zenith angle[1]. These observations of the apparent deficit of muon neutrino became known as the atmospheric neutrino anomaly and almost definitive with the recent Super-Kamiokande results. As well, the solar neutrino experiments indicate the massive neutrino.

To solve these problems, higher sensitivity experiments are required. KamLAND is one of such experiments challenging to find the possibility of neutrino oscillations. This will be able to cover one of the possible solutions of the solar neutrino problem. This is further explained in Chapter 2. And to perform the KamLAND project, preliminary experiments are necessary to establish the experimental techniques required for the KamLAND experiment as well as to evaluate the performance of the integrated detector system. The Test Bench Facility which is modeled upon the KamLAND detector system will help us to do them, and also to find unexpected defects of detectors and require the final decision of the most appropriate detectors for use. This is explained in detail in Chapter 3.

1.2 Vacuum Oscillation

In the Standard Model, neutrinos are treated as massless particles, if ever, extremely small. However, there are experimental deviations which implies the possibility of the massive neutrino. They could be explained by some form of neutrino flavour oscillations, since the massive neutrino is allowed to have a leptonic mixing matrix similar to a quark mixing matrix. Thus, the states of the massive neutrino has a definite mass, such as the mass eigenstates which propagate as plane waves in vacuum, and are not necessarily the partners of the charged leptons coupled to the vector bosons $W^{\pm}$ in doublets such as the weak eigenstates. The weak eigenstates $|\nu_l\rangle$ will be in such a case of the linear superpositions of the mass eigenstates $|\nu_i\rangle$ with the leptonic mixing matrix $U_{l,i}$,

$$|\nu_l\rangle = \sum_i U_{l,i}|\nu_i\rangle \tag{1.1}$$

Chapter 1

Introduction

The Standard Model describes the electromagnetic and weak interactions of quarks and leptons. This model conserves the lepton number due to the postulation of the massless neutrinos. Negligible neutrino-magnetic moments and no massive weakly interacting particles are defined as well within this model. However, the model contains a large number of parameters whose values are not explained and which must be determined from experiments. Also, the symmetries of the model are postulated, not derived, from an underlying principle. The massless neutrino is as well, in this respect. In this chapter, the motivation for non-zero neutrino mass, and the extension of the standard model are introduced in terms of the neutrino oscillations.

1.1 Motivation for Non-Zero Neutrino Mass

There are experimental problems which indicate the necessity of the massive neutrino. They motivate to investigate the presence of the neutrino oscillations. They are classified mainly into two problems such as the solar neutrino problem and the atmospheric neutrino anomaly. Solar neutrino problem is further discussed in Chapter 2 so here in this section, brief explanation about the atmospheric neutrino anomaly is introduced.

At some higher energies, the neutrino flux on earth is dominated by those produced by cosmic rays impinging upon the earth's atmosphere. Then, nitrogen and oxygen nuclei produce pions, which subsequently decay via $\pi^{\pm} \rightarrow \mu^{\pm}\nu_{\mu}(\bar{\nu}_{\mu})$, and $\mu^{\pm} \rightarrow e^{\pm}\bar{\nu}_{e}(\nu_{e})\nu_{\mu}(\bar{\nu}_{\mu})$. Early experiments measured a ratio of muon to electron type neutrinos that was inconsistent

Fire Services Act. These are arranged inside the 1.5m^3 acrylic vessel, where four 20-inch PMTs (later replaced to 17-inch PMTs) and 24 8-inch PMTs (not in use for this study) are mounted. Figure 3.1 shows the view of the overall apparatus, and two photographs in Figure 3.2 provide the practical idea of the Test Bench Facility.

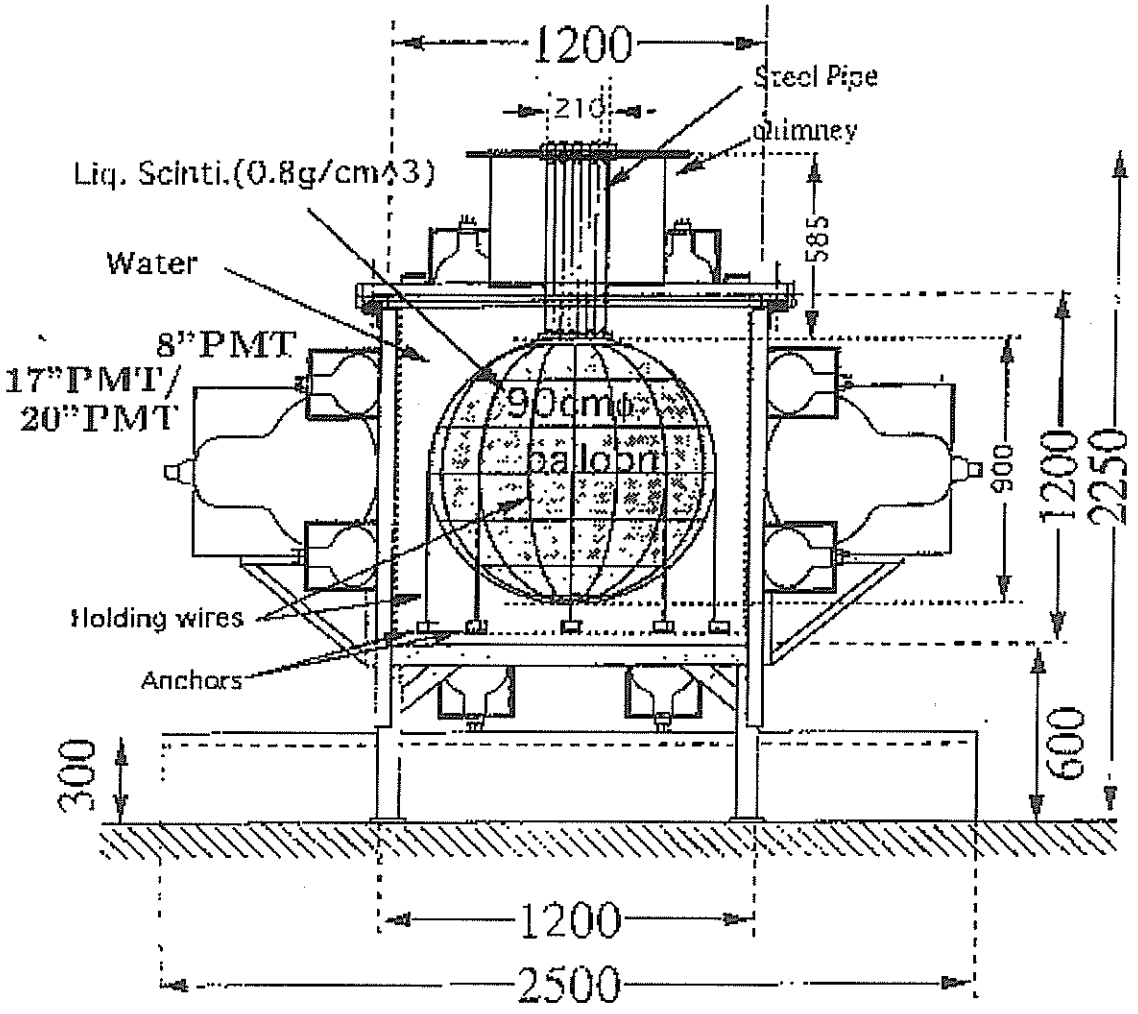

Fig. 3.1: Overview of the overall apparatus

In the following, some important detectors used in the Test Bench Facility are discussed, which may overlap in the previous chapter.

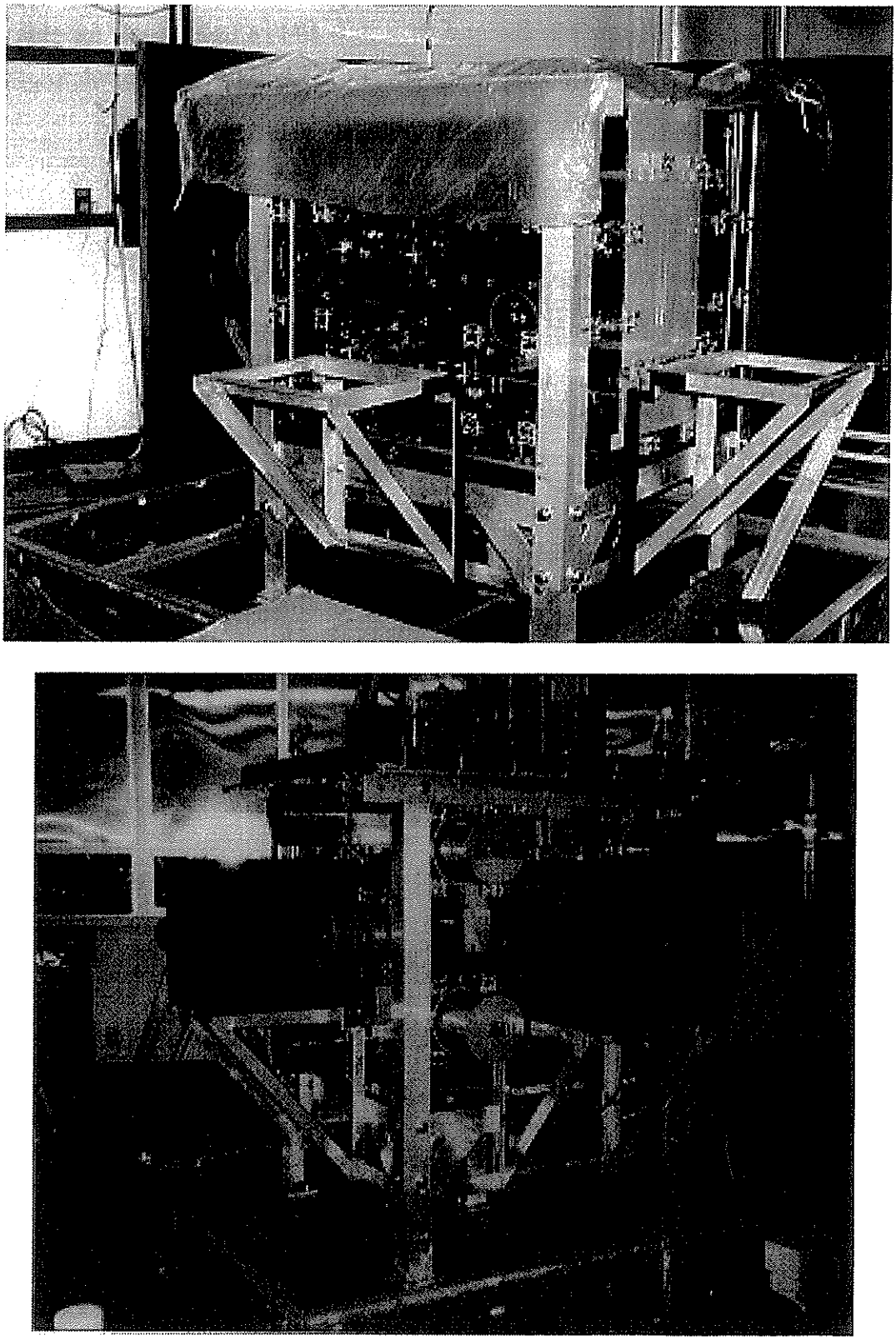

Fig. 3.2: Practical views of the Test Bench Facility

3.2.1 Liquid Scintillator

Most liquid scintillator experiments use gadolinium to improve the response to neutrons. KamLAND is, however, a deep and large detector, where backgrounds are intrinsically lower.

As explained in the previous chapter, the liquid scintillator for KamLAND experiment is chosen which is composed of 20% of the pseudocumene (1,2,4-Trimethylbenzene) as a primary solvent with 1.5 g/l of the PPO (2,5-Diphenyloxazole) as a primary fluorescence, as well as 80% of the normal paraffin12 as a co-solvent. In the early stage of the planning for KamLAND project, the isoparaffin of paraol 250 was supposed to be used as a co-solvent for the pseudocumene. Therefore, the composition of 20% of the pseudocumene and 80% of the isoparaffin mixed with the 2 g/l PPO for the liquid scintillator was adopted in the Test Bench Facility experiment. Although, the demands for the liquid scintillator such as the low pressure, high flash point, and low toxicity are satisfied. From now on, the liquid scintillator discussed below is what is mentioned above.

Particularly, it has a light yield of 50% of anthracene and attenuation length better than 12m (at $\lambda = 440$nm), resulting in an energy resolution of $\sigma(\mathrm{E})/\mathrm{E} = 10\%/\sqrt{\mathrm{E(MeV)}}$ (assuming 35% photocathode coverage, 20% photocathode quantum efficiency and 90% transmission from balloon). They are obtained from the laboratory tests performed before the Test Bench Facility installation, also giving a good pulse shape discrimination. Namely, the neutron contamination results in 6.5% for 90% gamma detection efficiency at $\mathrm{E}_\gamma >$ 1MeV.

3.2.2 Prototype Balloon

The central balloon is a very thin flexible membrane and isolates the liquid scintillator from the external buffer oil. The balloon is one of the extremely critical component of the detector in KamLAND. The material for the balloon should satisfy: radiologically pure, transparent for light in the $300 \sim 500$nm region, chemically inert to both the surrounding oil and the liquid scintillator, impermeable to radon gas, and the stability of its properties during the lifetime of the detector.

A single polymer film that provides all these properties is probably not available, so that a multi-layer sandwich structure balloon is developed. This consists of the sandwich of CN(60μm)/ON(25μm)/EVOH(12μm) /ON(25μm)/CN(60μm) and satisfies the required properties. In fact, the nylon CN/ON provides strength and compatibility with the oil and scintillator. Actually, CN is the low melting point nylon, while ON is the two axis-stretchable nylon. And the EVOH provides very low gas permeability. The EVOH is also the two axis-stretchable film and the hydrophily resin. Its chemical formula[21] is given by

$$-(CH_2 - CH_2)_m - (CH_2 - CH)_n-$$
$$\qquad\qquad\qquad\qquad\qquad\qquad\qquad\qquad\qquad\qquad\qquad\qquad\quad |$$
$$\qquad\qquad\qquad\qquad\qquad\qquad\qquad\qquad\qquad\qquad\qquad\qquad\quad OH$$

ethylene component vinyl alcohol component

The laboratory test indicates 70% for the transparency of this sandwich-film and 2×10^{-10} uranium content. Also, the radon permeability is reported 0.001×10^{-10} cm^2/s in terms of the diffusion length. And this balloon endures the pressure of at least $\sim$ 200 g/cm for one year experiment in the Test Bench Facility.

The overview of the prototype balloon used in the Test Bench Facility is shown in Figure 3.3 and the balloon installed in the Test Bench Facility is shown in Figure 3.4.

3.2.3 Photomultiplier

17-inch PMTs are already explained in the previous chapter, so here in this section, general characteristics of the 17-inch PMT are listed in Table 3.1 given below, with the comparison to both 20-inch in Table 3.2 and 8-inch PMTs in Table 3.3 installed in the Test Bench Facility. Cross sections of 17-inch and 20-inch PMTs are shown in Figure 3.5 (Top:20-inch PMT/Bottom:17-inch PMT). Actually, in most stage of the experiment, 20-inch PMTs are used instead of 17-inch PMTs.

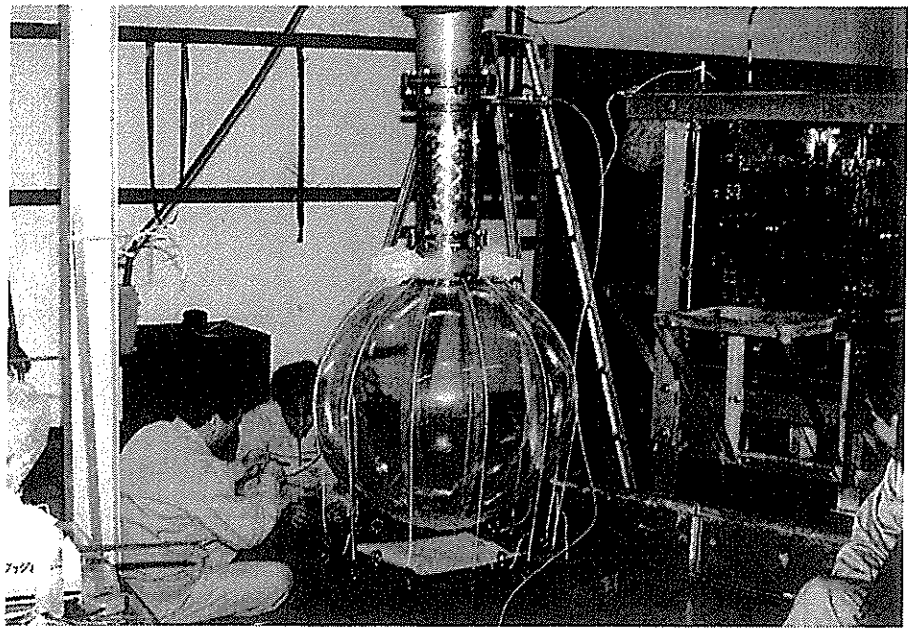

Fig. 3.3: Overview of the prototype balloon
The rightside apparatus is the Test Bench Facility

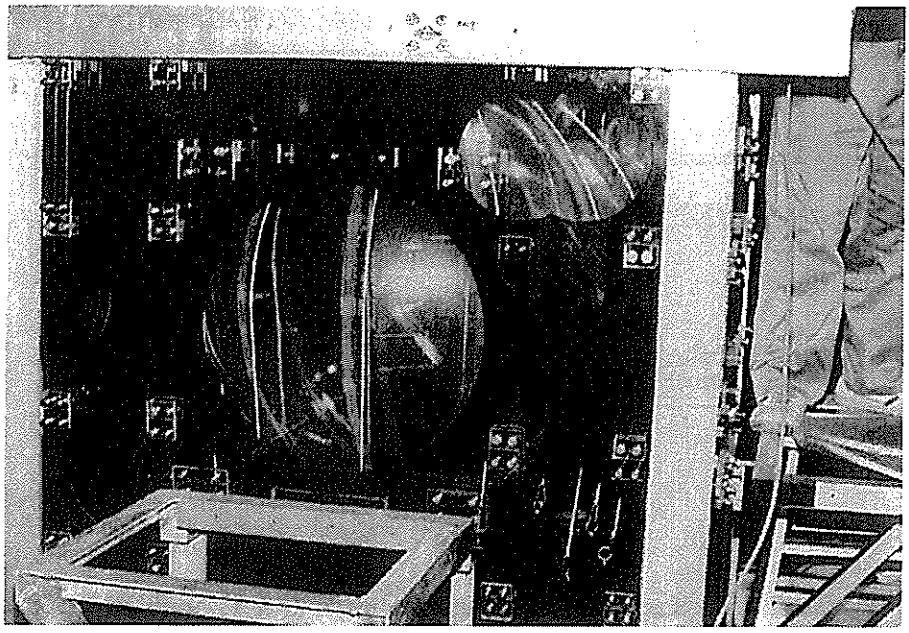

Fig. 3.4: Prototype balloon installed in the Test Bench Facility

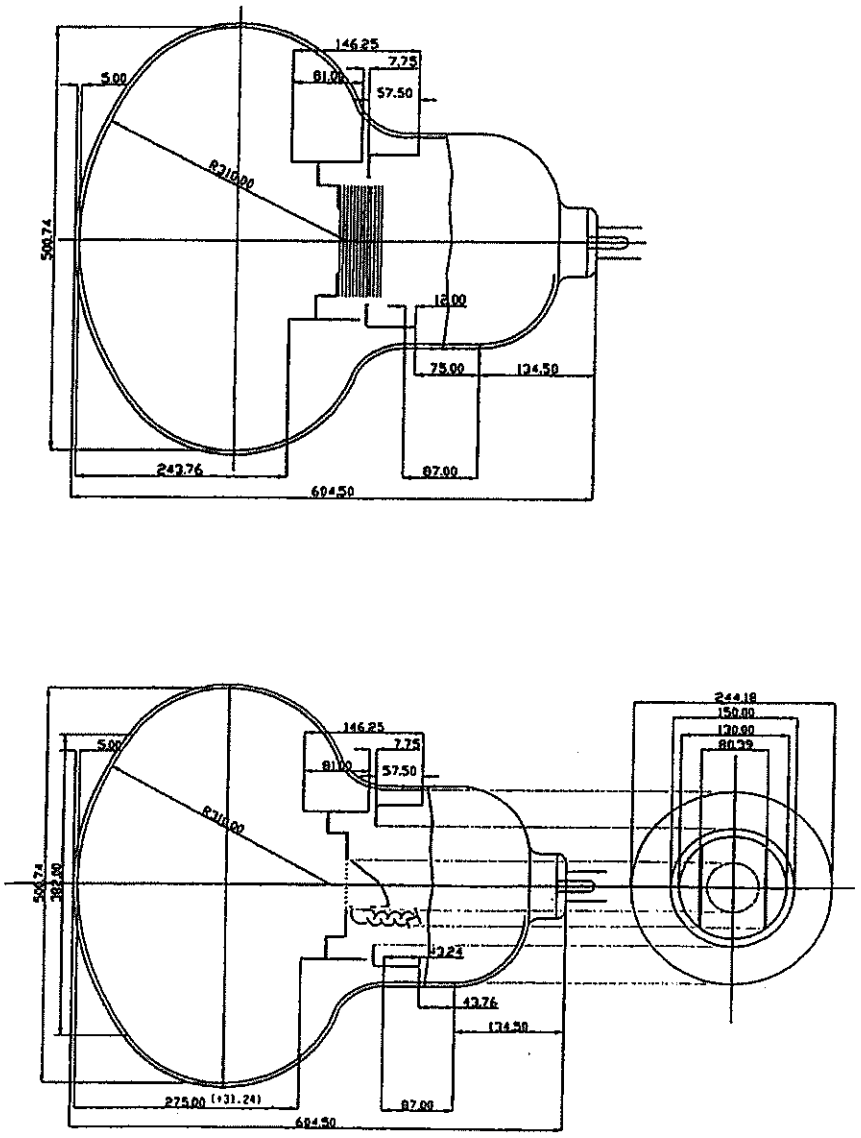

Fig. 3.5: Cross sections of 20-inch PMTs and 17-inch PMTs

Parameter	Minimum	Typical	Maximum	Unit
Cathode Quantum Efficiency at 480nm	20	22	-	%
Supply Voltage for Gain of 10^7	1,600	2,300	2,500	V
Anode Dark Current** (after 30min. storage in darkness)	-	83	400	nA
Anode Dark Pulse Rate** > 0.25p.e.	-	25	60	kHz
Transit Time Spread* (FWHM with 1p.e. detection)	2	3.1	4.0	ns
Anode Pulse Rise Time*	-	7	9	ns
Transit Time*	-	110	130	ns
Peak-to-Vally Ratio*	1.8	3.3	6.0	-
After Pulse(0.15~30μs after Main Pulse)	-	-	7	%

Table 3.1: Characteristics of 17-inch PMT(R7250)
(*:at 10^7 gain. *:at 10^7 and 25°C.)

Parameter	Minimum	Typical	Maximum	Unit
Cathode Quantum Efficiency at 390nm	20	23	-	%
Supply Voltage for Gain of 10^7	1,500	-	2,500	V
Anode Dark Current** (after 30min. storage in darkness)	-	-	1,000	nA
Anode Dark Pulse Rate** > 0.25p.e.	-	30	100	kHz
Transit Time Spread* (FWHM with 1p.e. detection)	-	6	-	ns
Anode Pulse Rise Time*	-	10	15	ns
Transit Time*	-	90	-	ns
Peak-to-Vally Ratio*	1.1	-	-	-
After Pulse(0.15~30μs after Main Pulse)	-	-	1	%

Table 3.2: Characteristics of 20-inch PMT(R3600)
(*:at 10^7 gain. *:at 10^7 and 25°C.)

Parameter	Minimum	Typical	Maximum	Unit
Cathode Quantum Efficiency at 420nm	-	22	-	%
Supply Voltage for Gain of 10^7	-	1,500	1,800	V
Anode Dark Current** a(after 30min. storage in darkness)	-	50	700	nA
Anode Dark Pulse Rate** > 0.25p.e.	-	4	8	kHz
Transit Time Spread* (FWHM with 1p.e. detection)	-	2.4	-	ns
Anode Pulse Rise Time*	-	3.8	-	ns
Transit Time*	-	55	-	ns
Peak-to-Vally Ratio*	-	2.5		-
After Pulse(100ns~16μs after Main Pulse)	-	2	10	%

Table 3.3: Characteristics of 8-inch PMT(R5912)
(*:at 10^7 gain. *:at 10^7 and 25°C.)

Chapter 4

Energy Calibration with Radioactive Sources

The energy calibration converts essentially the detector data to the energy deposit. Gamma sources are used for calibrating the response of the detector. In this chapter, we shall see the calibration line as well as the energy resolution and the attenuation length of this detector to understand the properties of the detector in the Test Bench Facility.

4.1 Experimental Method and Setup

^{137}Cs, ^{60}Co and ^{207}Bi are used as the γ-ray sources providing energies of 0.662MeV (^{137}Cs), 0.569MeV and (0.569+1.063)MeV (^{207}Bi) and (1.173+1.773)MeV (^{60}Co) for determination of the calibration line. These four energy deposits are applied because of the restricted energy resolution of the liquid scintillator discussed later. The level diagram for each isotope is given in Appendix C. These sources are hung down to the middle of the balloon. Each of them is enclosed with the 4×4 cm^2 polyethylene bag which is tied with 2m Teflon-lined string. Both materials indicate the compatibility with the liquid scintillator. This is why gamma sources are adopted, which we would not have to worry about the energy loss at the polyethelene bag. In addition, the experiments discussed in the coming chapters require higher energy range to identify the energy of the prospective events. Figure 4.1 given below shows the arrangement of a source. And the schematic diagram for single-event measurement is shown in Figure 4.2. The system is triggered in coincidence with the four fired 20-inch (later replaced to 17-inch) PMTs, and each detected signal is converted to its

own charge at the Analog to Digital Converter (REPIC 16CH CS ADC, type RPC-022). High voltage is applied for all the four 20-inch PMTs to realize the 10^7 gain, which differs among them. Off-line charge summation for all the four signals are performed to obtain the energy spectra of the γ-rays. Actually, each ADC channel is well-calibrated with the test pulse input for the conversion into charge in terms of pico coulomb(pC). Here, the nitrogen gas bubbling of the liquid scintillator is well-performed beforhand to purge out the dissolved oxygen which reduces the light output. This is further discussed in the next chapter.

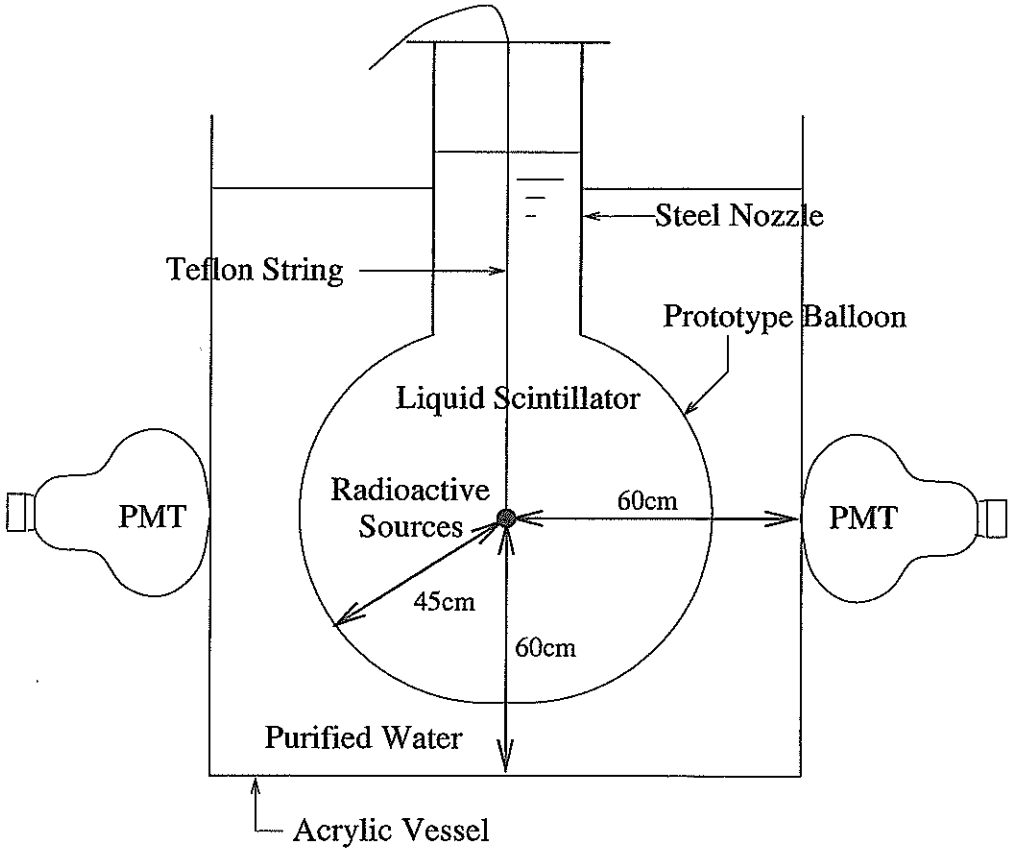

Fig. 4.1: Radioactive source arrangement in the Test Bench Facility

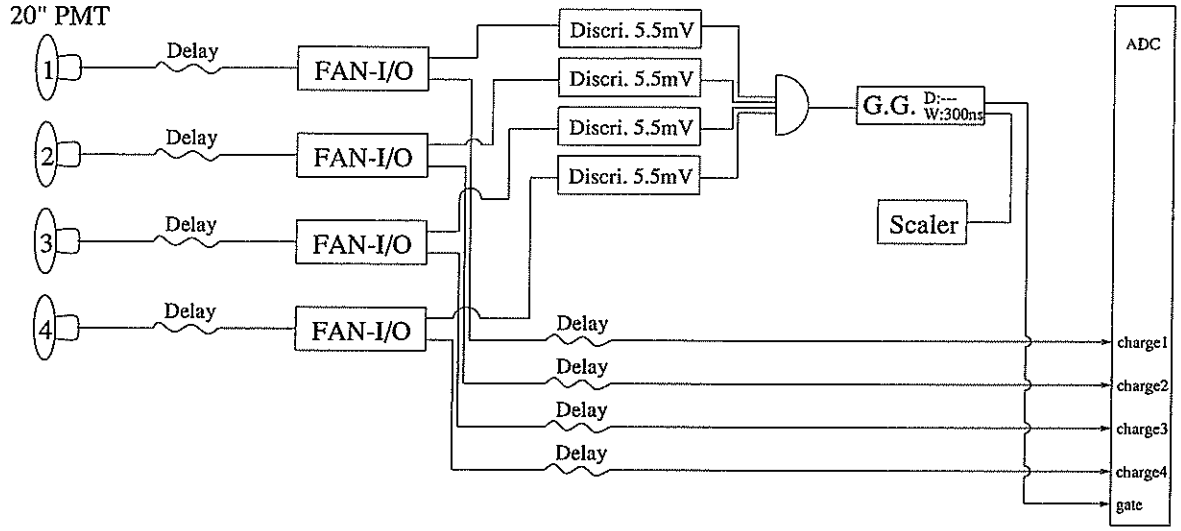

Fig. 4.2: Schematic block diagram for single event measurement

4.2 Results

The energy spectra for all gamma sources are given in Figure 4.5, 4.6 and 4.7, for ^{137}Cs, ^{60}Co and ^{207}Bi, respectively. And we can see the total absorption peaks in each spectrum with few Compton continuous spectrum (The mechanism of the Compton scattering is shown in Figure 4.3). The total absorption peak is produced when all the energy of gamma is deposited and absorbed inside the detector. This peak is mainly due to the photoelectric effect, or that of the low energy scattered γ-ray suffered multi-Compton scattering. Figure 4.4 is the example of the γ-ray cross sections in carbon[22].

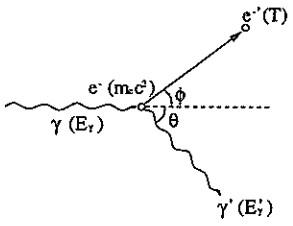

Fig. 4.3: Compton scattering mechanism
The energy distribution of the compton electron is represented by $T = \frac{(1-\cos\theta)E_\gamma/m_0c^2}{1+(1-\cos\theta)E_\gamma/m_0c^2}E_\gamma$, where θ varies from 0 to π.

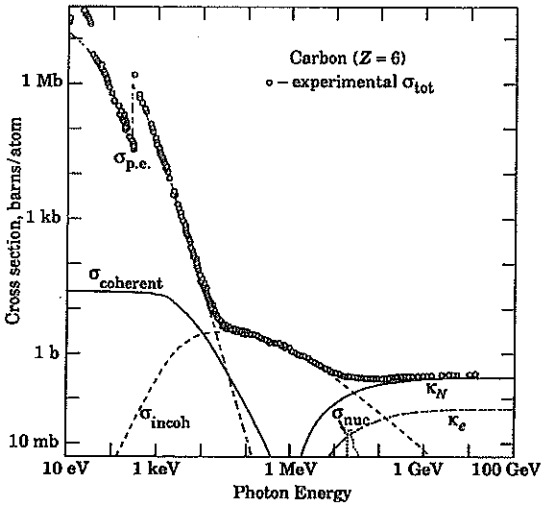

Fig. 4.4: γ-ray cross sections in carbon

Here, multi-gamma emitters such as ^{60}Co and ^{207}Bi show the sum peaks. This is because multi-gammas incident upon the detector and lose their energies at the same time within its resolving time. Literally, the peak indicates the summation of all the energy deposits. The clear appearance of the sum peak results from the high detection efficiency of the detector[23]. Poor energy resolution of the liquid scintillator is compensated with the larger size of the Test Bench Facility.

Actually, the calibration line is obtained with the four points, indicated with arrows in each spectrum. The relation is Energy(MeV) = 0.003 $\times$ Charge(pC) + 0.06 and shown in Figure 4.8. The error bars are given by 1σ of the total absorption peaks. It is confusing to identify 1.173MeV and 1.333MeV energy deposit emitted by ^{60}Co because of the restricted energy resolution and possibly small contribution of the overlapped Compton continuous spectrum of the summed energy deposit (1.173+1.333MeV), so that this is not adopted for the calibration line determination.

With the aid of this calibration line, the environmental background γ-rays from ^{40}K can be observed. This gamma deposits 1.46MeV as in Figure 4.9. This is found without any radioactive sources employment. This trigger rate is at most 4kHz compared to 35kHz, 567kHz and 36kHz for ^{137}Cs, ^{60}Co and ^{207}Bi employment, respectively.

The calibration line is also helpful to find the 2.2MeV energy deposit of the γ-ray emitted by the thermalized neutron capture on proton. Actually, the possible explanation for the slight variance of the peak would be explained by the energy deposit of the first recoiled proton scattered by the fast neutron from ^{252}Cf due to its high disintegration rate.

We shall now evaluate the energy resolution of the liquid scintillator based on the total absorption peaks obtained in the energy spectra. Actually, the statistical fluctuation is given within 1% due to the high statistics of 100,000 events. From the data represented in the spectra, $\sigma(\mathrm{E})/\mathrm{E} = 25.4\%$, 18.1% and 14.3% are obtained for ^{137}Cs, ^{60}Co and ^{207}Bi, respectively. And thus the resolution can be found as the energy function, $\sigma(\mathrm{E})/\mathrm{E} = 3.3 + 18.1\%/\sqrt{\mathrm{E(MeV)}}$ and shown in Figure 4.11. $\sigma(\mathrm{E})/\mathrm{E} = 10\%/\sqrt{\mathrm{E(MeV)}}$ is expected with the correction of the position dependence.

The attenuation length of the liquid scintillator is also evaluated by using two peaks in the spectrum of the ^{60}Co. Actually, the ^{60}Co used here has the high disintegration rate of 567kHz so that we may have the approximately 15% pile-up events in the 300ns gate. Assuming only the total absorption peaks observed, the escape probability of either 1.173MeV or 1.333MeV gamma can be found as 0.21 from the two Gaussian fitted areas in Figure 4.12. Here, only one gamma deposit contributes to the leftside peak, while the rightside peak is due to both gammas' deposits. This gives the 28.8cm of the attenuation length of the liquid scintillator. Thus, we could expect the suppression of ^{60}Co gammas in the buffer oil layer, emitted from the stainless frame in KamLAND.

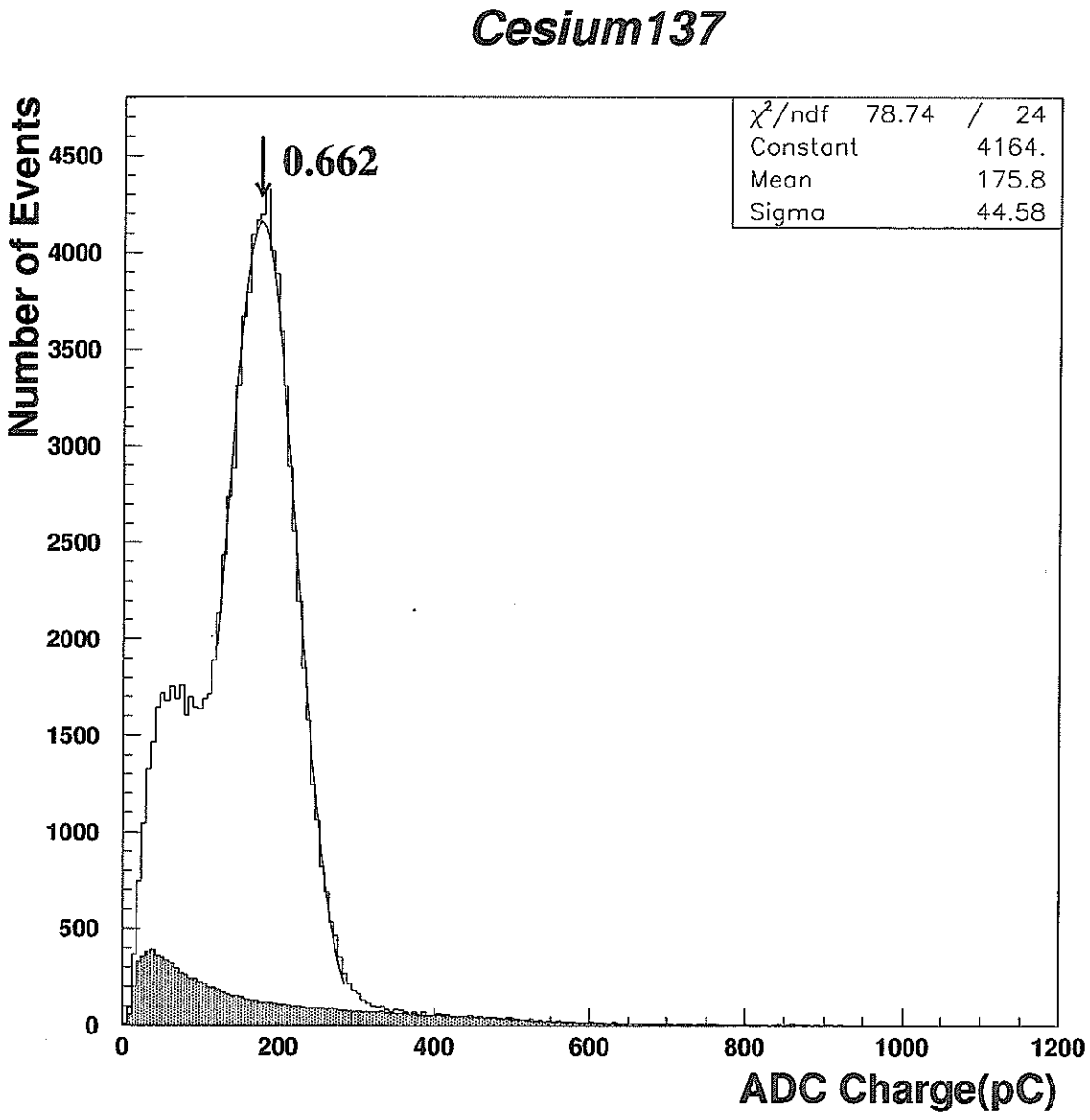

Fig. 4.5: Energy spectrum for ^{137}Cs
Dotted histogram shows the event rate normalized environmental background.

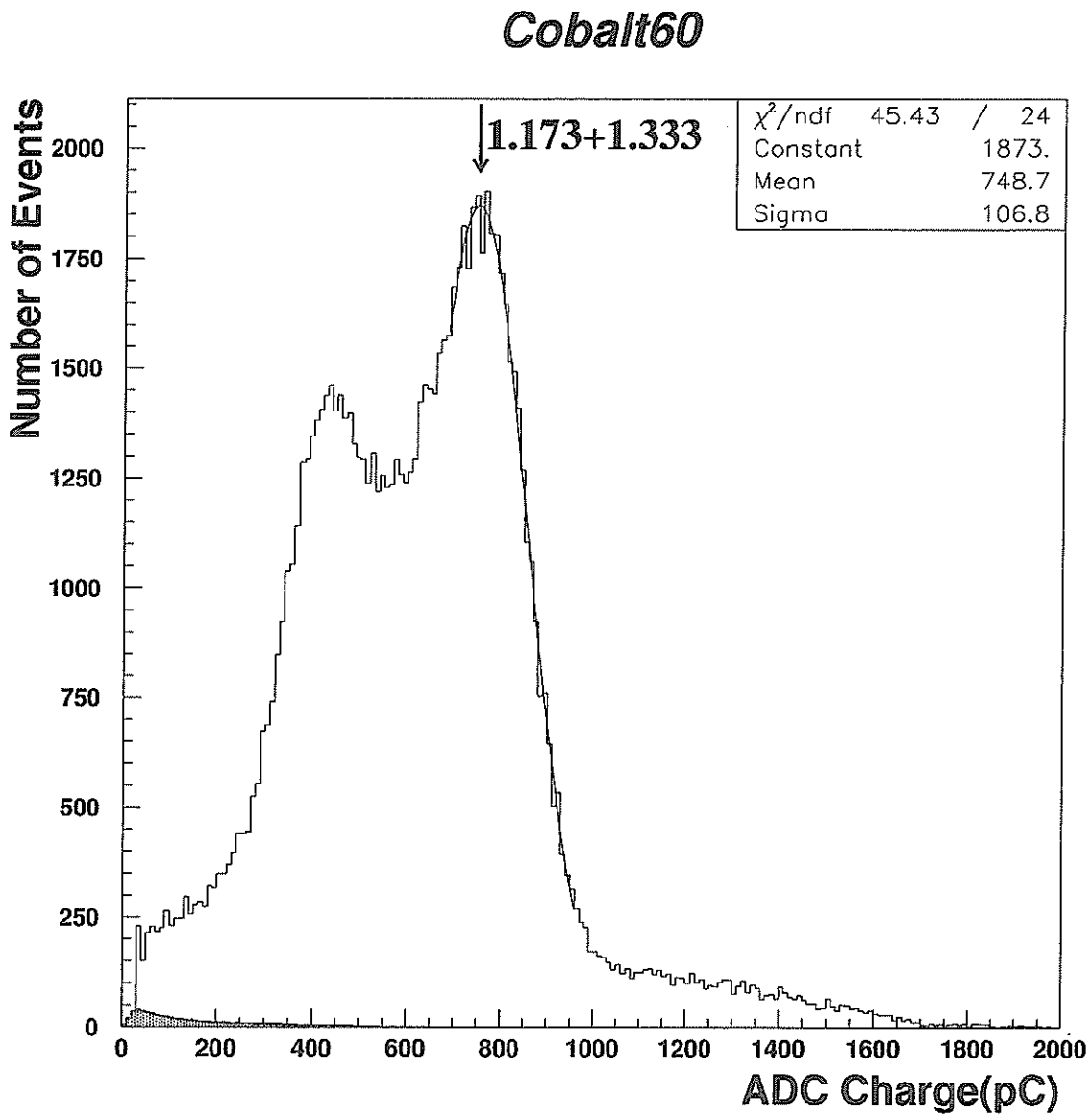

Fig. 4.6: Energy spectrum for ^{60}Co
Dotted histogram shows the event rate normalized environmental background.

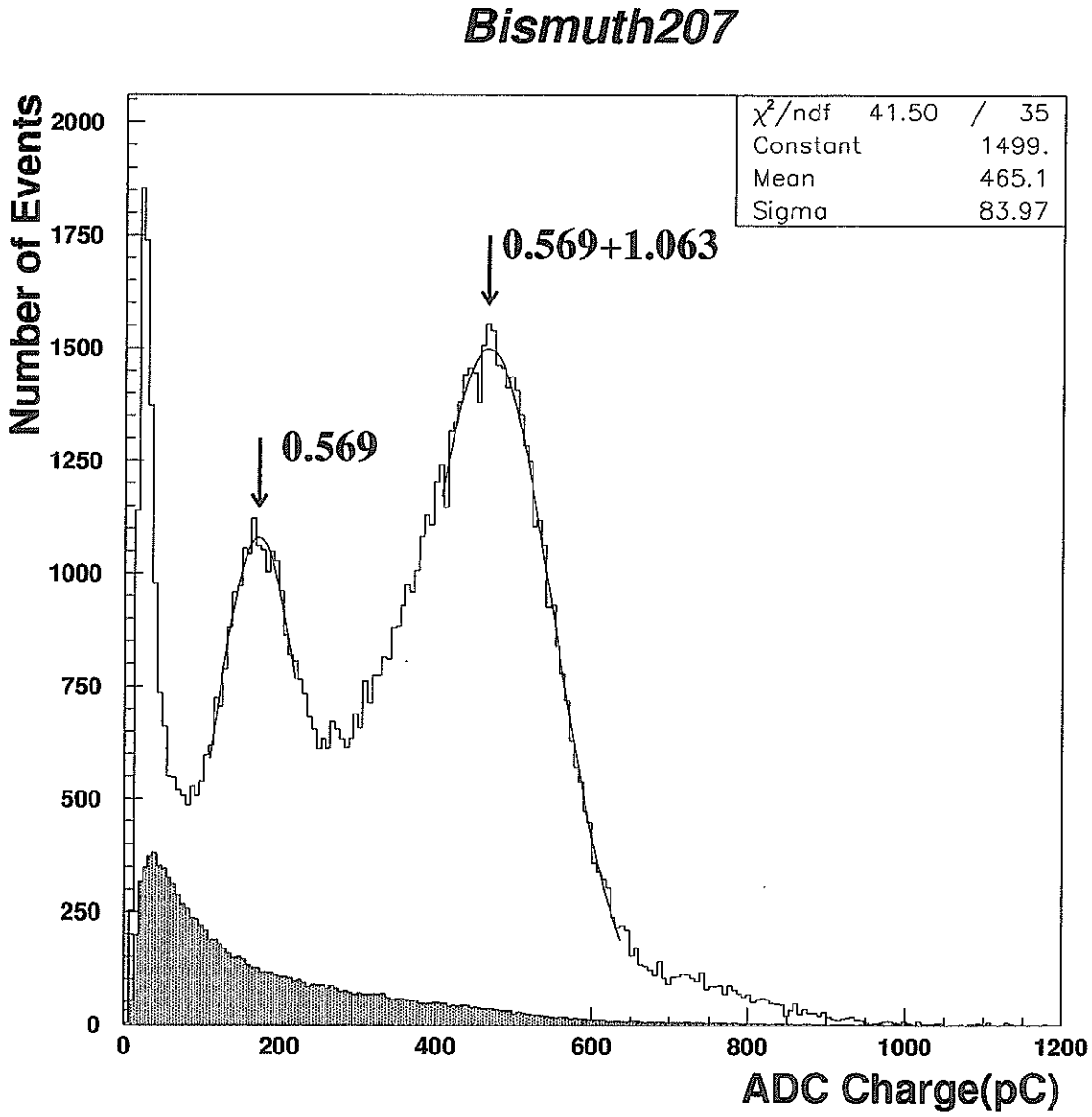

Fig. 4.7: Energy spectrum for ^{207}Bi
Dotted histogram shows the event rate normalized environmental background.

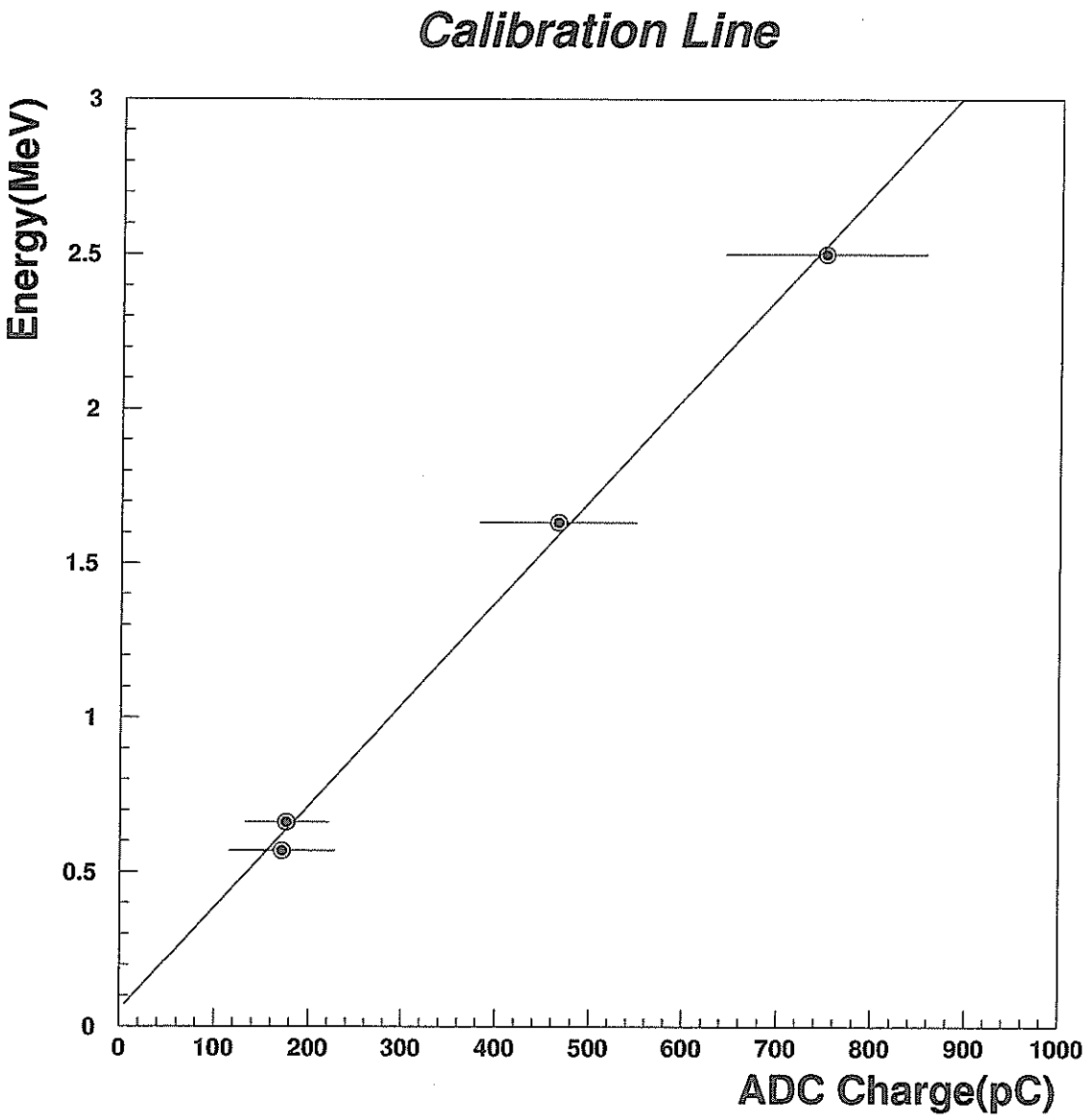

Fig. 4.8: Calibration line for four 20-inch PMTs charge summation
The relation, Energy(MeV) = 0.003 × Charge(pC) + 0.06 is obtained. The error bars are given by 1σ of the total absorption peaks.

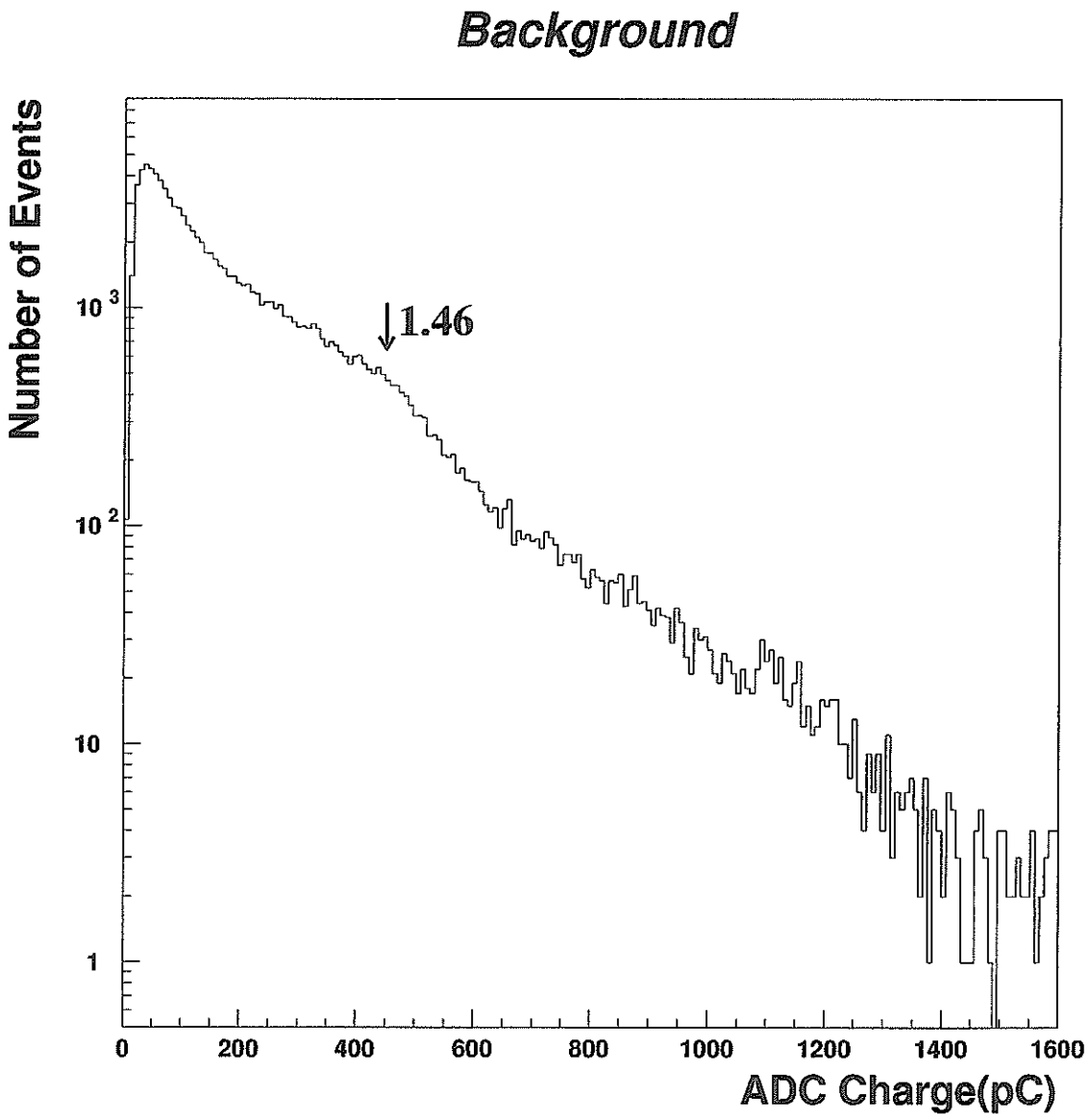

Fig. 4.9: Energy spectrum for environmental background
1.46MeV energy deposit of the γ-ray emitted by ^{40}K is identified through the obtained calibration line.

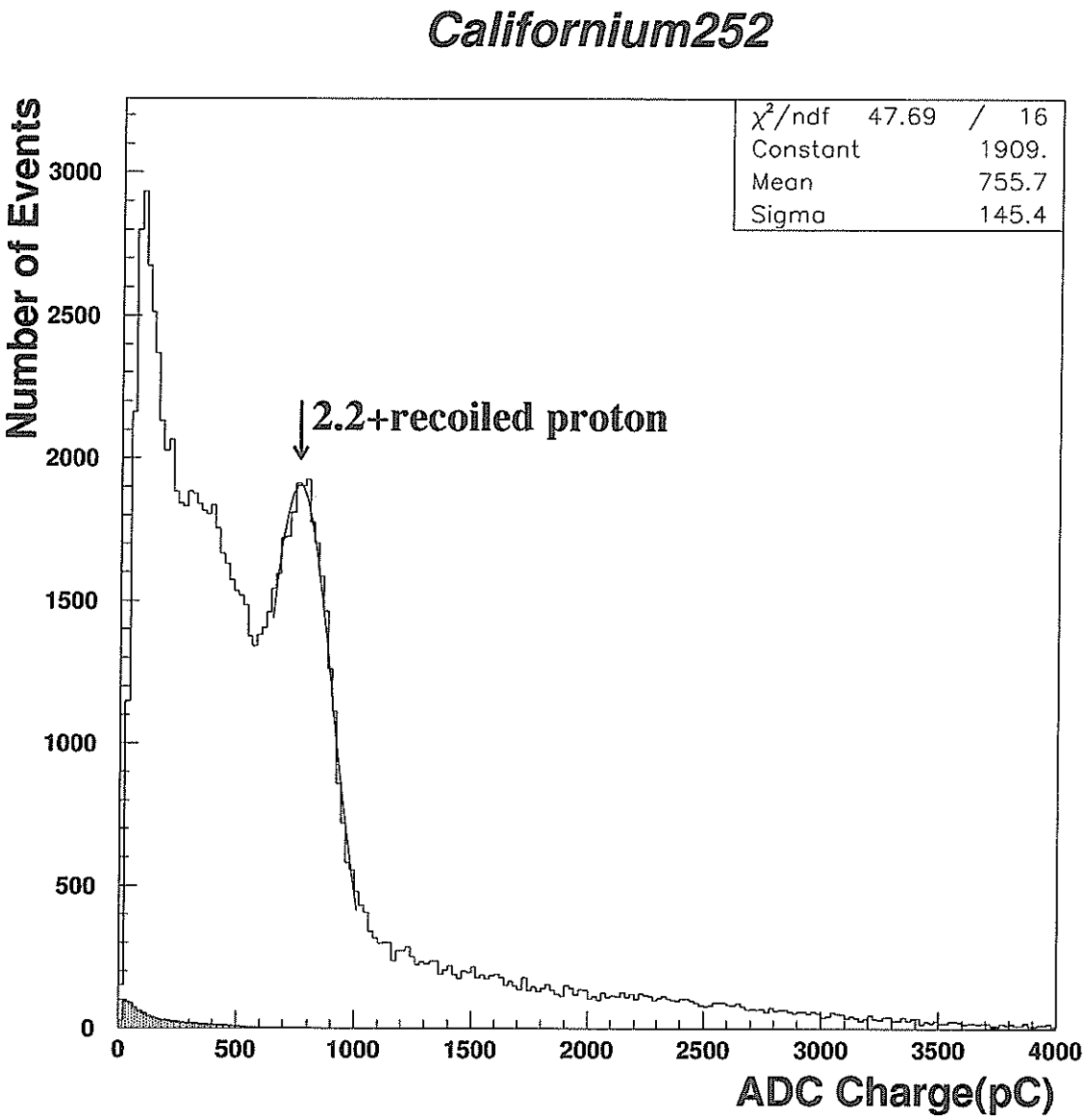

Fig. 4.10: Energy spectrum for ^{252}Cf
2.2MeV energy deposit of the γ-ray emitted by the thermalized neutron capture on proton is identified through the obtained calibration line. Actually, the possible explanation for the slight variance of the peak would be explained by the energy deposit of the first recoiled proton scattered by the fast neutron from ^{252}Cf due to its high disintegration rate.

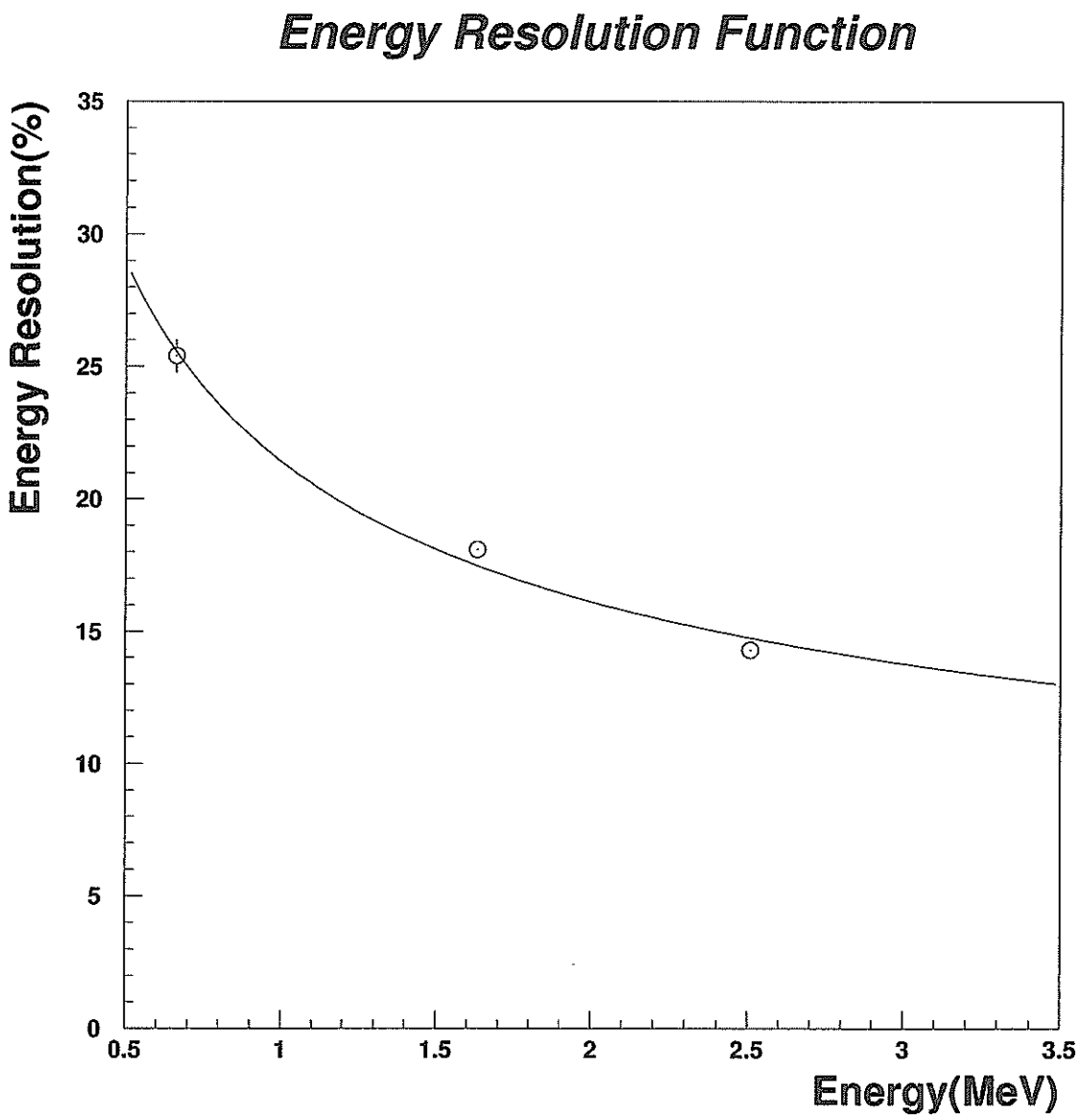

Fig. 4.11: Energy resolution function
The relation between the energy and its resolution is given by $\sigma(\mathrm{E})/\mathrm{E} = 3.3 + 18.1\%/\sqrt{\mathrm{E(MeV)}}$.

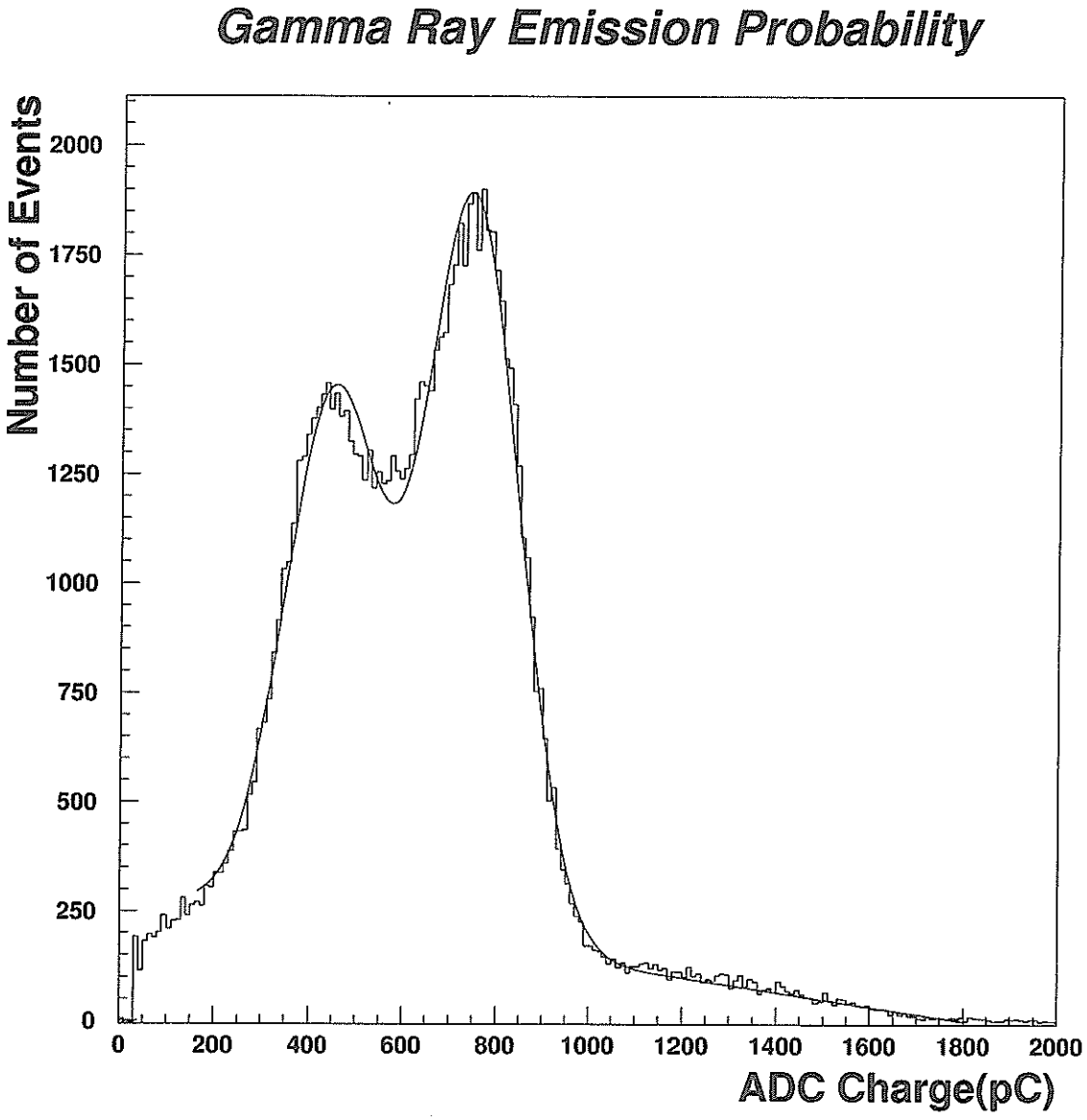

Fig. 4.12: Single and double gamma emission probability in the liquid scintillator Pile-up events can be seen above 950pC due to the high disintegration rate of the ^{60}Co source. The environmental background is subtracted in this histogram.

Chapter 5

Light Output Improvement with N_2 Gas Bubbling

Liquid scintillator has the great advantage of its high light yield, so that we can detect lower energy radiation. However, it is easy to be suffered from the self-absorption of incident radiation energy. This phenomenon is called quenching. In this chapter, we shall introduce the principle of the quenching, then discuss how to recover the light output from the oxygen quenching in the Test Bench Facility with the nitrogen gas bubbling.

5.1 Quenching

As mentioned, some incident radiation upon the liquid scintillator undergo the quenching so that their intrinsic energies are, in fact, shifted to the lower side. In the following, the quenching itself is classified for each stage of the energy transfer in the liquid scintillator.

Radiation Energy
↓ ← chemical & oxygen quenching
Solvent
↓ ← chemical & oxygen quenching
Solute ← concentration quenching
↓ ← colour quenching
PMT

- Chemical quenching

  This quenching occurs before the fluorescence emission of the solute and depends mainly on the chemical characteristics of the scintillator. Either the formation of the exciplex or the spin-orbit interaction contributes this quenching.

  Exciplex is the excited complex of the intermolecular compound, which is composed of two different molecules. Especially, the exciplex produced in the collision between the excited solvent molecules and the quencher molecules is significant. Once this kind of exciplex is formed, the chemical quenching occurs by either one of the following processes.

$$
\begin{array}{c}
{}^1\mathrm{M}^* + \mathrm{Q} \rightarrow (\mathrm{M}^{\pm} \cdot \mathrm{Q}^{\mp})^* \rightarrow \mathrm{M}^{\mp} + \mathrm{Q}^{\pm(1)} \\
\swarrow \quad \searrow \\
{}^3\mathrm{M}^* + \mathrm{Q}^{(2)} \rightarrow {}^1\mathrm{M} + \mathrm{Q}^{(3)}
\end{array}
$$

  1. Dissolution
  2. Intersystem crossing to the excited triplet state
  3. Transition to the ground state

  Here, ^{1}M and ^{3}M are the singlet and triplet state of the solvent molecule, and Q is the quencher molecule.

  The quenching due to the spin-orbit interaction is relevant for heavy atoms. This interaction is enhanced under their existence so that the intersystem crossing between the singlet and triplet states is prompted, which results in the quenching.

- Colour quenching

  Under the presence of the material which has the absorption band overlapped with the emission band of the solute, part of the emitted fluorescence is absorbed and this results in the colour quenching. This is different from the chemical quenching in that the former occurs after the emission of the fluorescence of the solute.

- Oxygen quenching

  This quenching results from the dissolved oxygen in the liquid scintillator. The dissolved oxygen is the molecular-type oxygen dissolved in the liquid phase. This quenching is similar to the chemical one in terms of the energy transfer process.

  The oxygen molecule has the strong acceptance of electrons as the electron scavenger so that it is easy to form the exciplex with the excited singlet state of the solvent molecule, excited by the incident radiation. Once the exciplex is formed, the following reaction occurs, and thus results in the oxygen quenching.

$$^1M^* + {}^3O_2 \rightarrow \underbrace{(M^+ \cdot O_2^-)^*}_{\text{exciplex}} \rightarrow {}^1M + {}^3O_2$$

  Here, ^1M and $^3O_2$ are the singlet state of the solvent molecule and the triplet state of the oxygen molecule, respectively. Another possible reaction giving rise to the quenching is shown below.

$$^3M^* + {}^3O_2 \rightarrow {}^1M + {}^1O_2^*$$

  The excited singlet state of the oxygen molecule is chemically active so that it may form the peroxide with the solvent or give rise to the chemical luminescence. Nitrogen gas or argon gas bubbling for the liquid scintillator should help to remove the dissolved oxygen. However, this improvement would be cancelled if one exposes the liquid scintillator under the pressure of the atmosphere, which allows the dissolution of atmospheric oxygen into the scintillator. It takes approximately 60 minutes to reach the previous equilibrium state containing a certain dissolved oxygen.

- Concentration quenching

  The light output for the liquid scintillator depends on the concentration of the solute. In the case of the extremely high concentration brings about the reduction of the light

output due to the concentration quenching. This quenching is considered due to either the self-quenching or the self-absorption of the solute.

The self-quenching of the solute occurs when the excited state and the ground state of the solute molecules collide and interact with each other. High concentration gives more chances to form the excimer which results in the energy loss due to the internal conversion of the molecule. This phenomenon is given below.

$$^1\mathrm{F}^* + \mathrm{F} \rightleftharpoons (^1\mathrm{F} \cdot \mathrm{F})^* \rightarrow \mathrm{F} + \mathrm{F}$$

excimer

Here, F denotes the solute molecule. The excimer formation depends upon the temperature. The lower temperature environment should prompt its formation, while the dissolution of it occurs as the temperature rises.

The self-absorption of the solute is the light energy loss occurring where the emission band and absorption band of the solute overlap with each other. The self-absorption would increase in the high concentration or in the large overlapped area of both bands mentioned.

- Ionization quenching

  Heavy charged particles such as proton and α indicate higher energy loss dE/dx in the liquid scintillator. The passage of them results in the generation of the high density area of the ionized and excited molecules along the passage, which thus reduce the light output of the light yield. This is the mechanism of the ionization quenching[24].

5.2 Oxygen and Water Dissolution in the Test Bench Facility

Actually, the prototype balloon used in the Test Bench Facility is hydrophily resin[21] so that the water outside of the balloon can soak into the liquid scintillator. This clouds the balloon inside, and results in the reduction of the light output. Nitrogen gas bubbling removes the dissolved water as well as the dissolved oxygen.

Atmospheric oxygen may also invade the liquid scintillator during the employment of a radioactive source. Enclosing the apparatus after the rejection of the oxygen is desired. Otherwise, this is effective for approximately 1 hour under the exposure of the liquid scintillator to the atmosphere, as mentioned.

5.3 Experimental Method and Setup

The nitrogen gas is provided through the pipe from the nitrogen gas cylinder as shown in Figure 5.1. The gas flow rate is controlled manually. In this experiment, 2,300l N_2 gas is provided for four hours until the balloon became cleared. The laboratory test shows the dissolved water in the liquid scintillator does not bring about the quenching. But this water clouds the whole balloon which may degrade the light emission so that it is necessary to purge it out. Gas flow in the enclosed system should be paid attention as far as the pressure onto the balloon is concerned. We decided to provide the gas at most for four hours just in case. The light output variation is monitored by the variation of the sum peak of 1.63MeV (1.063+0.569MeV) total absorption peak of ^{207}Bi. The experimental method and conditions are the same as in the previous chapter.

5.4 Results

As in Figure 5.2, 20% improvement is obtained for 2,300l nitrogen gas bubbling, where is the equilibrium state inside the balloon. The bubbling effect to suppress the oxygen quenching is thus confirmed, and this improvement corresponds to the 10% that of the anthracene.

The difference between the KamLAND liquid scintillator detector and the Test Bench Facility is chiefly their size. The volume of the KamLAND liquid scintillator is approximately 3,000 times as large as that of the Test Bench Facility one. And the liquid scintillator in KamLAND is surrounded by the buffer oil, while that in the Test Bench Facility is surrounded by the purified water. The EVOH doesn't absorb the oil so that the balloon in KamLAND will not be suffered from the cloud effect as seen in the Test Bench Facility. Still, further attention is required especially in handling the calibration stuff, when oxygen

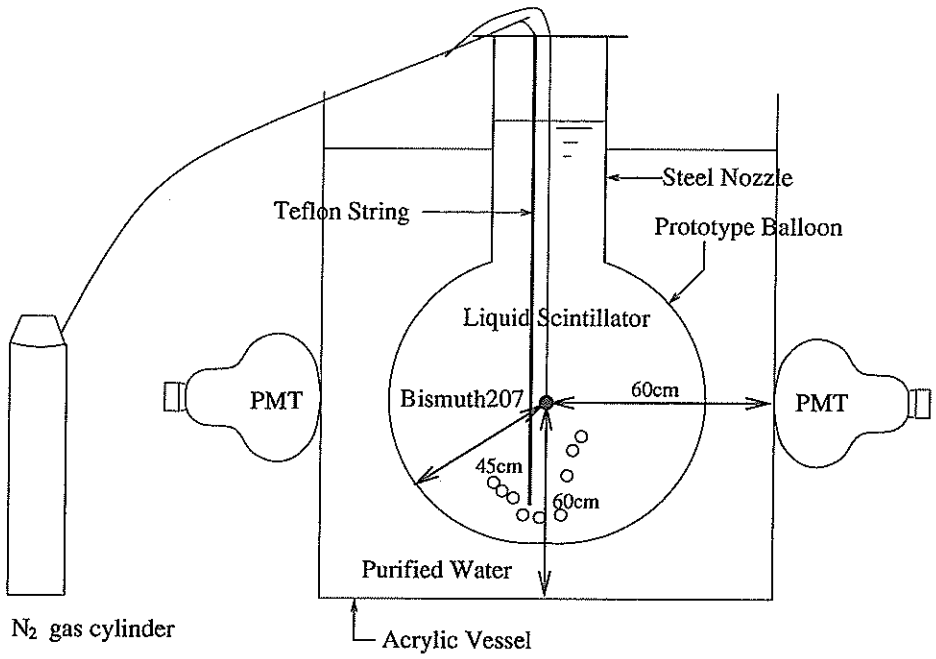

Fig. 5.1: Schematic diagram of the nitrogen gas bubbling experiment

or water would invade. KamLAND's gigantic detector size would assure little variance of the light output, expected from the results obtained here.

Rather, radon invasion is the crucial factor in KamLAND. The purified system will highly remove the radon by circulating and purifying the liquid scintillator. The Test Purified System is thus combined with the Test Bench Facility to study the performance of the circulation and purification of the liquid scintillator. The test in this system is further discussed in the next chapter. And in the experiments discussed in the next chapters are assumed the bubbling performed.

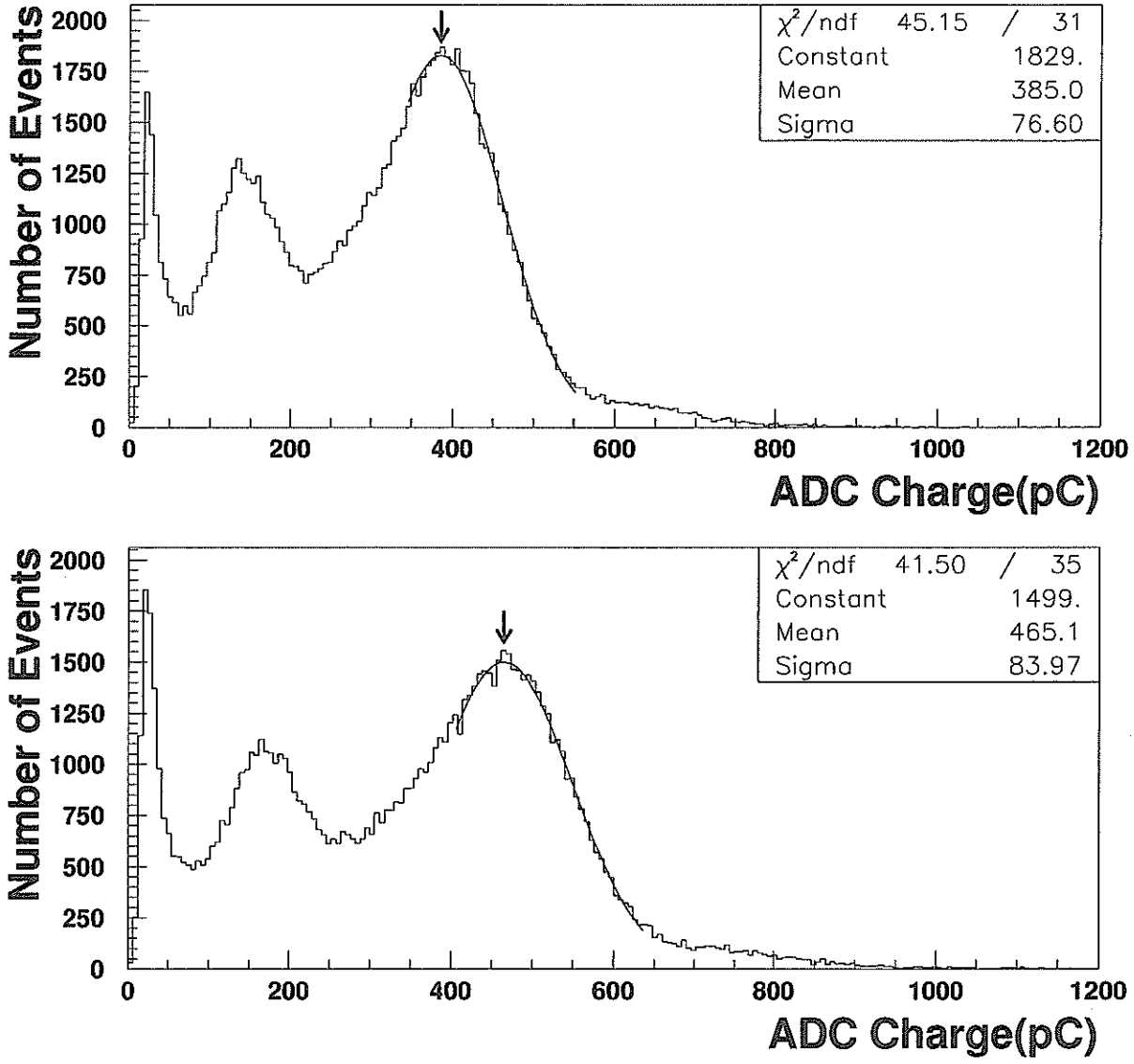

Fig. 5.2: Light output variation before and after the nitrogen gas bubbling
Top histogram gives the light output before the bubbling, and the bottom one shows after the bubbling.

Chapter 6

Light Output Improvement with the Test Purified System

In KamLAND, during the experiment lifetime both scintillator and buffer fluid will be continuously purified to reduce the background from internal radioactivity.

A prototype of the purified system has built to work with the Test Bench Facility, processing 20 l/hr of the scintillator. With such a detector we will be able to test the effects of purification down to 10^{-13} g/g of U and Th by detecting sequential decay in the decay chain. Here, the preliminary operation of this system is discussed to evaluate the light output improvement of the liquid scintillator with respect to the quantity of the dissolved oxygen in it.

6.1 Experimental Method and Setup

The system circulates the liquid scintillator 20 l/hr. Totally, 53-hour operation is performed. First, we shall see the variation of the oxygen concentration of the liquid scintillator under the system operation, then discuss the improvement of the light output with respect to the variation of the oxygen concentration. The overall view of this system is shown in Figure 6.1. The oxygen concentration was measured with the Oxygen Monitor (Portable Dissolved Oxygen Monitor, DO-25A, TOA Electronics Ltd.) 16 times for three days totally. Each measurement was performed approximately every 5 hours. The probe of this monitor was hung down about 5cm below the surface of the liquid scintillator. See Figure 6.2 for the arrangement of the probe as well as the ^{60}Co source.

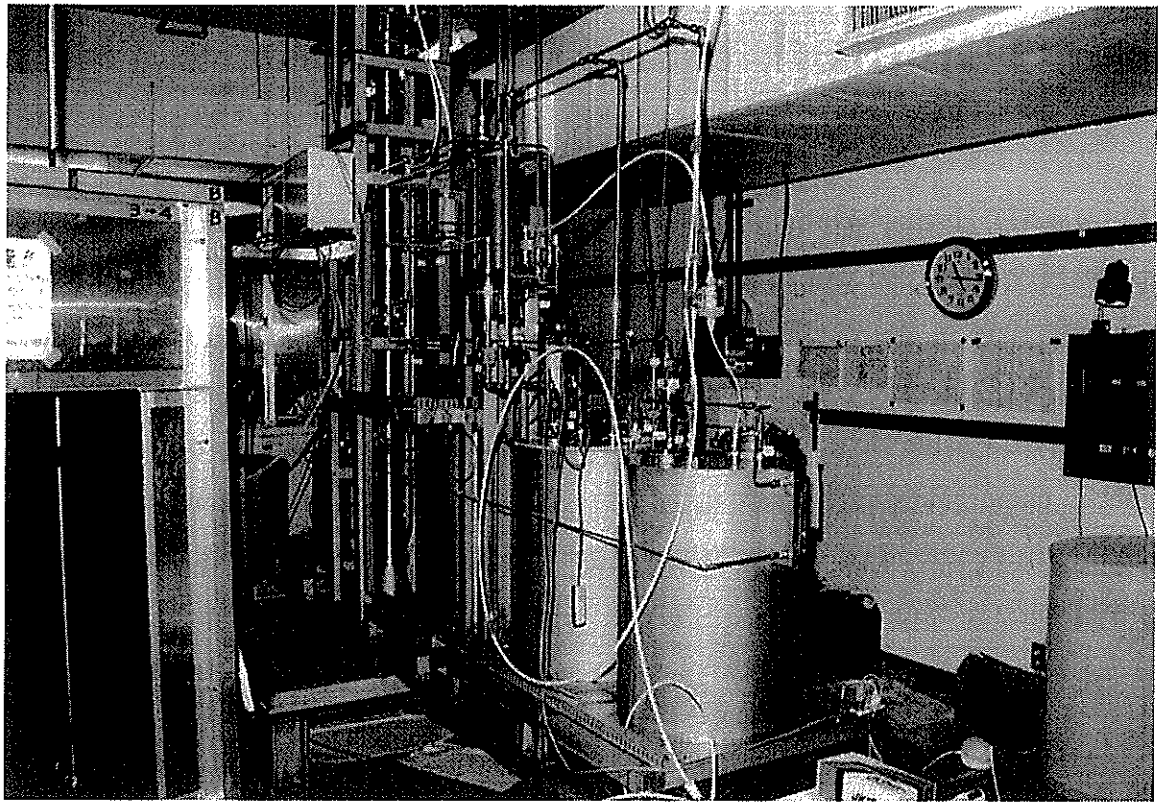

Fig. 6.1: Overview of the Test Purified System
The leftside apparatus is the Test Bench Facility

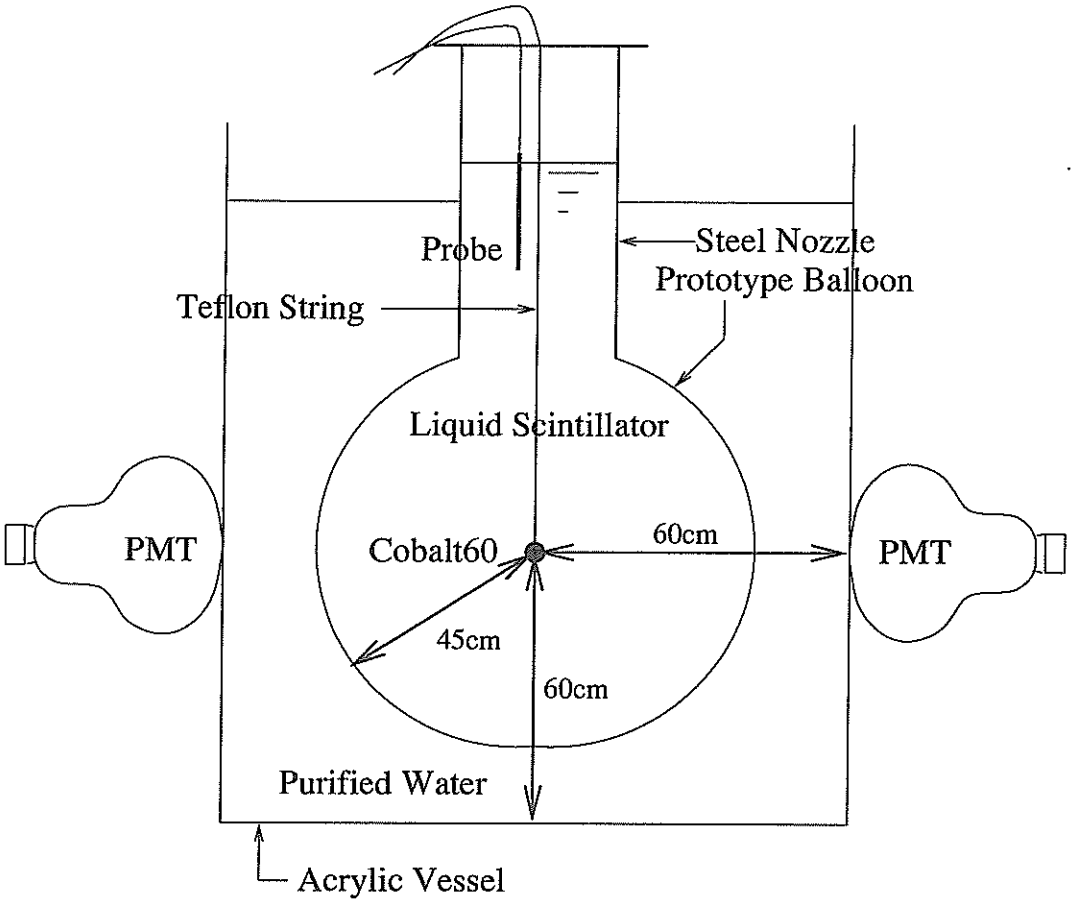

Fig. 6.2: Arrangement of the probe of the oxygen monitor and the ^{60}Co

Figure 6.3 shows the obtained results indicating the variation of the oxygen concentration. The vertical and horizontal axes denote the variation of the oxygen concentration in terms of percentage and the time evolution from the beginning of the system operation in terms of minutes, respectively.

The light output variation of the liquid scintillator was obtained by monitoring the variation of the γ-ray total absorption peak emitted by ^{60}Co source employed in the middle of the Test Bench Facility shown in Figure 6.2. Actually, the sum peak of 2.507MeV (1.173+1.333MeV) is used, which results from the summation of charges detected at all the four 17-inch PMTs. The experimental method and conditions are the same as described in Chapter 4 except for the PMTs for use presuming the essential calibration is performed.

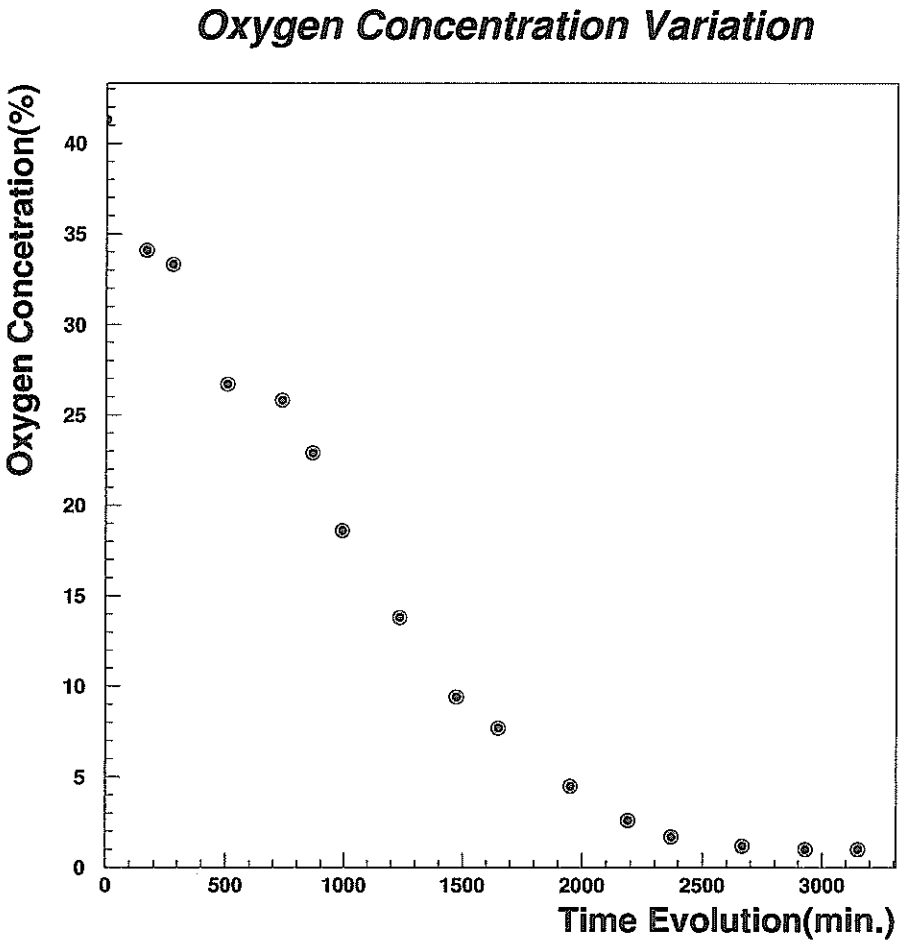

Fig. 6.3: Oxygen concentration variation

See Figure 6.4 to get the idea of the peak variation under the system operation. They are, from top to bottom, the results measured in 168, 990 and 3150 minutes from the beginning of the operation, respectively.

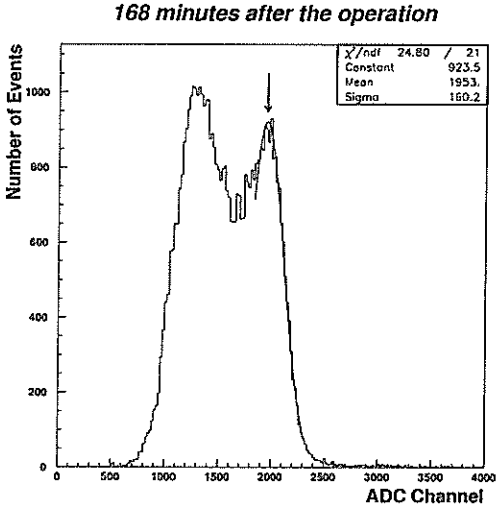

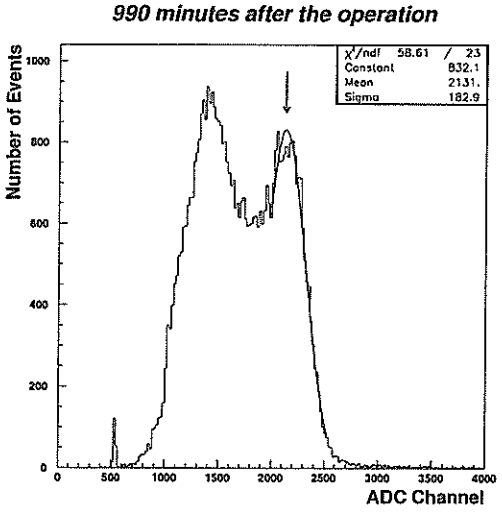

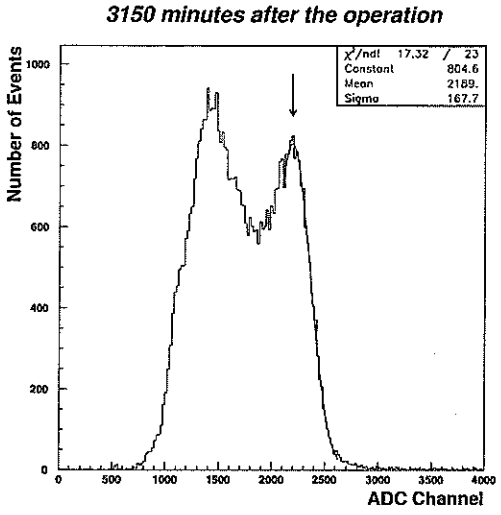

Fig. 6.4: Light output variation for three different measurement time

Figure 6.5 is the the light output variation in terms of the corresponding oxygen concentration (%). Note that the light output here is expressed with the anthracene light output correspondence, assuming that of 51% of the anthracene is realized as the highest light output in this system. The four squared points are of the results obtained in the laboratory test using the $300ml$ beaker system.

6.2 Results

As in Figure 6.5, we can see that the light output is improved with the reduction of the oxygen concentration. It is desired to have the oxygen concentration less than 5% to keep the light output which is worth that of 51% of the anthracene. And the 5% improvement of the light output in terms of the anthracene is obtained for 53-hour operation, which is consistent with the results shown in the previous chapter and obtained in the $300ml$ beaker system.

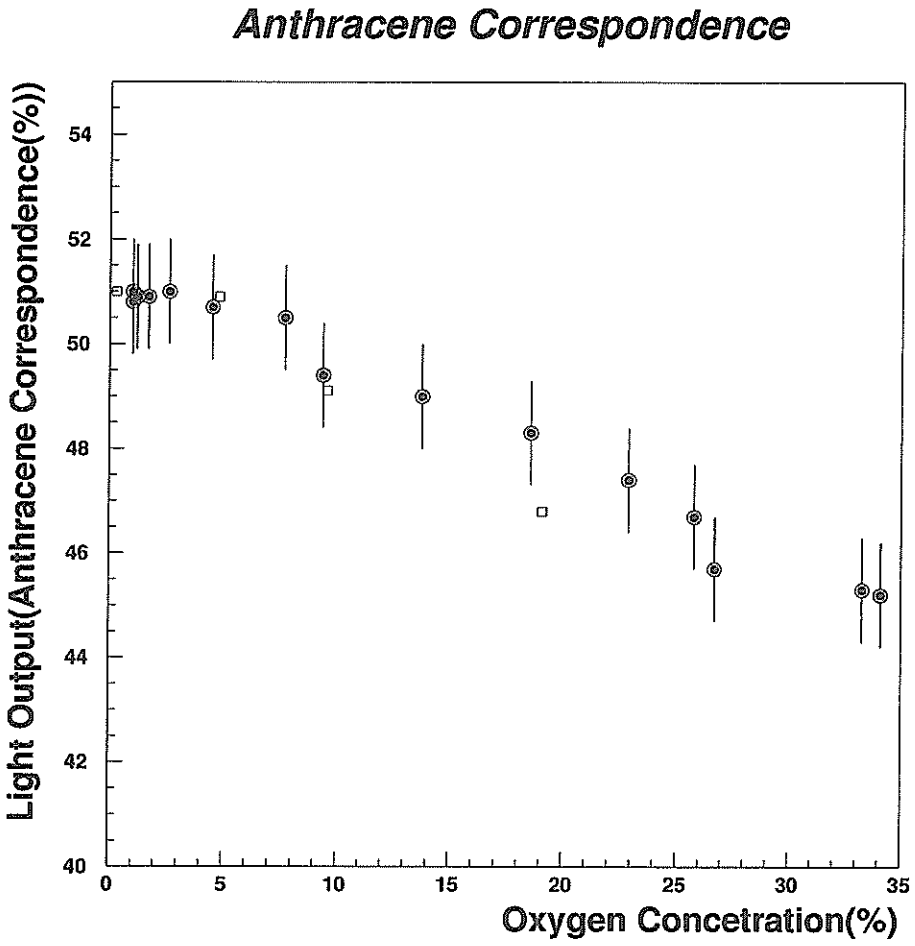

Fig. 6.5: Light output improvement with respect to the oxygen concentration
The four squared points are of the results obtained in the laboratory test using the $300ml$ beaker system.

Chapter 7

Delayed Coincidence Technique

$\bar{\nu}_e$ detection is based on the inverse β-decay with the aid of the delayed coincidence technique in the liquid scintillator, which is crucial for KamLAND experiment. To assure this technique, Am/Be source is well adapted that experiences the similar reactions to the inverse β-decay as in the detection of $\bar{\nu}_e$. This is further discussed in this chapter.

7.1 Principle of the $\bar{\nu}_e$ Detection

Figure 7.1 given below shows the schematic diagram for the $\bar{\nu}_e$ detection in the liquid scintillator. $\bar{\nu}_e$ with an energy larger than 1.8MeV suffers the inverse β-decay with a proton in the scintillator, producing one positron and neutron ($\bar{\nu}_e + \mathrm{p} \rightarrow \mathrm{n} + \mathrm{e}^+$).

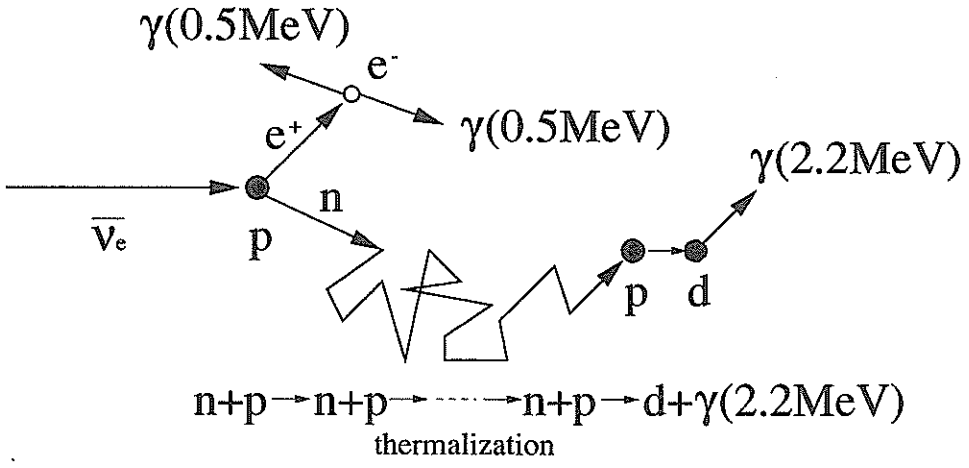

Fig. 7.1: Principle of the $\bar{\nu}_e$ detection through the inverse β-decay in the liquid scintillator

The positron then loses its energy via the ionization and annihilates with an electron in the scintillator, leading to the two gammas generation. This process occurs within a few ns from the $\bar{\nu}_e$ reaction, and the energy deposit due to the e^+ and two gammas form so-called the prompt signal which is larger than 1.0MeV. On the other hand, a neutron scatters with protons elastically until it is thermalized and then captured by a proton, giving a deuteron which results in the 2.2MeV gamma emission. This emission seems to occur approximately 200μs after the $\bar{\nu}_e$ reaction and thus gives a delayed signal compared to the prompt one. We can hence obtain two signals separated about 200μs from each other in one reaction. To identify the arrival of the delayed signal, we open the gate with a few hundred μs width triggered by the prompt signal. Delayed signal detection within the gate is thus a candidate as a $\bar{\nu}_e$ induced event. After all, introducing the energy and spatial cuts, we determine the $\bar{\nu}_e$ events. This method used for the $\bar{\nu}_e$ identification is called the delayed coincidence technique.

7.2 Delayed Coincidence Technique for Am/Be Source Signals

Am/Be is a radioactive source used both as gamma and neutron emitter. The mechanism of their emissions in Am/Be results from α particles by ^{241}Am decay. An α impinges on ^{9}Be, leading chiefly to the production of a $^{12}C^*$ and one neutron.

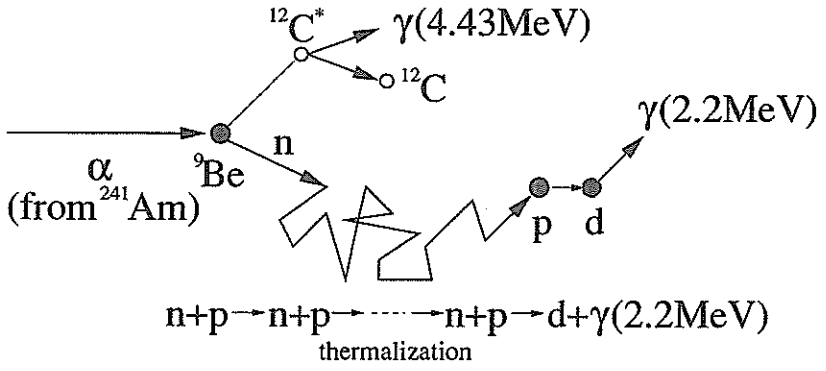

Fig. 7.2: Am/Be source induced reactions in the liquid scintillator

$^{12}C^{*}$ then de-excites with the emission of 4.43MeV gamma, which gives the prompt signal. The neutron, on the other hand, experiences the same reactions discussed in the previous section, such as the elastic scattering with protons until it is thermalized and then captured resulting in the 2.2MeV gamma. This gamma is referred to the delayed signal. The reactions of the gamma and neutron emitted by Am/Be is described in Figure 7.2.

7.3 Experimental Method and Setup

This section gives the practical description of how to introduce the delayed coincidence technique into the detection of two different signals from Am/Be source.

The Am/Be source is placed in the middle of the balloon. And the experimental setup is prepared as in the block diagrams, Figure 7.3. Four 20-inch PMTs were in use for this experiment.

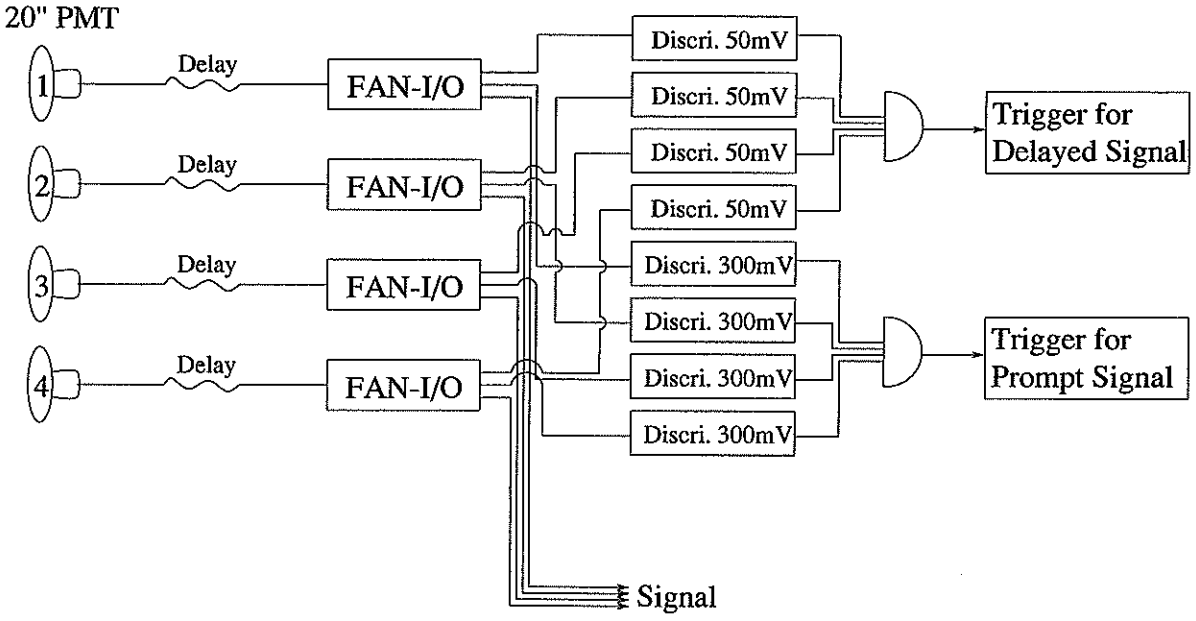

continued on the next page

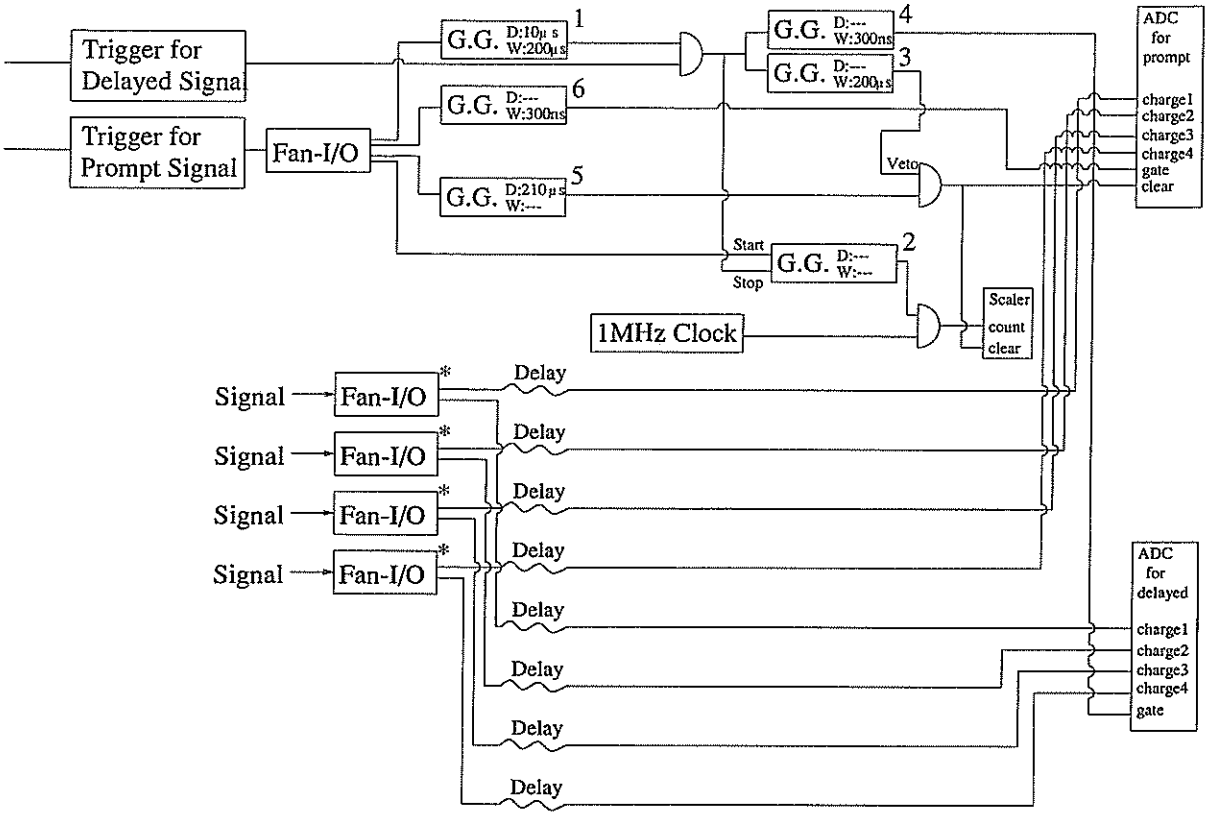

Fig. 7.3: Schematic block diagrams of the experimental setup
G.G. stands for a gate generator, and D and W inside the box representing a gate generator denote the delay and width of the generated gate.

Photons detected in each PMT are summed in the Fan-in - Fan-out denoted with $*$ and provided into both ADCs for prompt and delayed signals. Trigger conditions for both signals are determined by the discriminators. 300mV and 50mV are given as the threshold values for prompt and delayed signals, respectively, which are correspond to approximately 1.8MeV and 0.5MeV for the charge summation to obtain both 4.43 and 2.2MeV gamma peaks clearly. Roles for all gate generators are referred to Figure 7.4 given below. Actually, the 1MHz clock generator is introduced in order to measure the neutron capture time. This can be measured by counting the number of clock pulses coincident with the gate opened between the arrivals of the prompt and delayed signals.

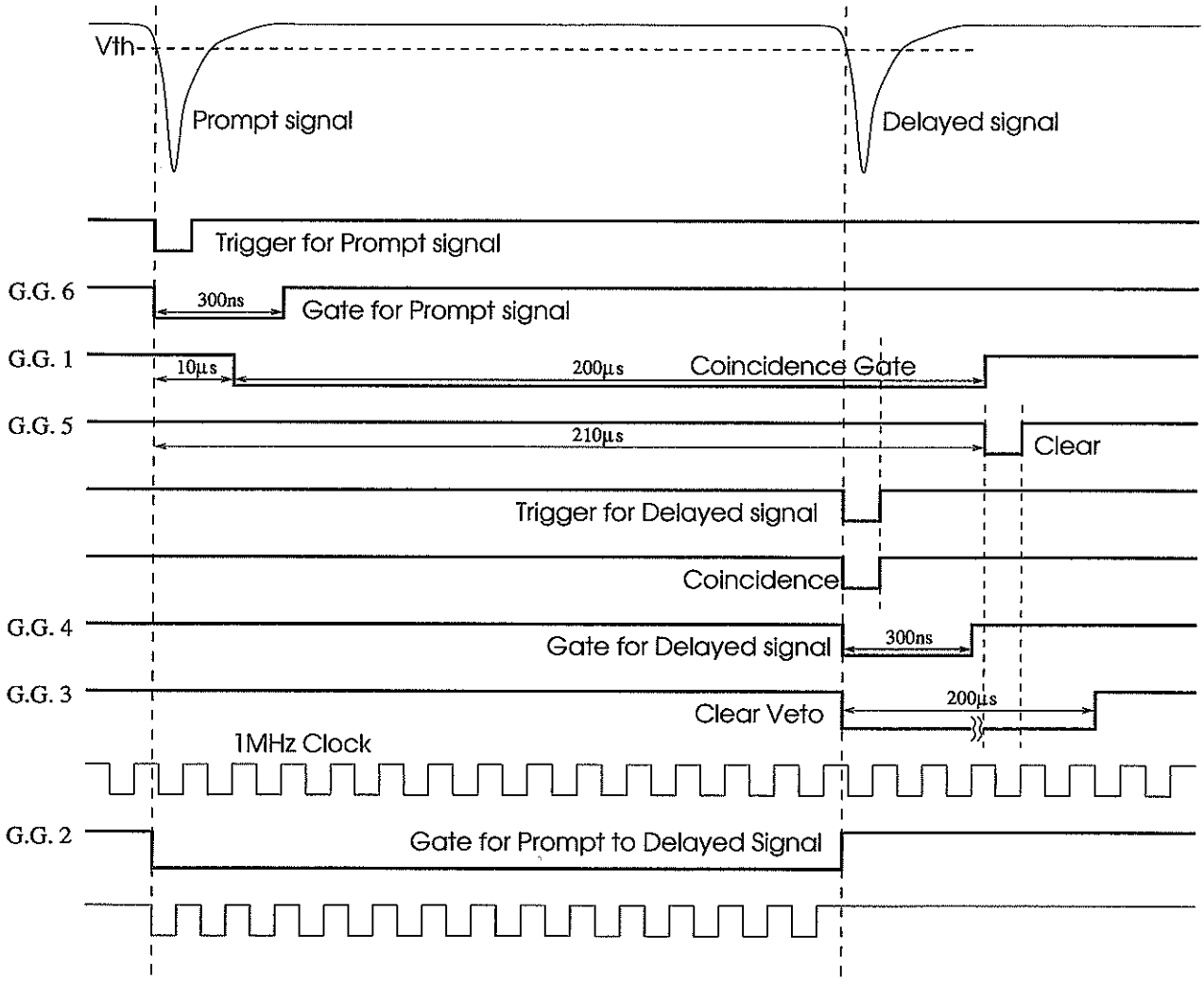

Fig. 7.4: Schematic diagram of the delayed coincidence principle

7.4 Results

With the calibration mentioned in the previous chapter, the energy spectra for both prompt and delayed signals are obtained as in Figure 7.5, while Figure 7.6 is obtained without the Am/Be employment. The top figures are for the prompt signal and the bottom ones for the delayed signal in both figures. Two arrows in the prompt signal energy spectrum indicate the energies which are 4.4 and 5.4MeV. A possible explanation to account for them is the 4.43MeV gamma plus energy promptly deposited by the neutron. On the other hand, the arrow in the delayed signal energy spectrum shows 2.2MeV due to the creation of the deuteron. The black filled area in the prompt signal spectrum is restricted compared to its peak value (5.4MeV). This is because less background events are favoured. Actually, peaks without the arrow indication come from the threshold effects brought about in the discriminators. due to the accidental backgrounds and thus form the fake peaks. The extraction of the black filled area in the prompt signal spectrum results in the detection of the correlated delayed signals with less background events which is shown as the black filled area as well in the delayed signal spectrum.

Figure 7.7 shows the same spectra in terms of the two dimensional contour plots. We can see the correlation of the prompt and delayed signals. And the presence of the fake peaks are verified through the experiment without any radioactive sources employed in the detector.

The lower figures point out the neutron capture time. Obviously, the capture time is unable to be found without the Am/Be source employment.

Therefore, we see that the neutron capture time is obtained $173 \pm 2\mu$s ($1022 \pm 16\mu$s without Am/Be, instead), and it is possible to use the delayed coincidence technique for the detection of two different signals separated a few hundred μs with each other. This assures to find the $\bar{\nu}_e$ with this technique in KamLAND.

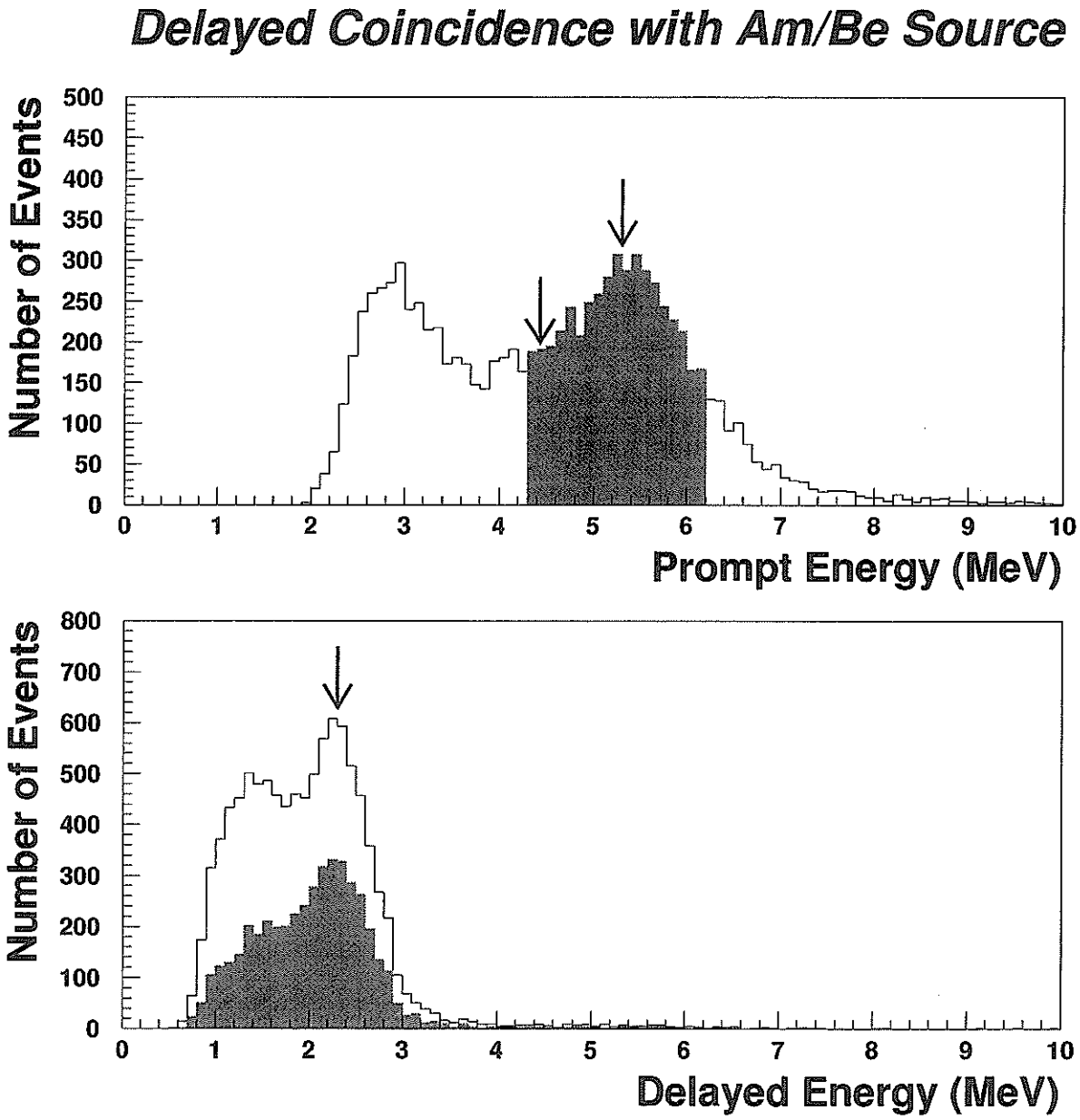

Fig. 7.5: Energy spectrum for prompt and delayed signals with Am/Be

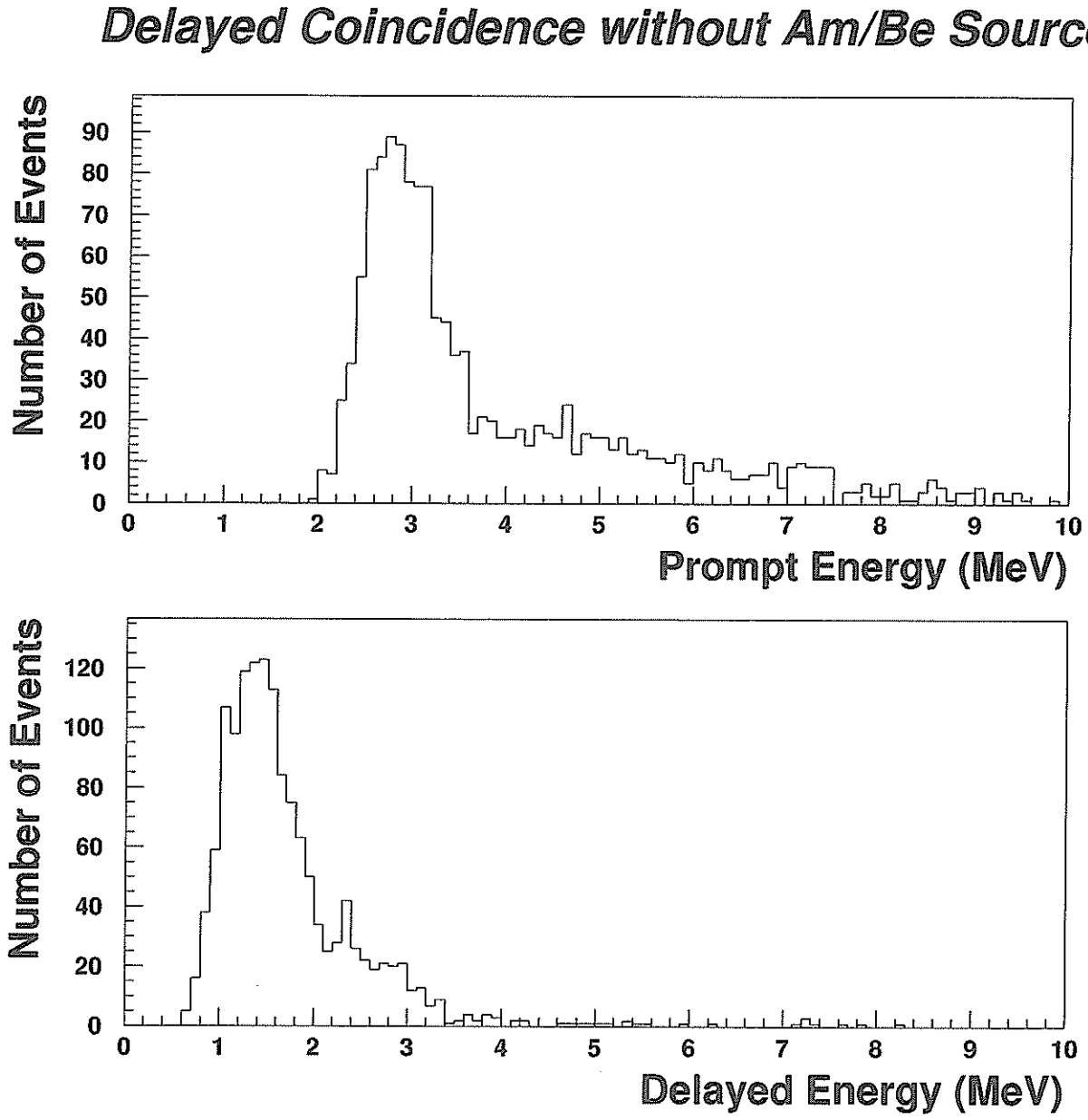

Fig. 7.6: Energy spectrum for prompt and delayed signals without Am/Be

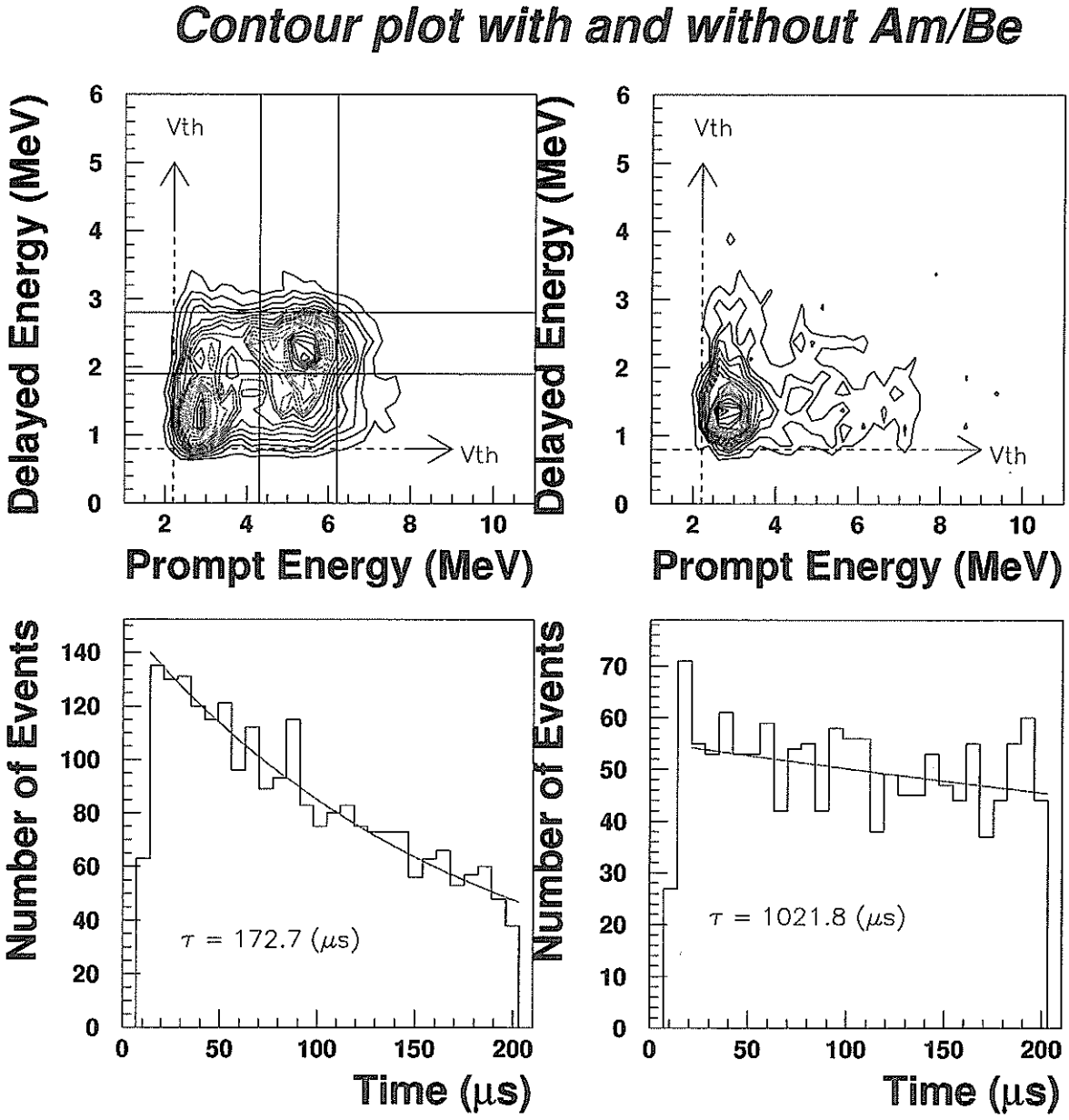

Fig. 7.7: Prompt and delayed signal correlations and neutron capture time Leftside figures are measured with Am/Be, and rightside ones are without Am/Be. Of course, no specific contributions by the neutron can be seen in the capture measurement without the Am/Be.

Chapter 8

n/γ Discrimination

The differentiation between neutron and gamma with the Pulse Shape Discrimination method(PSD) is crucial in KamLAND experiment to reject background events which bring about the reactions similar to the real $\bar{\nu}_e$ induced events. In the laboratory test with the $300ml$ beaker system the liquid scintillator shows the good pulse shape discrimination of 6.5% neutron contamination preserving the 90% gamma efficiency. Usually, it seems that the PSD would be worsen for larger detector systems so that it is important to evaluate whether PSD is available for 1.5m^3 system. This is discussed in this chapter.

8.1 Principle of PSD

The fast component of the scintillation light comes from the de-excitation of molecules of the solute in the lower singlet excited state (fluorescence process), while the tail, referred as delayed or slow component, is an effect of the so-called delayed fluorescence mechanism, originated by the triplet annihilation reaction involving two excited molecules in the lower triplet excited state. This is further explained in Appendix A. The strong dependence of the amount of the delayed component on the specific energy loss of the exciting particle provides a powerful tool to distinguish among different species of incident radiations impinging upon an organic scintillator. Actually, this effect is the basis for the pulse shape discrimination method, widely applied in neutron detection applications with liquid scintillators, where the heavily ionizing recoil protons are discriminated by the gamma through the long tail characterizing their scintillation light. Figure 8.1 is the example of the different decay

times for the α and electron which experience the different ionization loss in the liquid scintillator.

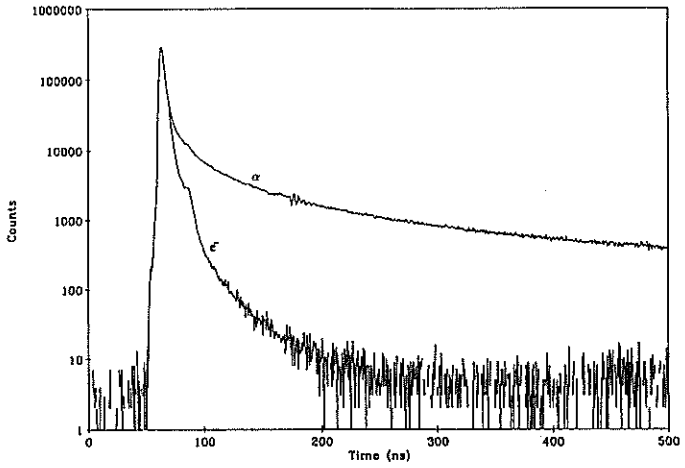

Fig. 8.1: Example of the decay time difference of the α and electron

The difference between $\bar{\nu}_e$ induced and fast neutron induced reactions is in terms of the prompt signals. Refer to Figure 8.2 for the mechanism of the fast neutron induced reactions. As mentioned in Chapter 2, fast neutrons are produced in the rocks surrounding the KamLAND detector, via the interaction with the cosmic ray muon. They can be serious backgrounds in case they reach the liquid scintillator tank. They will be suppressed with the introduction of the PSD.

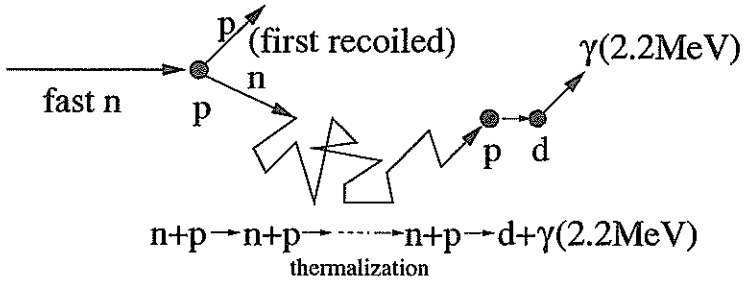

Fig. 8.2: Mechanism of the fast neutron induced reactions

8.2 PSD with the 300ml Beaker System

As mentioned, the liquid scintillator used in the Test Bench Facility shows the good pulse shape discrimination of 6.5% neutron contamination preserving the 90% gamma efficiency in the laboratory test using the 300ml beaker system. Figure 8.3 is the separation between neutrons and gammas obtained in this system. In this study, ^{252}Cf source is used as the neutron emitter. Actually, this also emits gammas in its spontaneous fission. The ratio is given by that of the tail charge of the pulse to the total one which is further explained later.

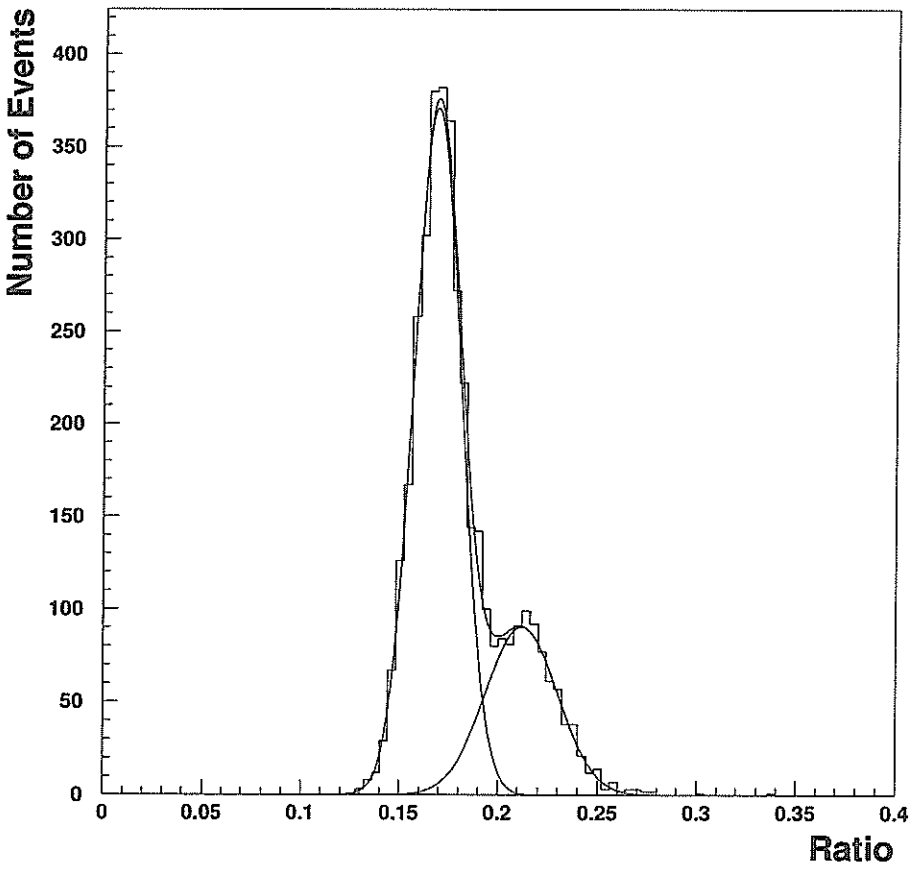

Fig. 8.3: n/γ discrimination in the 300ml beaker system

8.3 Pulse Shape Differences between Light and Heavy Particles

The n/γ discrimination is based on the observation of the tail charge difference for different incident particles so that the tail charges for all the detected signals are integrated as well as the total charges for them. Actually, the prompt charges are taken instead of the tail ones in this experiment. Figure 8.4 indicates how to define the prompt charge as well as both total and tail charges.

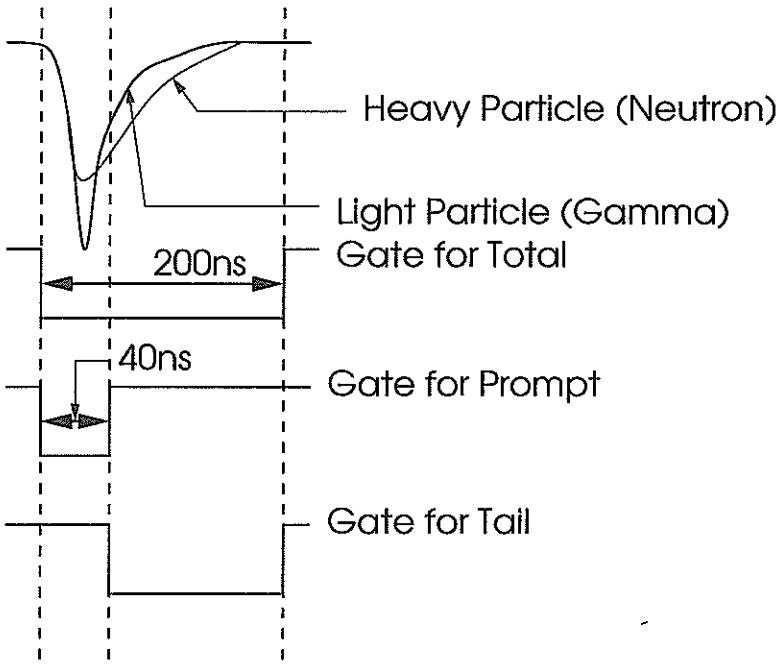

Fig. 8.4: Total, prompt and tail charge definition

Here, 200ns and 40ns are applied for the total and prompt gates. The gate width for the NaI signal integration is set to 1μs.

8.4 Experimental Method and Setup

To obtain neutron events cleanly, Am/Be source, 7.6cmϕ $\times$ 7.6cm NaI and 1.5-inch PMT are prepared. Am/Be is attached to the NaI which is mounted to the 1.5-inch PMT as

shown in Figure 8.5. All of them are put inside the EVOH bag to prevent the liquid scintillator from damaging them. Am/Be provides one neutron for each 4.43MeV gamma production so that this may enable us to collect clean neutrons in the liquid scintillator by taking the coincidence of this gamma fired the 1.5-inch PMT.

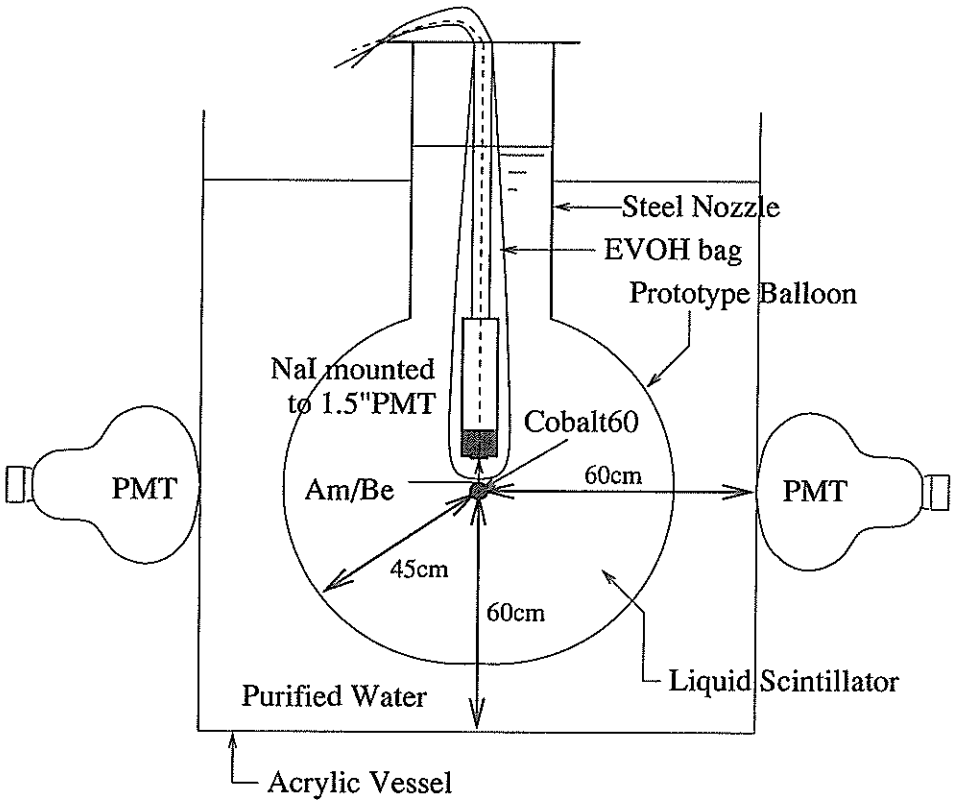

Fig. 8.5: Arrangement of Am/Be source with NaI mounted to 1.5-inch PMT
Actually, ^{60}Co is also employed at the center of the liquid scintillator separately.

The decay time of pulses in NaI extends $\sim 1\mu$s. Still, better resolution is assured than that of the liquid scintillator[26], so that this will provide the total absorption peak, single escape peak, double escape peak and the Compton continuous spectrum of the 4.43MeV γ-ray as will be seen later in Figure 8.7. The ^{60}Co source is also employed to obtain the pure gamma events which differentiate the ones relevant to the 4.43MeV gamma. This is hung down with the same manner explained in Chapter 4.

The electronics setup is described in Figure 8.6. The trigger is the coincidence of

the four 17-inch PMTs coincidenced signal and the NaI detected signal. After the event detection is performed, off-line analysis is introduced to identify neutrons triggered by the Am/Be 4.43MeV gamma or gammas from ^{60}Co.

Here, all PMTs are calibrated beforehand with the same manner and used the same electronics as in Chapter 4. Nitrogen gas bubbling is performed as well.

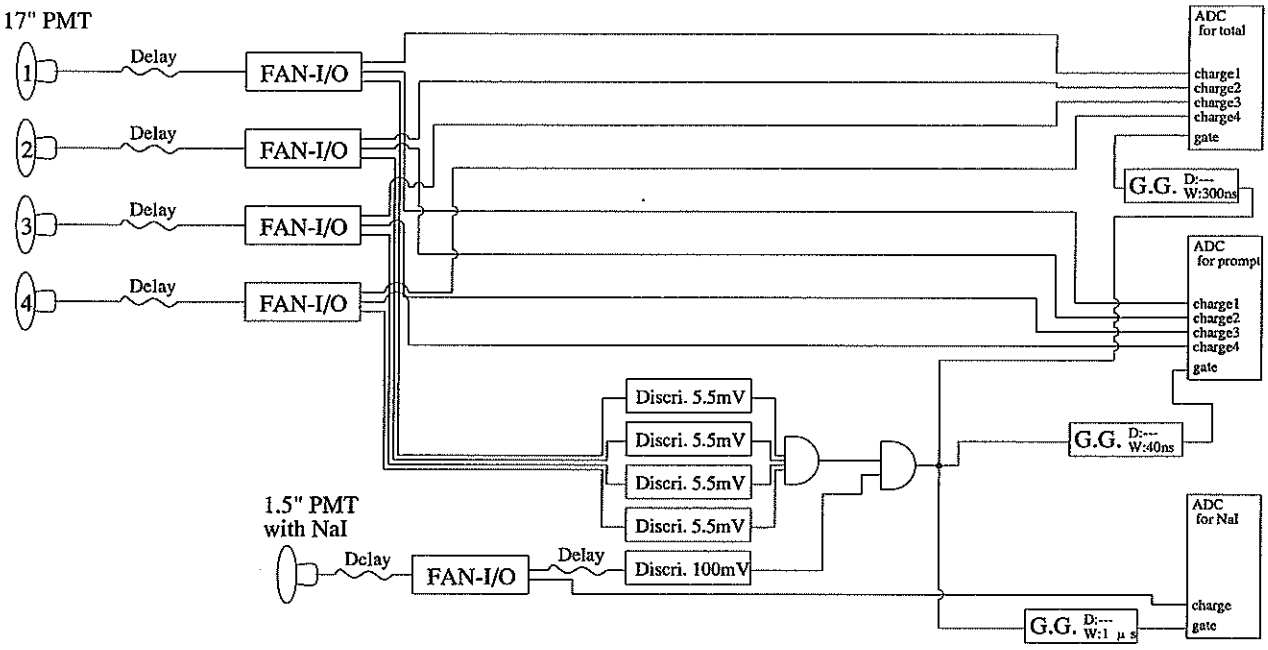

Fig. 8.6: Schematic block diagram for n/γ discrimination experiment

8.5 Results

Figure 8.7 is the spectrum obtained in NaI. Three peaks in high energy region are the double escape peak, single escape peak and total absorption peak of the 4.43MeV gamma emitted from Am/Be from left to right. On the other hand, two peaks in the low energy region are 1.173 and 1.333MeV gammas from ^{60}Co. Figure 8.8 is the spectrum obtained by the off-line charge summation of the four 17-inch PMTs. Also, Am/Be 4.43MeV gamma triggered events and ^{60}Co triggered events are shown in the same figure. Figure 8.9 is the prompt to total charge ratio for both neutron(left) and gamma(right) related events.

Actually, to separate them cleanly, the spatial cut is introduced as well as the energy cut of more than 1MeV, in which the region is the proximity of the center of the balloon by assuming the charge subtraction of opposite PMTs with respect to the charge summation of them to be approximately zero.

Therefore, we can see the n/γ discrimination in the 1.5m^3 system. Actually, the position dependence of the light transmission and the trigger condition of all the PMTs' coincidence result in the timing jitter so that some of the prompt charges may not be integrated exactly. Moreover, the neutron related events are selected by even including the single and double escape peaks of 4.43MeV gamma from Am/Be. This would a little bit worsen the n/γ discrimination. However, the KamLAND experiment can save both pulse shape and timing information for each event in every PMT, thus we will be able to have better differentiation between neutrons and gammas. Even in the Test Bench Facility can be seen the differentiation if those problems mentioned are solved, for example, by introducing TDCs or FADCs.

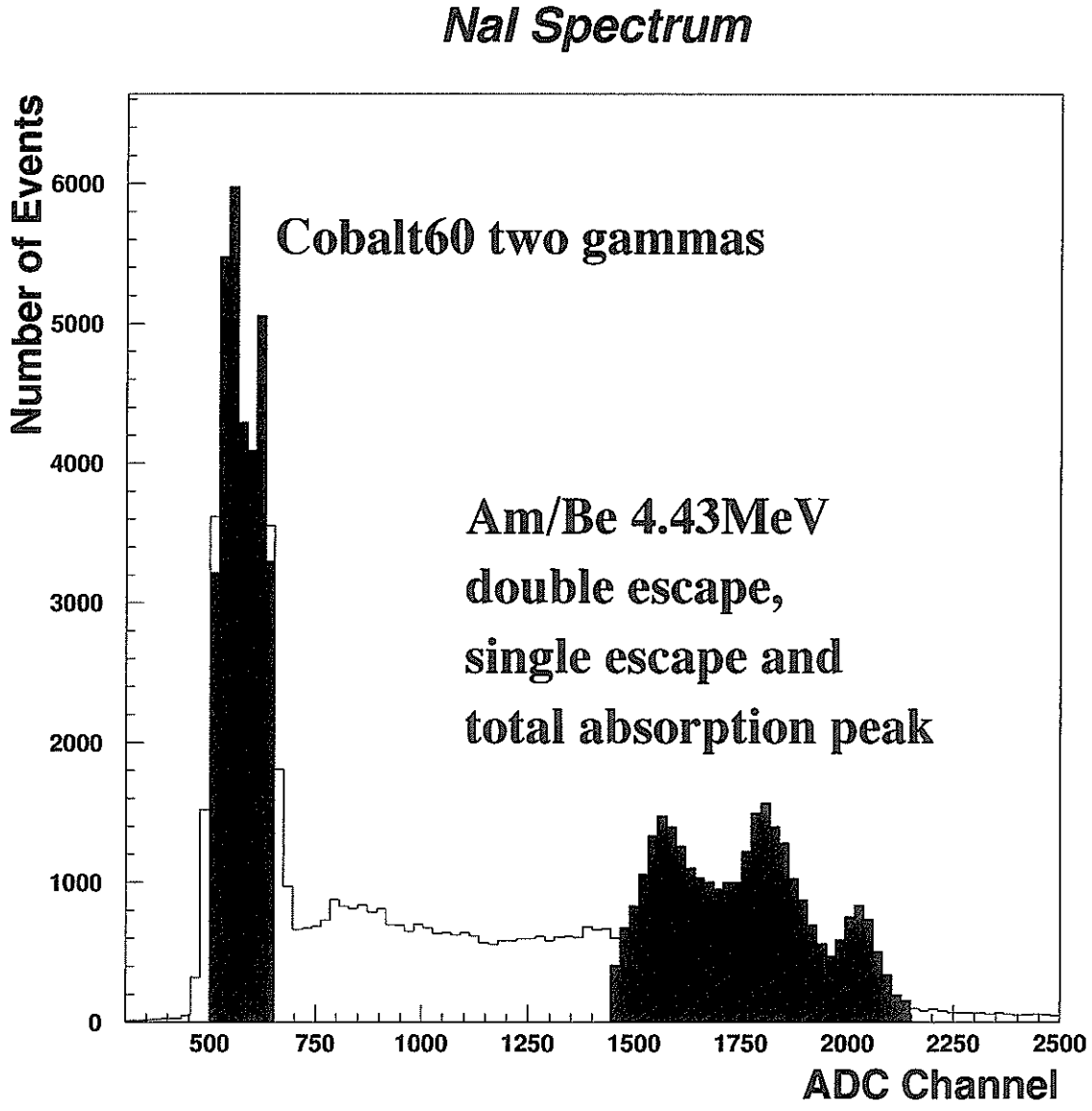

Fig. 8.7: Energy spectrum obtained in NaI

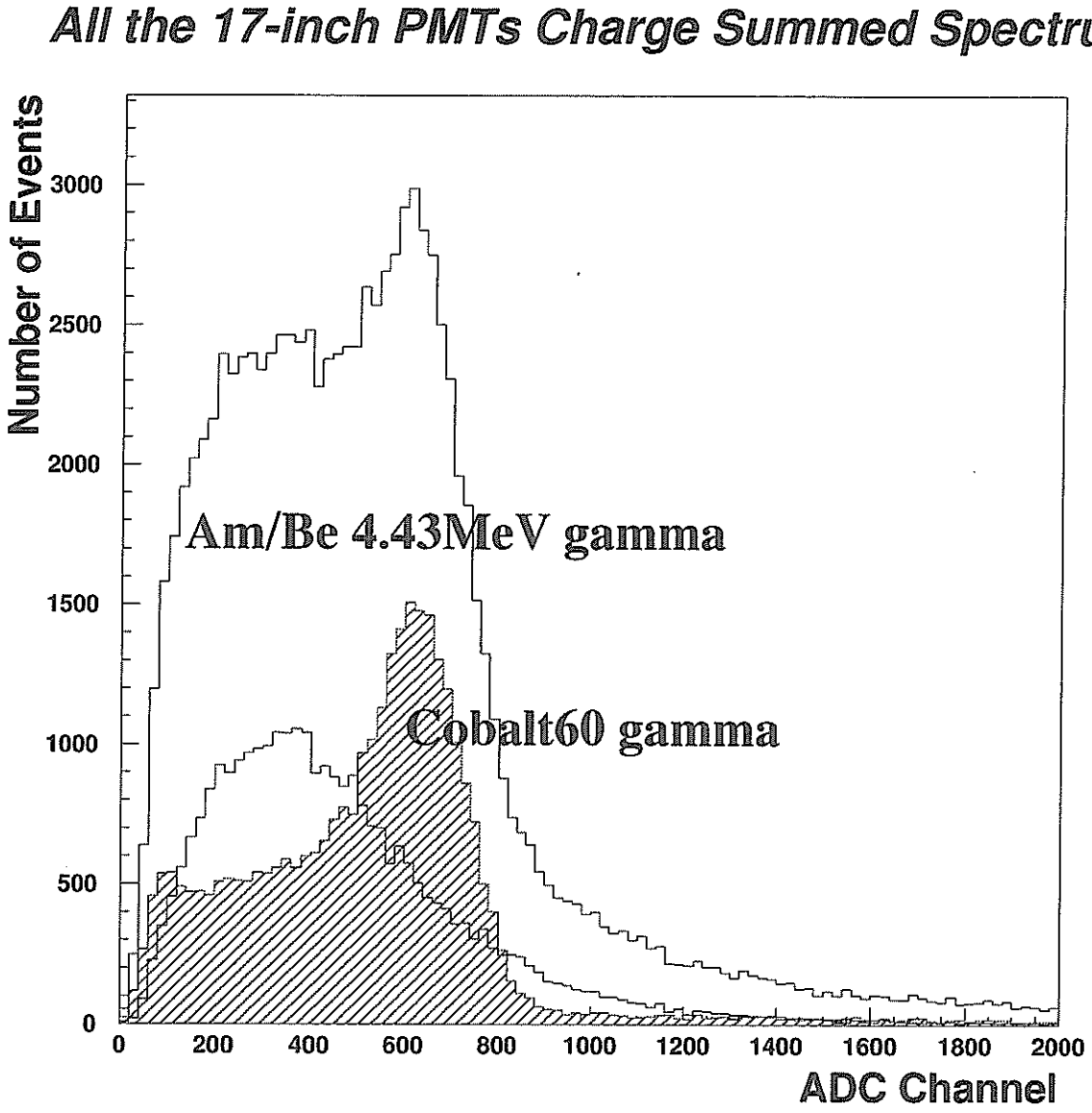

Fig. 8.8: Energy spectrum obtained in the four 17-inch PMTs

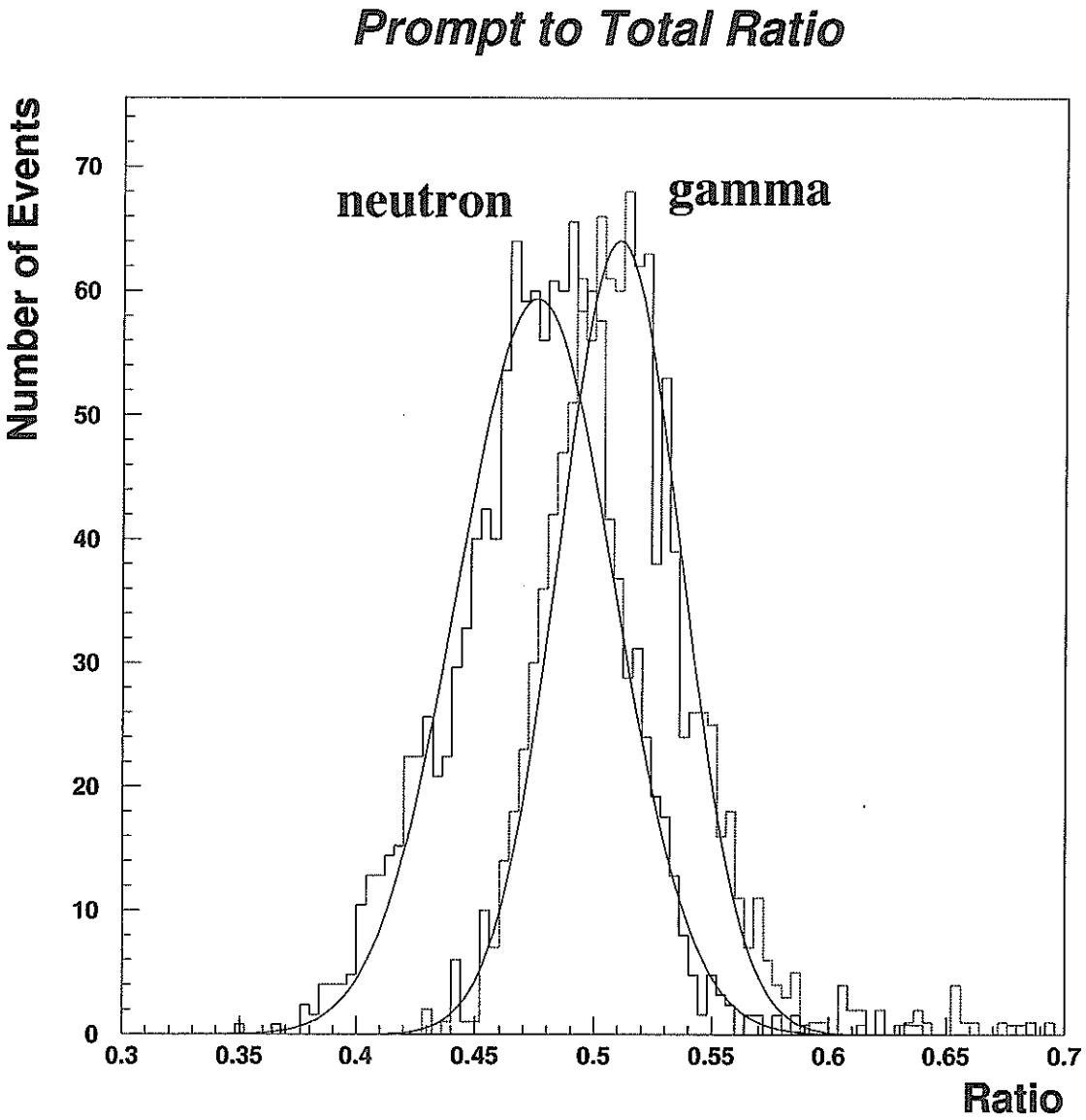

Fig. 8.9: Prompt to total ratio

The spatial cut is introduced as well as the energy cut of more than 1MeV, in which the region is the proximity of the center of the balloon by assuming the charge subtraction of opposite PMTs with respect to the charge summation of them to be approximately zero.

Chapter 9

Conclusion

From the experiments discussed, we obtained the calibration line which is highly applied to the energy identification in terms of the energy for the delayed coincidence experiment, for instance. Also, we could obtain the important results from the study of the liquid scintillator, such as the energy resolution ($\sigma(\mathrm{E})/\mathrm{E} = 3.3 + 18.1(\%)/\sqrt{\mathrm{E(MeV)}}$) and the attenuation length (28.8cm), and the light output improvement by the nitrogen gas bubbling as well as the operation of the Test Purified System. In addition, this 1.5m^3 system provides the measurement of the neutron capture time in the liquid scintillator given by 173 $\pm$ 2μs. And the balloon durability is also confirmed for one year experiment.

Although, the position dependence of the light transmission and the trigger condition of all the PMTs' coincidence result in the timing jitter, the overall experiments in the Test Bench Facility show the ability to perform experiments in KamLAND. The delayed coincidence technique is shown definitely useful for KamLAND, and n/γ discrimination is as well. Actually, the KamLAND experiment can save both pulse shape and timing information for each event in every PMT, thus we will be able to have better differentiation between neutrons and gammas. Even in the Test Bench Facility can be seen the differentiation if those problems mentioned are solved, for example, by introducing TDCs or FADCs.

In the next stage of the experiment, it is essential to create the simulation for further confirmation of the obtained results here, and also introduce 8-inch PMTs for the spatial cut of events. High energy background estimation with respect to the cosmic ray muon spallation is also interesting topic before the KamLAND project launches.

Appendix A

Scintillation Mechanism

In this chapter, the mechanism of the light emission of liquid scintillator is explained. Liquid scintillator is composed chiefly of solvents and solutes (fluorescent molecules). In general, the solvent has roles to absorb the energy of incident radiation (mainly by its ionization) which successively excite themselves, and to transmit the energy to the solute quickly and effectively via the de-excitation. The solute has to emit fluorescence whose wavelength is sensitive to other detectors such as photomultipliers so that we can identify and analyze the incident radiation. The detailed explanation of the energy transfer among the compounds of the liquid scintillator is given in the following sections.

A.1 General Characteristics

The scintillator signal, in general, provides a variety of information. Especially, the sensitivity to energy, fast time response and pulse shape discrimination are the outstanding features.

As radiation passes through the scintillator, it excites the atoms and molecules of the scintillator, which results in the light emission. This light is transmitted to the photomultiplier in which it is converted into a weak current of photoelectrons. This is then amplified by an electron multiplier system so that we can analyze the signal by the electronics system.

Generally, the re-emission process can be described with two-component exponential[27]

$$N = A\exp(\frac{-t}{\tau_f}) + B\exp(\frac{-t}{\tau_s}), \tag{A.1}$$

where N is the number of photons emitted at time t, and τ_s and τ_f are the decay constants. For most scintillators, one component is generally much faster than the other so that we refer to them as the fast and slow components. Their relative magnitudes, A and B depend on materials. Figure A.1 shows the relation between these components.

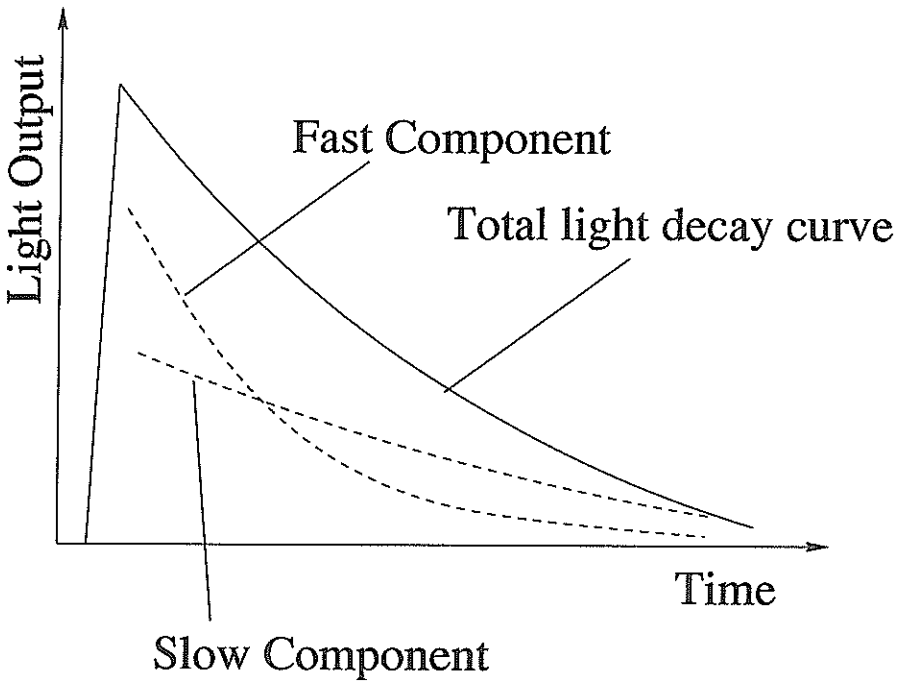

Fig. A.1: Two components of the scintillation light with the total light decay curve

While many scintillators exist, a good detector scintillator should satisfy:

- high efficiency for conversion of exciting energy to fluorescent radiation
- transparency to its fluorescent radiation for better transmission of the light
- absorption spectral band of the solute consistent with the emission spectral band of the solvent
- emission spectral band of the solute consistent with the spectral response of existing photomultipliers
- a short decay constant τ.

A.2 Excitation of Solvent

Incident radiation upon the liquid scintillator is first absorbed by the solvent. There are few chances for the radiation to be absorbed by the solute first instead, due to its few concentration compared to the solvent in the liquid scintillator. The energy of the radiation is usually much higher than the excitation energy of the solute (a few eV) so that the radiative excitation may result in the σ electron excitation, π electron excitation, ionization or dissociation as follows.

$$^1\mathrm{M} + \mathrm{W} \rightarrow {}^1\mathrm{M}^* \tag{A.2}$$

$$^1\mathrm{M} + \mathrm{W} \rightarrow {}^3\mathrm{M}^* \tag{A.3}$$

$$^1\mathrm{M} + \mathrm{W} \rightarrow \sigma^* \tag{A.4}$$

$$^1\mathrm{M} + \mathrm{W} \rightarrow \mathrm{M}^+ + \mathrm{e}^- \tag{A.5}$$

$$^1\mathrm{M} + \mathrm{W} \rightarrow \mathrm{X}^+ + \mathrm{X}^- \tag{A.6}$$

Here, $^1\mathrm{M}^*$ and $^3\mathrm{M}^*$ are the excited singlet and triplet states for π electrons, respectively. (π electrons are de-localized free valence electrons of solvent and are not associated with any particular atom in the molecule so that they can occupy what are known as the π-molecular orbitals). And X and σ^* denote the dissolution of the molecule and the excited state of the σ electrons. Produced electrons in (A.5) may experience the reactions as in (A.1$\sim$4). Moreover, they experience other reactions given below.

$$\mathrm{M}^+ + \mathrm{e}^- \rightarrow {}^1\mathrm{M}^* \tag{A.7}$$

$$\mathrm{M}^+ + \mathrm{e}^- \rightarrow {}^3\mathrm{M}^* \tag{A.8}$$

$$\mathrm{M}^+ + \mathrm{e}^- \rightarrow \sigma^* \tag{A.9}$$

$$^1\mathrm{M} + \mathrm{e}^- \rightarrow \mathrm{M}^- \tag{A.10}$$

$$\mathrm{X}^+ + \mathrm{e}^- \rightarrow \mathrm{X} \tag{A.11}$$

Reactions (A.4), (A.6), (A.9) and (A.11) are not useful for the generation of the scintillation light, and they may provide the energy loss through the heat or radiation damage.

A.3 Energy Transfer between Solvents

This kind of energy transfer is classified into two processes such as the collisional process and the excimer formation.

The collisional process is the one that the excited molecules give their energies to the non-excited ones through the collision between them. This phenomena is expressed given below.

$$M_1{}^* + M_2 \rightarrow M_1 + M_2{}^* \tag{A.12}$$

$$M_2{}^* + M_3 \rightarrow M_2 + M_3{}^* \tag{A.13}$$

$$\vdots$$

Each electron orbit of all the relevant molecules for collisions are slightly overlapped so that the electron can be exchanged leading to the energy transfer. This transfer depends on the solvents' temperature and viscousness. Thus, high temperature and low viscousness solvent prompt it.

On the other hand, the excimer formation is explained by the mechanism of the energy transfer through the excimer. The excimer is the excited dimer, which is stable only in the excited state. It is composed of the same two molecules, one is in the ground state and the other is in the excited state. The excimer formation and dissolution frequently occur, which thus results in the fast energy transfer compared to the fluorescence emission.

$$M_1{}^* + M_2 \rightarrow (M_1 \cdot M_2)^* \rightarrow M_1 + M_2{}^* \tag{A.14}$$

$$M_2{}^* + M_3 \rightarrow (M_2 \cdot M_3)^* \rightarrow M_2 + M_3{}^* \tag{A.15}$$

$$\vdots$$

The energy transfers in these processes are performed within 10^{-9}s and most solvent molecules are relevant to either one of the processes.

A.4 Energy Transfer between Solvent and Solute

The excited energy of solvent is ultimately transferred to the solute. Here, two processes are expected, which are from the lowest excited state or from the higher excited state above it as in the following reactions in order,

$$^1\mathrm{M}^* + {}^1\mathrm{F} \rightarrow {}^1\mathrm{M} + {}^1\mathrm{F}^*, \tag{A.16}$$

$$^1\mathrm{M}^{**} + {}^1\mathrm{F} \rightarrow {}^1\mathrm{M} + {}^1\mathrm{F}^{**}, \tag{A.17}$$

where M and F denote the solvent molecules and the solute ones. $^1\mathrm{M}^{**}$ in (A.17) has a quite shorter lifetime ($\sim 10^{-15}$s) than that of $^1\mathrm{M}^*$ ($\sim 10^{-9}$s). Therefore, $^1\mathrm{M}^{**}$ may transfer to $^1\mathrm{M}^*$ or experience a transition to the ground state non-radiatively before interacting with the solute molecules in case the solute is low concentrated compared to the solvent. In other words, the probability of these two processes depend upon the concentration of the solute[28], namely,

$\mathrm{F} < \sim 10^{-3}\mathrm{M}$: Reaction (A.16) is dominated.

$\mathrm{F} \sim 10^{-2}\mathrm{M}$: Both reactions are found.

$\mathrm{F} > \sim 10^{-1}\mathrm{M}$: Reaction (A.17) is dominated.

To explain the energy transfer between the solvent and the solution, the dipole-dipole interaction and the collisional process between them by the formation of the intermediate solvent are considered. Actually, the latter process is similar to the excimer formation discussed before. These two processes are non-radiative energy transfer. The radiative energy transfer can be also considered as well.

The dipole-dipole interaction occurs between the electric dipole of excited molecule and non-excited one, and the energy is transferred non-radiatively in the long range. The distance between two molecules is so long that we can neglect the effect of more than quadrupole-quadrupole interactions, and thus realize the dipole-dipole interaction dominates.

The radiative energy transfer is the phenomenon that the excited solvent molecule emits its energy as fluorescence which is successively absorbed and then prompted to emit

the fluorescence by the non-excited solute molecule. This phenomenon can be expressed in the following reactions,

$$M^* \rightarrow M + h\nu_M, \tag{A.18}$$

$$F + h\nu_M \rightarrow F^*, \tag{A.19}$$

$$F^* \rightarrow F + h\nu_F, \tag{A.20}$$

where M and F denote the solvent and the solute, respectively, and $h\nu_M$ and $h\nu_F$ are photon energies for the solvent and the solute.

Actually, the solvent for liquid scintillator may emit fluorescence but the fluorescence quantum yield (= number of molecules emitting fluorescence/number of excited molecules) for this solvent is much smaller than that of the solute. This energy transfer depends on the concentration of the solute as well as the relationship between the emission band of the solvent and the absorption band of the solute, and in fact, it dominates in case the ultra-low concentration of the solute is realized. Usually, we choose the standard concentration of $\sim 10^{-2}$M in which the non-radiative energy transfer dominates.

A.5 Energy Transfer between Solutes

The energy transfer between different solutes may occur under their presence. The solute received the energy is often treated as the waveshifter. The transfer between them is similar to the one mentioned in the previous section. Actually, the ratio of the waveshifter to the whole solute is $\frac{1}{11}$ so that we can realize few chances of the energy transfer from the solvent directly to the waveshifter.

The energy transfer between these solutes is of either the radiative or non-radiative energy transfer. The former one results in the waveshifter's absorption of the fluorescence from the solute, which prompts the re-emission phenomenon by the waveshifter. The latter one is due to the dipole-dipole interaction which depends on the concentration of the waveshifter. Both transfers are in competition.

A.6 Light Emission from Solute

Absorbed the excited energy of the solvent, the solute is excited to either electronic excited level or its vibrational level. Then, the excited solute molecules emit lights by one of the the following four competing processes. Also refer to Figure A.2 given below,

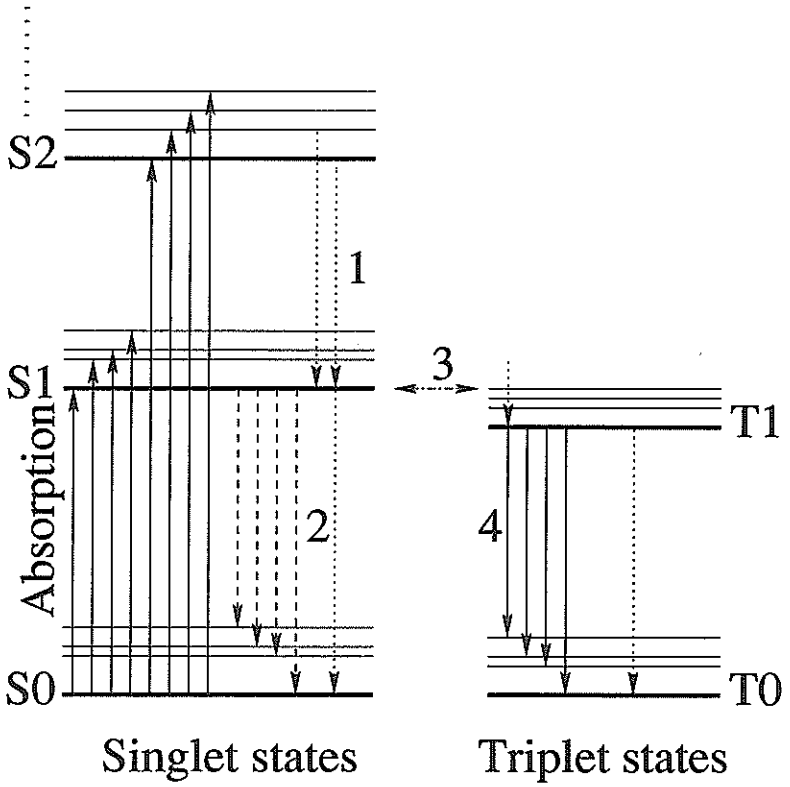

Fig. A.2: Energy level and transition for solute molecule

where S and T are singlet and triplet states, respectively. And 0 denotes a ground state. In the same manner, 1, 2$\cdots$ are excited states from lower levels. Bold lines are of electronic levels and others are of vibrational levels.

1. Internal degradation

   This process is the non-radiative transition whose lifetime is about $10^{-11} \sim 10^{-12}$s.

2. Fluorescence emission

The fluorescence is as a result of the radiative transition just between singlet states, especially the transition from the first excited electronic level (S1) to the ground state (S0). This lifetime is $10^{-8} \sim 10^{-9}$s. Thus, solutes should be satisfied with the high fluorescence quantum yield and low probability of the non-radiative transition from S1 to S0.

3. Intersystem crossing

   Non-radiative transition between a single state and a triplet state. This accompanies the spin flip so that this process may hardly occur due to the multi-pole selection rules of the quantum mechanics. However, the intersystem crossing is possible in case the low energy between these two states is realized.

4. Phosphorescence emission

   This emission from T1 to G is also forbidden due to the same reason above so that this may occur with low probabilities. The phosphorescence lifetime is more than 10^{-4}s, which results from the stability of the T1 level.

The process 2 is the most important and we use the emitted fluorescence in this process as a signal. This decays within a few ns and contributes the fast component of the scintillator light. On the other hand, the excited triplet state molecules decay mainly by interacting with other excited triplet state ones,

$$^3\mathrm{M}^* + {}^3\mathrm{M}^* \rightarrow {}^1\mathrm{M}^* + {}^1\mathrm{M} \tag{A.21}$$

to leave one of the molecules in the S1 state. Radiation is then emitted by the S1 as described above. This light comes after a delay time characteristic of the interaction between the excited molecules and is the slow component of the scintillator light. This characteristic provides the pulse shape discrimination method.

Appendix B

Decay Chains for ^{238}U and ^{232}Th

In nature, there are four series originated from ^{238}U, ^{232}Th, ^{237}Np and ^{235}U. Here, only two series of the first two elements are introduced with their A(mass number) - Z(atomic number) planes and decay chains[29].

B.1 ^{238}U Series

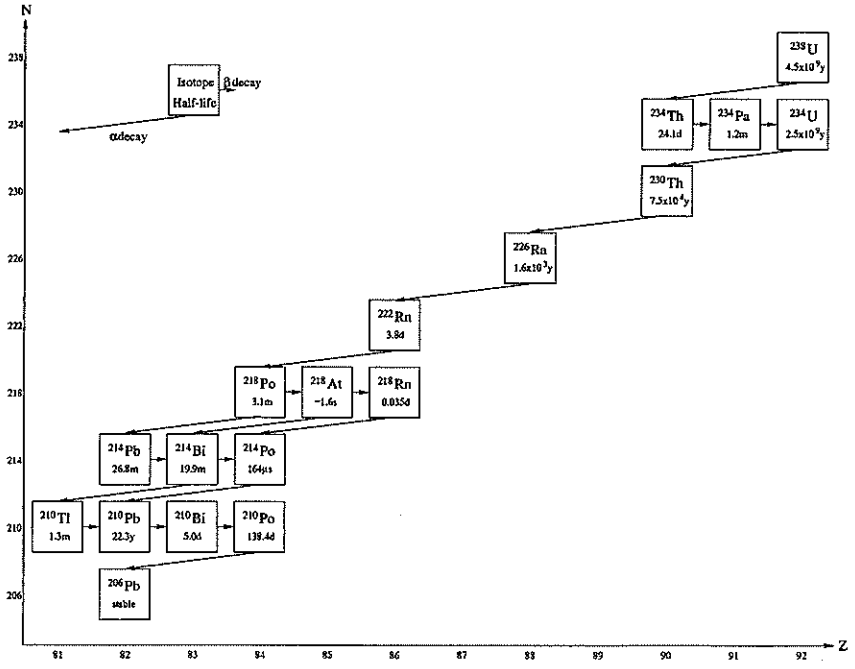

Fig. B.1: A - Z plane for ^{238}U series

^{238}U	E_α(keV)	E_γ(keV)	Branching Ratio(%)
	4198	-	79.0
	4151	50	21.0
↓			
^{234}Th	E_{β^-} Endpoint(keV)	E_γ(keV)	Branching Ratio(%)
	273	-	70.3
	160	113	2.2
	181	92	19.2
	136	137	8.3*
↓			
^{234}Pa	E_{β^-} Endpoint(keV)	E_γ(keV)	Branching Ratio(%)
	2197	-	98.2
	1153	1001, 43	0.9
	1099	1098	0.9*
↓			
^{234}U	E_α(keV)	E_γ(keV)	Branching Ratio(%)
	4775	-	71.4
	4722	53	28.6
↓			
^{230}Th	E_α(keV)	E_γ(keV)	Branching Ratio(%)
	4688	-	76.3
	4621	68	23.7
↓			
^{226}Ra	E_α(keV)	E_γ(keV)	Branching Ratio(%)
	4784	-	94.4
	4602	186	5.6
↓			
^{222}Rn	E_α(keV)	E_γ(keV)	Branching Ratio(%)
	5490	-	100.0
↓			
^{218}Po	E_α(keV)	E_γ(keV)	Branching Ratio(%)
	6002	-	100.0
↓			
^{214}Pb	E_{β^-} Endpoint(keV)	E_γ(keV)	Branching Ratio(%)
	1023	-	9.3
	184	839	0.6
	234	786, 53	0.9
	671	352	46.0
	728	295	28.8
	728	242, 53	11.7
	511	512	2.7*

↓			
^{214}Bi	E_{β^-} Endpoint(keV)	E_γ(keV)	Branching Ratio(%)
	3272	-	19.9
	790	1208, 665, 609	0.5
	824	2448	1.5
	824	1838, 609	0.4
	1068	2204	4.8
	1153	1509, 609	2.2
	1153	2119	1.2
	1255	1408, 609	2.9
	1261	1402, 609	1.5
	1278	1385, 609	0.9
	1382	1281, 609	1.5
	1425	1847	2.1
	1425	1238, 609	5.9
	1508	1764	14.9
	1508	1155, 609	1.6
	1542	1120, 609	14.4
	1542	1730	2.8
	1729	934, 609	2.7
	1857	806, 609	0.9
	1894	1378	3.2
	1894	768, 609	4.0
	1636	1636	10.2*
↓			
^{214}Po	E_α(keV)	E_γ(keV)	Branching Ratio(%)
	6902	800	0.01
	7687	-	99.99
↓			
^{210}Pb	E_{β^-} Endpoint(keV)	E_γ(keV)	Branching Ratio(%)
	64	-	16.0
	17	47	84.0
↓			
^{210}Pb	E_{β^-} Endpoint(keV)	E_γ(keV)	Branching Ratio(%)
	1163	-	100.0
↓			

	E_{β^-} Endpoint(keV)	277, 583, 2615	
^{210}Po	E_α(keV)	E_γ(keV)	Branching Ratio(%)
	5304	-	100.0
↓			
^{206}Pb			

Table B.1: ^{238}U decay chain
Only decay with visible energy larger than 100keV of branching ratio more than 0.5% are listed. Effects of internal conversion are not included as they are negligible for a very large detector (∗: remaining mode lumped).

B.2 ^{232}Th Series

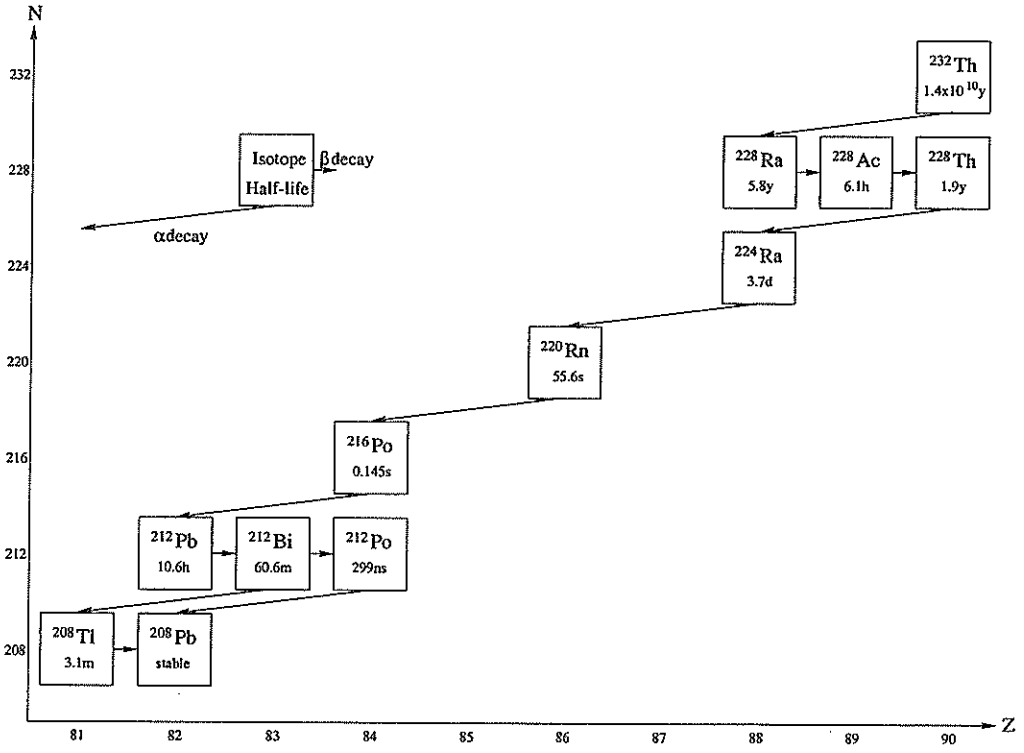

Fig. B.2: A - Z plane for ^{232}Th series

^{232}Th	E_α(keV)	E_γ(keV)	Branching Ratio(%)
	4013	-	77.9
	3954	64	22.1
↓			
^{228}Ra	E_{β^-} Endpoint(keV)	E_γ(keV)	Branching Ratio(%)
	46	-	100.0
↓			
^{228}Ac	E_{β^-} Endpoint(keV)	E_γ(keV)	Branching Ratio(%)
	2069	58	10.0
	403	755, 911, 58	0.7
	438	1631, 58	2.0
	438	1502, 129, 58	0.6
	444	1496, 129, 58	0.9
	481	1588, 58	3.1
	481	1459, 129, 58	0.8
	596	99, 463, 911, 58	1.5
	596	99, 463, 969	1.1
	596	99, 409, 965, 58	0.8
	596	563, 911, 58	1.6
	596	563, 969	0.9
	596	509, 965, 58	1.0
	959	772, 338, 58	1.2
	959	840, 270, 58	0.5
	973	322, 774, 58	0.5
	973	322, 503, 328	0.5
	973	322, 503, 270, 58	0.6
	973	1096, 58	0.9
	973	1154	1.0
	1004	795, 328	2.0
	1004	795, 270, 58	2.3
	1104	965, 58	2.3
	1104	836, 128, 58	0.7
	1158	969	11.6
	1216	911	19.1
	1731	209, 129, 58	3.0
	1731	338, 58	8.6
	1063	1064	20.2*
↓			

^{228}Th	E_α(keV)	E_γ(keV)	Branching Ratio(%)
	5423	-	71.5
	5340	84	28.5
↓			
^{224}Ra	E_α(keV)	E_γ(keV)	Branching Ratio(%)
	5685	-	94.9
	5449	241	5.1
↓			
^{220}Rn	E_α(keV)	E_γ(keV)	Branching Ratio(%)
	6288	-	100.0
↓			
^{216}Po	E_α(keV)	E_γ(keV)	Branching Ratio(%)
	6778	-	100.0
↓			
^{212}Pb	E_{β^-} Endpoint(keV)	E_γ(keV)	Branching Ratio(%)
	574	-	12.3
	274	300	5.2
	335	239	82.5
↓			
^{212}Bi	E_{β^-} Endpoint(keV)	E_γ(keV)	Branching Ratio(%)
64%	2254	-	55.5
	634	1620	1.5
	742	785, 727	1.1
	1527	727	4.4
	1127	1127	1.5*
↓			
^{212}Po	E_α(keV)	E_γ(keV)	Branching Ratio(%)
	8784	-	64.0
↓			
^{208}Pb			

^{212}Bi	E_α(keV)	E_γ(keV)	Branching Ratio(%)
36%	6090	-	9.8
	6050	40	26.2
↓			
^{208}Bi	E_{β^-} Endpoint(keV)	E_γ(keV)	Branching Ratio(%)
	1040	763, 583, 2615	0.8
	1292	511, 583, 2615	8.5
	1525	861, 2615	5.2
	1525	277, 583, 2615	2.6
	1803	583, 2615	17.5
	2500	2501	1.4*
↓			
^{208}Pb			

Table B.2: ^{232}Th decay chain

Only decay with visible energy larger than 100keV of branching ratio more than 0.5% are listed. Effects of internal conversion are not included as they are negligible for a very large detector ($*$: remaining mode lumped).

Appendix C

Nuclear Level Diagrams

Some nuclear level diagrams for isotopes appeared in this thesis are represented, only with decay whose visible energy is larger than 100keV or branching ratio is more than 0.5%. Transitions shown below are just relevant for gamma-ray[30].

C.1 ^{40}K

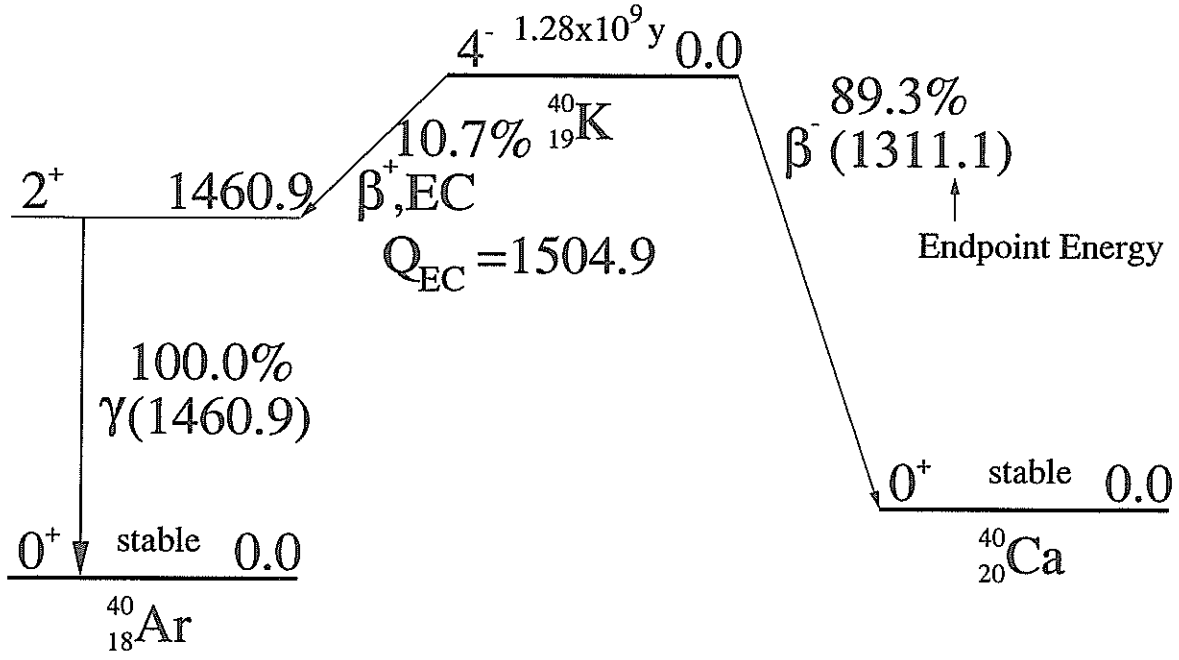

Fig. C.1: Level diagram for ^{40}K

C.2 ^{60}Co

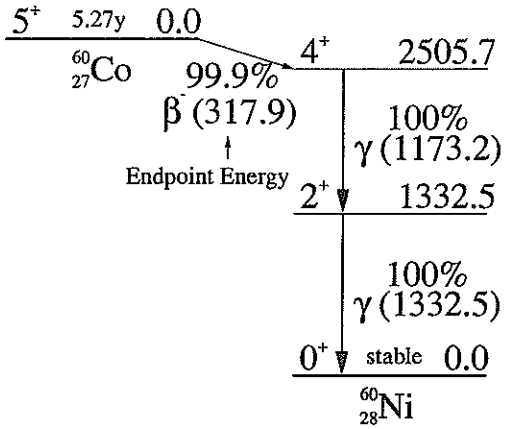

Fig. C.2: Level diagram for ^{60}Co

C.3 ^{137}Cs

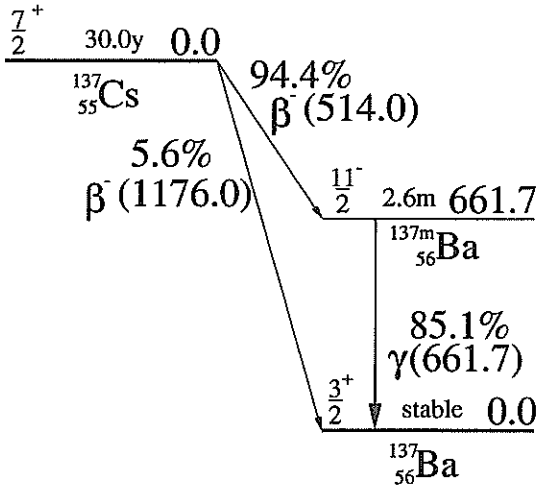

Fig. C.3: Level diagram for ^{137}Cs

C.4 ^{207}Bi

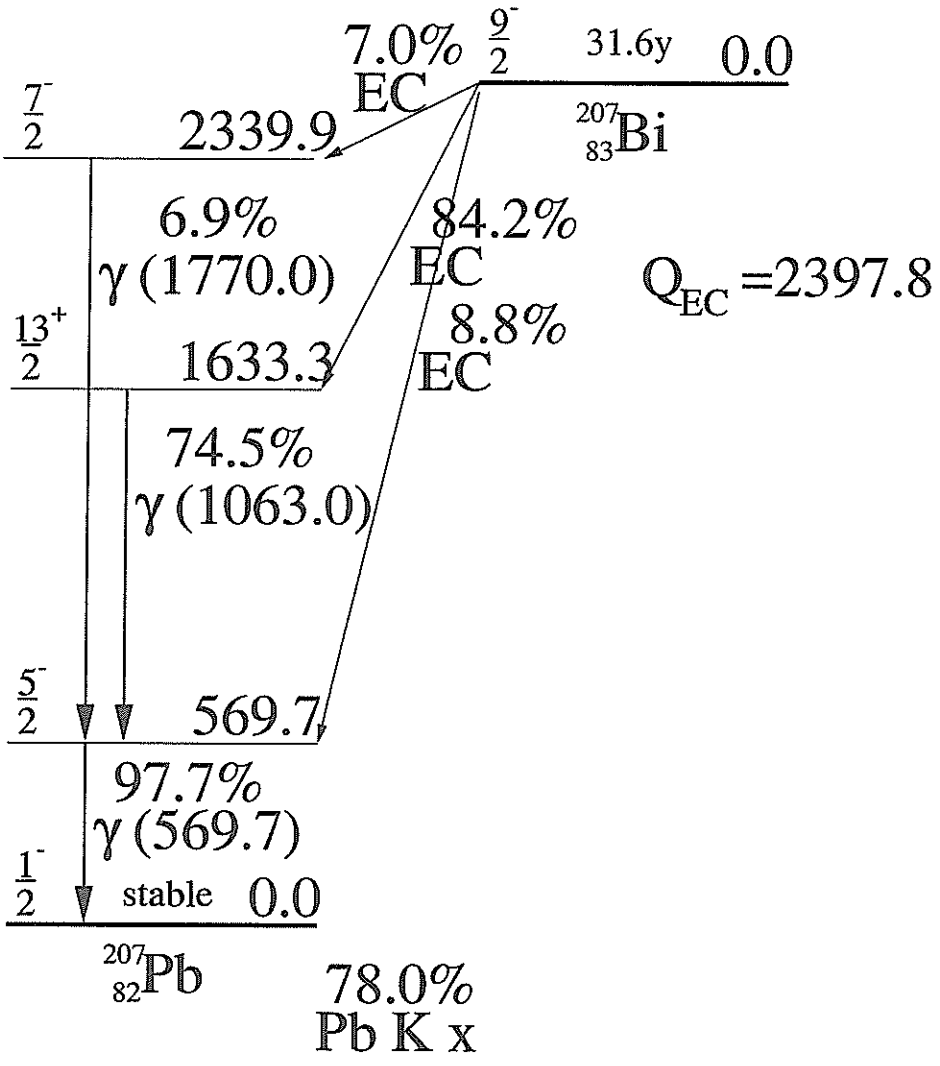

Fig. C.4: Level diagram for ^{207}Bi

C.5 ^{252}Cf

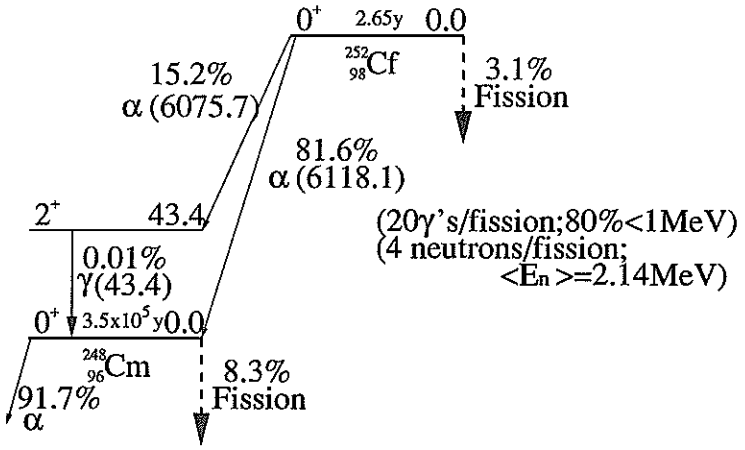

Fig. C.5: Level diagram for ^{252}Cf

C.6 ^{241}Am

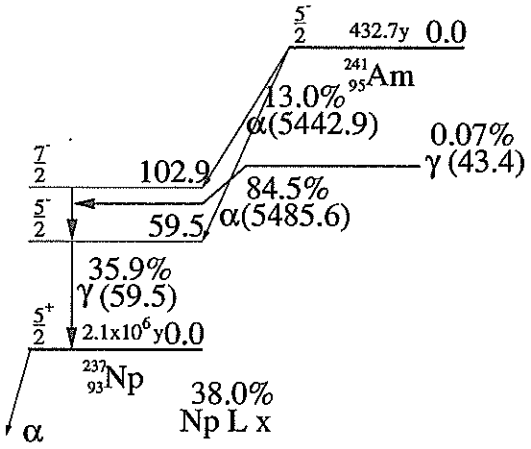

Fig. C.6: Level diagram for ^{241}Am

Bibliography

[1] Super-Kamiokande Collaboration: Y. Fukuda *et al.*, Phys. Lett. **B335**, 33 (1998).

[2] K. Hirata, *et al.*, Phys. Rev. **D44**, 2241 (1991).

[3] B. Achkar *et al.*, "Comparison of anti-neutrino reactor spectrum models with the Bugey 3 measurements", Phys. Lett. **B374**, 243 (1996).

[4] CHOOZ Collaboration: M. Apollonio *et al.*, Phys. Lett. **B420**, 397 (1998).

[5] Palo Verde Collaboration: F. Boehm *et al.*, "The Palo Verde Reactor Neutrino Oscillation Experiment", Nucl. Phys. B. (Proc. Suppl.), 77 (1999) 166.

[6] K. Nishikawa, "Status of K2K (KEK to Kamioka Long Baseline Neutrino Oscillation Experiment)", Nucl. Phys. B. (Proc. Suppl.), 77 (1999) 198.

[7] B.C. Barish, "MINOS - A Status Report", Nucl. Phys. B. (Proc. Suppl.), 70 (1999) 227.

[8] Refer to http://www.neutrino.lanl.gov/BooNE.

[9] LSND Collaboration: C, Athanassopoulos *et al.*, "Evidence for Neutrino Oscillations from Muon Decay at Rest", nulc-ex/9605001, (1996).

[10] T.E. Jannakos, hep-ex/990843, (1999).

[11] P. Vogel, Phys. Rev. **D29**, 1918 (1984).

[12] KamLAND Collaboration: J. Busenitz *et al.*, "Proposal for US Participation in KamLAND" (1999).

[13] Borexino Collaboration: G. Alimonti *et al.*, Astroparticle Physics, 8 (1998) 141.

[14] R.S. Raghavan *et al.*, Phys. Rev. Lett. 80 (1998) 635.

[15] T. Totani *et al.*, in proceedings of the 17th International Conference on Neutrino Physics and Astrophysics, Helsinki (1996); World Scientific.

[16] H.A. Bethe, Rev. Mod. Phys. 62 (1990) 801.

[17] Y. Totsuka, "Particle Physics," Iwanami, Tokyo (1996).

[18] J.N. Bahcall, "Neutrino Astrophysics," Cambridge Univ. Press, (1989).

[19] J.N. Bahcall, P.I. Krastev, and A.Yu. Smirnov, Phys. Rev. **D58**, 096016 (1998).

[20] G.A. Horton-Smith, "Muons, muon spallation, muon tracking, and spallation cut," KamLAND-NOTE-99-16, (1999).

[21] "Soanor," Unpublished Technical Material, Nihon-Gosei Chemical Engineering Co. Ltd.

[22] Particle Date Group: C. Caso *et al.*, Eur. Phys. J. C3 (1998).

[23] H. Kawada, "Techniques for Radiation Experiment," Univ. of Tokyo Press, Tokyo (1986).

[24] F. Yamasaki *et al.*, "Radiation," Kyoritsu, Tokyo (1981).

[25] G. Ranucci *et al.*, "Scintillation decay time and pulse shape discrimination of binary organic liquid scintillators for the Borexino detector," Nucl. Inst. and Meth. in Phys. Res. A 350 (1994) 338.

[26] N. Tsoulfanidis, "Measurement and Detection of Radiation," McGraw-Hill, (1983).

[27] W.R. Leo, "Techniques for Nuclear and Particle Physics Experiments, A How-to Approach, Second Revised Edition," Springer-Verlag, (1994).

[28] H. Ishikawa, "Measurement Method for Liquid Scintillation," Nanzando, Tokyo (1977).

[29] Arthur Beiser, "Concept of Modern Physics, Third Edition," McGraw-Hill Book Co., New York (1981).

[30] R.B. Firestone *et al.*, "Table of Isotopes, Eighth Edition," Johns Wiley & Sons, New York (1996).

Acknowledgements

I would like to show my profound gratitude to many people in Recerch Center for Neutrino Science in my completion of this dissertation. In particular, I would like to thank Prof. A. Suzuki, Assistant Prof. J. Shirai, Assistant Prof. F. Suekane and Assistant Prof. K. Inoue for their valuable advice for this thesis. I also show my thanks to Dr. S. Hatakeyama, Dr. M. Koga, Dr. K. Furuno, Dr. G.A. Horton-Smith, Dr. K. Nakamura, Dr. K. Ishihara and Dr. T. Mitsui for their valuable suggestion for my study in the Test Bench Facility. As well, I am very grateful to all the technical officials, secretaries and students in this center, especially those who complete the Master Program together, S. Azuchi, Y. Ikarashi, T. Itoh, K. Tagashira, Y. Shirasaki and O. Tajima for giving me an enjoyable life until today.

Last but not the least, I would like deeply to express my appreciation to my parents and my best friends for everything.

Sendai, February 2000 *Hideki Watanabe*